The background of the entire page is a satellite or aerial photograph showing a series of parallel, wavy sediment ridges or waves in the Irish Sea. The ridges are light-colored, likely sand or silt, and are spaced out across the darker blue water. The perspective is from an elevated angle, showing the curvature of the ridges.

Formation and evolution of relict trochoidal sediment waves in the Irish Sea throughout their post-glacial history

Master Thesis

Marcus Rademaker

Formation and evolution of relict trochoidal sediment waves in the Irish Sea throughout their post-glacial history

by

Marcus Rademaker

To obtain the degree of

Master of Science
in River and Coastal Engineering

at the University of Twente,
at the Faculty of Engineering Technology, Enschede
to be publicly defended on
February 16, 2023

Student number:	2420465
Project duration:	April, 2022 - February, 2023
Head graduation committee:	Dr.ir. B.W. Borsje (Bas)
Daily supervisor:	Dr.ir. J.H. Damveld (Johan)
Supplementary supervisors:	ir. P.H.P. Overes (Pauline) Dr. K.J.J. van Landeghem (Katrien)
Institution:	University of Twente, Enschede
Faculty:	Faculty of Engineering Technology
Programme:	Water Engineering & Management

Cover Image: Seafloor sand dunes (Ma, 2021)

**UNIVERSITY
OF TWENTE.**

Preface

Nu ik op het punt sta mijn studie civiele techniek af te ronden, kijk ik terug op een prachtige studententijd. De reis naar dit punt is zowel uitdagend als lonend geweest, omdat ik de kans heb gehad om uit te vinden waar mijn interesses liggen op het gebied van civiele techniek. Ik ben blij dat ik gekozen heb voor de mastertrack 'River and Coastal Engineering', want ik heb ontzettend veel geleerd over dit interessante onderwerp.

Deze scriptie is het resultaat van maandenlang hard werken en toewijding. Ik heb dit onderzoek uitgevoerd op een specifiek gebied van de mastertrack met betrekking tot zandgolven, waardoor ik meer inzicht heb gekregen in het modelleren en de uitdagingen die het met zich meebrengt. De bevindingen en aanbevelingen in dit proefschrift vormen aanvullende informatie voor het onderzoeksveld en ik hoop dat ze van grote waarde zullen zijn voor onderzoekers en andere geïnteresseerden.

Gedurende dit traject heb ik de steun en begeleiding gehad van mijn begeleiders Bas, Katrien, Pauline en Johan. Ik heb hun begeleiding als prettig en leerzaam ervaren en wil hen hiervoor erg bedanken. Een speciaal woord van dank gaat uit naar Johan, vooral voor de gesprekken die niet over de scriptie gingen. Ook wil ik mijn dank uitspreken aan vrienden en familie, die mij bij verschillende gelegenheden hebben gesteund en geholpen.

Ik kijk ernaar uit om mijn opgedane kennis in het werkveld te gebruiken.

*Marcus Rademaker
Breda, February 2023*

Summary

Trochoidal sediment waves are large-scale rhythmic bedforms in a non-cohesive, shallow and tide-dominated marine environment and are observed at several locations which experienced glaciations, e.g. the Irish Sea. The abnormal heights of trochoidal sediment waves do not scale with the present-day water depths and current hydrodynamics are unable to form these bedforms. Therefore, the hypothesis states that the coarse cores of trochoidal sediment waves are relicts and their generation is linked to palaeo-tidal conditions during the marine transgression after the Last Glacial Maximum, i.e. 26,000 years before present. Over time, the Irish Sea encountered extreme sea-level rise and significantly changing tidal dynamics before conditions stabilised around 6,000 years ago. Nowadays, a sand veneer on the flanks of the present-day core is mobile during high-energy events. These relicts can comprise a nuisance to offshore projects and affect hydrodynamic processes as macroscale roughness to the bed due to their abnormal heights, thereby impacting the entire ecosystem.

Processes influencing the genesis of trochoidal sediment waves however remain poorly understood. Process-based models can be used to simulate present-day sand wave behaviour. The contemporary model set-up however needs significant adjustments due to the coarse nature, larger water depths and a substantial time-scale. Nevertheless, these models may give insights into the genesis of relict trochoidal sediment waves. The aim of this research is therefore to explain the formation and evolution of trochoidal sediment waves throughout their post-glacial period using an existing process-based sand wave model in Delft3D.

First, reconstructed palaeo-tidal conditions and the present-day morphological characteristics of trochoidal sediment waves in the Irish Sea are analysed. The first indicates a clear trend of intensifying peak bed shear stresses and significant sea-level rise. Bathymetry data from the Amplifies Sediment wave Irish Sea project subsequently showed site-specific characteristics with wave heights and wavelengths ranging between 11 to 35 m and 340 to 560 m, respectively. Furthermore, grab samples obtained along trochoidal sediment waves mainly presented multimodal sediment mixtures with the coarsest sediments found in the troughs.

Subsequently, the model is adjusted according to the Irish Sea. A sensitivity analysis is conducted to find a suitable parameter setting. Through a 2DV case study sediment wave formation and evolution on a millennial time-scale is modelled following the trend obtained from the palaeo-tidal reconstruction. Sea level rise and enhanced hydrodynamics are simulated with depth increments and increasing bed roughness and tidal conditions, respectively. The model results show that sediment waves grow in height over time and that longer wavelengths prevail at larger depths. This resulted in wave heights and wavelengths comparable to those observed in the field.

At last, a thin sand layer is added at the bed to the 2DV case study model through bed stratification to determine the initial morphodynamic response. This layer of sand represents the observed mobile sand veneer. Model simulations show that the sand covers the flanks and troughs of the coarse core over time thereby decreasing its original height and tending towards a new equilibrium. Observations however imply that the coarsest sediments are found in the troughs. Furthermore, the sand layer is shown to be mobile dependent on the tidal current during the simulations.

In comparison to previous sand wave modelling studies, this research can be considered as a starting point of modelling bedforms with a coarser nature which are located at significantly larger water depths. Through a case study model with an idealized set-up the research shows that it is also possible to model over a significant time-scale despite the associated large uncertainties. Moreover, this study indicates that observed trochoidal sediment waves in the Irish Sea formed and evolved between 12,000 and 6,000 years before present thereby strengthening the geological hypothesis.

This model set-up is recommended for modelling on a substantial time-scale to qualitatively support hypotheses. Recommended research includes the application of the case study model for other study areas which experienced or face sea level rise. Collecting more grab sample data and further exploration of including processes within the set-up could potentially help to further understand the formation and evolution of these relict bedforms.

Contents

Preface	i
Summary	ii
Nomenclature	v
1 Introduction	1
1.1 Background	1
1.2 Knowledge gap	3
1.3 Research aim and questions.	3
1.4 Research approach	3
1.5 Report outline.	4
2 Theoretical framework	5
2.1 Tidal sand waves	5
2.2 The Irish Sea	9
2.3 Trochoidal sediment waves	11
3 Delft3D model description	13
3.1 Basics of Delft3D	13
3.2 Numerical model parameters	13
3.3 Hydrodynamics	15
3.4 Sediment transport	17
3.5 Bed evolution	18
4 Data-analysis	20
4.1 Description of data	20
4.2 Observations from the AmSedIS project	21
4.3 Conclusions.	25
5 Sensitivity analysis	26
5.1 Numerical model parameters	26
5.2 Process parameters	27
5.3 Conclusions.	34
6 Post-glacial modelling	36
6.1 Model set-up	36
6.2 Results	39
6.3 Conclusions.	42
7 Present-day modelling	44
7.1 Model set-up	44
7.2 Results	45
7.3 Conclusions.	46
8 Discussion	48
9 Conclusions	52
10 Recommendations	54
References	56
A Irish Sea	63
A.1 Quaternary	64
A.2 Map of the present-day Irish Sea	65

A.3 Amphidromic systems	66
A.4 Sediment distribution	67
A.5 Peak bed shear stresses	68
B AmSedIS data	69
B.1 Area 3-3.	70
B.2 Area 4N	72
B.3 Area 9.	74
B.4 Area 12M	76
B.5 Area 13N	78
B.6 Area 14E	80
B.7 Area 14W	82
C Fastest growing mode	84
C.1 Case I	85
C.2 Case II	88
D Circulation cells	89
D.1 Suspended load transport	90
D.2 Slope effect tuning parameter	91
D.3 Chezy roughness.	92
D.4 Grain size	93
D.5 Tidal velocity amplitude	94
E Sediment transport	95
E.1 Suspended load transport	96
E.2 Slope effect tuning parameter	97
E.3 Chezy roughness.	98
E.4 Grain size	99
E.5 Tidal velocity amplitude	100
F Bed development	101
F.1 Morphological acceleration factor	102
F.2 Suspended load transport	105
F.3 Slope effect tuning parameter	106
F.4 Chezy roughness.	109
F.5 Grain size	112
F.6 Tidal velocity amplitude	115
F.7 Longer initial wavelength	118
G Bed stratification	120
G.1 Morphological acceleration factor	121

Nomenclature

Acronyms

Abbreviation	Definition
AmSedIS	Amplified Sediment wave Irish Sea
BIIS	British-Irish Ice Sheet
BP	Before present
FGM	Fastest growing mode
GIA	Glacial isostatic ddjustment
GRADISTAT	Grain size distribution and statistics package
LAT	Lowest astronomical tide
LGM	Last glacial maximum
LOT	Lambeck's ocean Tide
MBES	Multibeam echosounder
MORFAC	Morphological acceleration factor
M_2	Lunar semi-diurnal
UKCS	United Kingdom Continental Shelf
S_2	Solar semi-diurnal
2DV	Two-dimensional vertical

List of Symbols

Symbol	Definition
a	Reference height
A	Asymmetry of sediment wave
A	Complex bed amplitude
A	Calculated bed amplitude
A_0	Initial sediment wave amplitude
c	Suspended sediment mass concentration
c_{mig}	Migration rate
C	Chezy roughness coefficient
d	Water depth
d_g	Uniform diameter of gravel
d_i	Grain size of i-th percentage
d_{ref}	Reference grain size
d_s	Uniform diameter of sand
D_{50}	Median sediment diameter
F_g	Gravel fraction
F_s	Sand fraction
F_u	Horizontal exchange of momentum due to turbulent fluctuations
g	Gravitational acceleration
$h(cr)$	Water depth at sediment wave crest
H	Wave height
H_0	Reference water depth
H_1	Total water depth
k	Wave number

Symbol	Definition
k_s	Nikuradse roughness length
K_ϕ	Kurtosis in logarithmic phi-scale
L	Sediment wave wavelength (trough spacing)
L_a	Thickness of active transport layer
L_b	Thickness of base layer
L_g	Initial thickness of gravel layer
L_s	Initial thickness of sand layer
L_{tot}	Total available sediment thickness
$L_{u,max}$	Maximum (initial) underlayer thickness
$L_{1,2}$	Wavelength components
M_ϕ	Mean grain size in logarithmic phi-scale
MF	Morphological acceleration factor
M_e	Excess sediment mobility number
M_s	Sediment mobility number
n	σ -layer number
N	Number of underlayers
p	Confidence level
P_u	Hydrostatic pressure gradient
r	Linear correlation coefficient
R_p	Reynolds number
Sk_ϕ	Skewness in logarithmic phi-scale
S_b	Bed load transport
S_s	Suspended load transport
t	Time
T	Tidal period
u	Flow velocity in x-direction
u_{cr}	Critical depth averaged velocity
u_r	Magnitude of equivalent depth averaged velocity
U	Magnitude of the depth-averaged horizontal velocity
U_{s0}	Residual current
U_{s2}	Tidal velocity amplitude
w	Flow velocity in z-direction
w_s	Settling velocity
x, z	Cartesian coordinates
$z_{b,t}$	Bed level at time t
$z_{b,eq}$	Equilibrium bed level
ΔS	Observed sediment wave height
α_{BS}	Slope effect parameter
α_s	Bed slope correction factor
ζ	Water level
ϵ	Dissipation
ϵ_p	Bed porosity
$\epsilon_{s,xz}$	Sediment diffusivity coefficients in x- and z-direction
γ	Growth rate
κ	Turbulent energy
λ	Sediment wave wavelength (crest spacing)
λ_{FGM}	Wavelength of FGM
λ_0	Initial sediment wave wavelength (crest spacing)
ν	Kinematic viscosity of water
ν_T	Vertical eddy viscosity
ϕ	Internal angle of friction
ϕ_i	Logarithmic phi scale
ρ_s	Sediment density
ρ_0	Reference water density

Symbol	Definition
σ	Scaled vertical coordinate
σ_ϕ	Sorting in logarithmic phi-scale
σ_{S_2}	Angular Frequency of S_2 constituent
τ_b	Bed shear stress
$\tau_{b,max}$	Maximum bed shear stress
ω	Flow velocity in σ -direction

1

Introduction

1.1. Background

Tidal sand waves (Figure 1.1b) are large-scale rhythmic bedforms in a noncohesive, shallow and tide-dominated marine environment. Sand wave patterns are generated by the complex interaction between hydrodynamics, sediment transport and morphology (Hulscher, 1996). A distinction in origin can be made between still actively forming and evolving sand waves which can migrate up to tens of metres per year (Van Landeghem et al., 2012) and relict sand waves which are formed due to the marine transgression several thousands of years ago and have only slightly reshaped after their formation (Albarracín et al., 2014). These bedforms can pose a serious threat to multiple offshore human activities and affect hydrodynamic processes as macroscale roughness to the bed impacting ecosystems (Németh et al., 2003; Games & Gordon, 2015; Roetert et al., 2017).

Trochoidal sediment waves are observed in the Irish Sea (Van Landeghem et al., 2009a). The nearly symmetrical, sharp-crested sediment waves with trochoidally-shaped flanks differ significantly from active and smaller-sized sand waves. Their wavelengths are dependent on whether they are located in a regularly spaced sediment wave assemblage or in isolation, i.e. when mobile sediment supply is sufficient or limited, respectively (Van Landeghem et al., 2009a). Trochoidal sediment waves consist mainly of a relatively coarse (sandy gravel) and poorly sorted core (Valentine et al., 2002; Van Landeghem et al., 2013). Due to their coarser nature, the term “sediment wave” is therefore adopted rather than sand wave. During high-energy events, the flanks of present-day trochoidal sediment waves are often reshaped by a mobile sand veneer (Albarracín et al., 2014; Neto et al., 2018) that can even include migrating superimposed sand waves (Van Landeghem et al., 2009a).

The coarse cores of trochoidal sediment waves are considered relicts. The abnormal heights of trochoidal sediment waves do not scale with the present-day water depth of the Irish Sea (Van Landeghem et al., 2013). In the Irish Sea, observed heights of these trochoidal sediment waves amplify from 5 m up to 36 m, which can comprise more than one third of the water column. Their generation is linked to significantly changing palaeo-conditions during the marine transgression after the Last Glacial

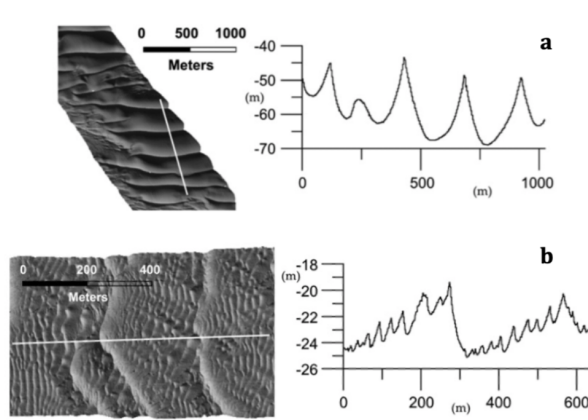


Figure 1.1: Shaded relief images of multibeam swath bathymetry data showing (a) trochoidal sediment waves and (b) sand waves in assemblage in the Irish Sea (Van Landeghem et al., 2009b).

Maximum (LGM), 26 kiloannum before present (BP), at multiple locations over the world, e.g. Canada (Barrie et al., 2009), France (Franzetti et al., 2013), Spain (Albarracín et al., 2014), and the eastern U.S. (Valentine et al., 2002).

During the post-glacial period temperatures evolved gradually and resulted in the retreat of the British-Irish Ice Sheet allowing water to enter the Irish Sea (Figure 1.2). Over time, the Irish Sea encountered extreme sea-level rise and significantly changing tidal dynamics due to the varying basin geometry. After the period of 10 ka BP, the bed load transport directions in the central Irish Sea changed due to the retreating ice sheets to a symmetrical tidal regime (Uehara et al., 2006). Since then, the central Irish Sea is associated with bed load parting zones. The nearly symmetrical tide and the long-term reversals of the slightly dominant current-induced bed stresses in these zones are suspected to have contributed significantly to the bi-directionally piling up of coarse sediment (Valentine et al., 2002; Van Landeghem et al., 2009a). Additionally, the formation of trochoidally-shaped sediment waves is supported by significant bed stresses between 7 and 10 ka BP due to the enhanced ocean tides and local configurations (Uehara et al., 2006).

A continuous mobile sediment supply turns out to be crucial for the further growth of trochoidal sediment waves (Van Landeghem et al., 2013). This supply is most probably from sediments infilling glacial incisions which overlap with trochoidal sediment wave fields (Jackson et al., 1995). This process is triggered due to converging sediment transport paths and due to scouring around nearby sediment waves which consist of coarse particles (Van Landeghem et al., 2009a) and is potentially strengthened by the formation of standing internal waves due to stratification (Cartwright, 1959). Another process that is linked to the trochoidal sediment waves is the hiding-exposure effect due to multimodal sediment mixture (Van Landeghem et al., 2013).

After 5 ka BP, it is assumed that the trochoidal sediment waves in the Irish Sea became moribund since hydrodynamics stabilised (Uehara et al., 2006). The geological hypothesis states that present-day hydrodynamics are unable to generate these enigmatic features (Van Landeghem et al., 2009a; Albarracín et al., 2014). Processes influencing their generation and evolution however remain poorly understood due to limited studies and the large timescale.

Process-based models are commonly used to simulate present-day sand wave behaviour, mainly focusing on the North Sea. These models are used in sand wave modelling studies to investigate several processes which theoretically can influence sand wave characteristics, e.g., sediment mixture (Damveld et al., 2020b) and tidal forcing (Besio et al., 2004; Németh et al., 2002). A non-linear approach to simulate sand wave morphodynamics is the use of the complex numerical shallow water model Delft3D (Deltares, 2022) in which various physical processes can be incorporated in an advanced manner. Such a model can be operated to investigate sand waves in multi-layer mode, i.e. two-dimensional vertical (2DV) or three-dimensional (3D), in which hydrodynamics, sediment transport and bed evolution are coupled and updated consecutively after each time step (Lesser et al., 2004). Here, 3D model application is generally limited due to large computation time. The Delft3D-4 model is most frequently used in sand wave modelling studies.

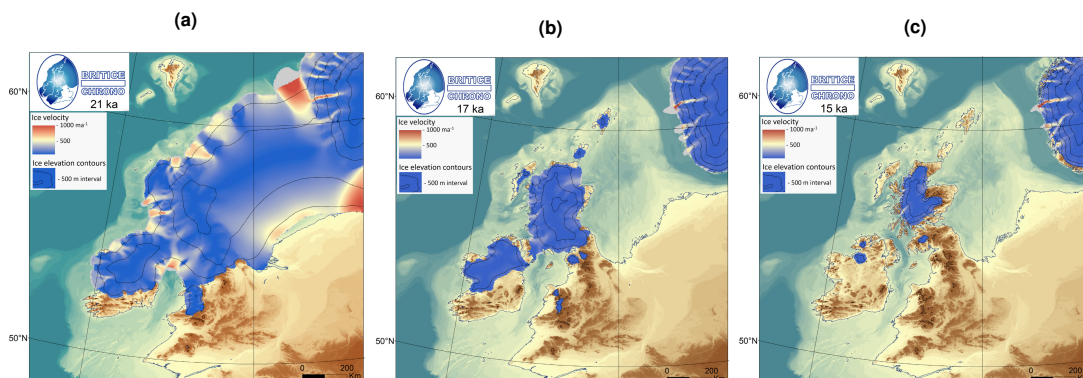


Figure 1.2: The BRITICE-CHRONO model reconstruction combining the physics of ice-sheet modelling with the geomorphological, geological and chronological data on ice limits and glacio-isostatic mass loading for (a) 21, (b) 17 and (c) 15 ka BP (Clark et al., 2022).

1.2. Knowledge gap

Very large relict trochoidal sediment waves can be found in the Irish Sea which significantly differ from the active, asymmetrical, and smaller-sized sand waves. A hypothesis states that the coarse core of these types is initially formed in a distant past. Its evolution over time is linked to numerous factors such as the bidirectionality of the tidal currents, glacial incisions, and scour mechanisms. However, processes influencing the formation and evolution of these types remain poorly understood due to limited studies and large uncertainty associated with the timescale of millennia.

Process-based models can be applied to better understand processes influencing the formation and evolution of trochoidal sediment waves in the Irish Sea throughout their post-glacial period. The applied model set-up is however based on present-day sand waves, mainly focusing on the North Sea. The Irish Sea has not yet been investigated with these types of models and its historical and current environment differs significantly from the southern North Sea such that the model by Damveld et al. (2020b) cannot instantly be used to reproduce sediment waves. Also, preliminary sand wave modelling studies only included a sand mixture, whereas the core of trochoidal sediment waves consists of relatively coarse sediments. Until now, gravel is not included in sediment mixtures during model simulations, let alone pure gravel. Likewise, the sorting process of a mobile sand veneer hosting the coarse core of equilibrium stage sediment waves is not investigated using these types of models.

1.3. Research aim and questions

According to the knowledge gaps found in the literature study, the aim of this study is defined, i.e.

to explain the formation and evolution of trochoidal sediment waves throughout their post-glacial history using an existing process-based sand wave model.

To achieve this aim, three sub-questions are specified and stated below. These sub-questions serve to structure the forthcoming research. A short motivation for each sub-question is included.

I. What are the palaeo-tidal conditions and present-day morphological characteristics of trochoidal sediment waves in the Irish Sea?

Information with respect to the palaeo- and present-day environment along observed trochoidal sediment waves in the Irish Sea will be used as a starting point for the parameter setting of the Delft3D model. In addition, the data will be compared to the model results.

II. In what way can an existing process-based sand wave model be adjusted to reconstruct the formation and evolution of the coarse core of trochoidal sediment waves during the post-glacial period?

The aim of the post-glacial modelling phase will be to validate the hypothesis which states that the coarse core of trochoidal sediment waves is initially formed in a distant past and evolved over time along with the sea-level rise until hydrodynamics stabilised. Thereby, processes influencing its formation and evolution will hopefully be better understood.

III. What is the initial morphodynamic response of equilibrium stage sediment waves due to the addition of a thin sand layer at the bed?

The inclusion of a sand layer within the Delft3D model will represent the mobile sand veneer that is observed hosting the coarse core of present-day trochoidal sediment waves. Short-term model simulations will give insight into initial morphodynamic behaviour and sorting patterns along sediment waves.

1.4. Research approach

The research aim and questions formulated above form the structure of the research to be carried out. The first question will be answered through the output of a Glacial Isostatic Adjustment (GIA) model by Uehara et al. (2006) and data-analysis of the Amplified Sediment wave Irish Sea (AmSedIS) project.

The palaeo-peak bed shear stresses and water depth of the last 16 ka near the survey areas will be reconstructed by the GIA model. During the AmSedIS project high resolution swath bathymetry and grab sampling data at survey areas of trochoidal sediment waves were obtained. This data set will be used to specify the present-day trochoidal sediment wave characteristics and to analyse correlations and trends. This information will be used as a starting point for the model set-up for the next research question.

Subsequently, a 2DV set-up which generates gravel waves will be established for a palaeo-depth, a symmetrical tide, and a uniform gravel composition using an existing sand wave model by Damveld (2020) in Delft3D-4. This model is used to answer the second and third research question. A sensitivity analysis of the numerical model and process parameters on the gravel wave development during the small- and finite-amplitude stage will be carried out which will shed light upon the possibilities of tuning the model. After this, a 2DV case study is set up to reconstruct the palaeo-tidal conditions and time scale. This will be achieved by depth increments thereby taking a leap in time between each case. While starting from a flat bed, the equilibrium bed levels will be adopted as initial topography for the succeeding case to simulate the formation and evolution of the coarse core of trochoidal sediment waves throughout its post-glacial history towards equilibrium, i.e. up to the period hydrodynamics stabilised.

To answer the final sub-question the 2DV case study model will be extended with bed level stratification, i.e. a sand layer will be added to the system on top of sediment waves. This layer will represent the mobile sand veneer that is observed hosting the core of present-day trochoidal sediment waves in the Irish Sea. The equilibrium stage sediment waves that follow from the second research question will be used as initial condition. First, a limited sensitivity analysis will be conducted for the morphological acceleration factor and the uniform diameter of the sand layer to tune the model setting. Thereafter, the short-term response to the bed level and sorting patterns along the sediment waves will be analysed.

1.5. Report outline

The theoretical framework of this study can be found in Chapter 2. Subsequently, the Delft3D model is described in Chapter 3. These two chapters are primarily intended for those with little prior knowledge about sand waves and the Delft3D model. The data of the post-glacial and present-day environment at the survey areas is analysed in Chapter 4. The sensitivity analysis is discussed in Chapter 5 prior to the post-glacial cases (Chapter 6). Chapter 7 describes the initial morphodynamic response of adding a sand layer to the system. Chapter 8 chapter contains a discussion of the limitations of the results, whereas Chapter 9 presents the conclusions of this study including answers to the stated research questions. Finally, recommendations for further research based on the results of this study are discussed in Chapter 10.

2

Theoretical framework

This chapter represents the theoretical framework of this study. First, scientific knowledge about tidal sand waves is summarised. Subsequently, the Irish Sea environment and its history is described. At last, trochoidal sediment waves which are observed in the Irish Sea are discussed.

2.1. Tidal sand waves

This section concerns sand waves which are observed all over the world. First, the definition and the practical relevance of sand waves for this modelling study are introduced. Subsequently, several observational studies over the world are shown and basic sand wave characteristics are briefly described. Hereafter, the formation of sand waves is explained. The section ends with processes that influence sand wave morphodynamics as found in literature.

2.1.1. Definition and practical relevance

Tidal sand waves (hereafter referred to as 'sand waves') are considered as large-scale rhythmic bedforms in a non-cohesive, shallow and tide-dominated marine environment. Its environment distinguishes marine sand waves from their river (Bradley & Venditti, 2017) and estuarine counterparts (Van der Sande et al., 2021). Sand wave patterns on the seafloor are induced by the complex interaction between hydrodynamics, sediment transport and morphology (Hulscher, 1996).

According to Albarracín et al. (2014), sand waves are distinguished between still actively forming, evolving and migrating bedforms and relict bedforms which are formed due to the marine transgression several thousands of years ago and have only slightly reshaped after their formation. The first can due to its morphodynamic behaviour pose a serious threat to multiple offshore human infrastructure, e.g., cables (Roetert et al., 2017), navigation (Katoh et al., 1999), pipelines (Németh et al., 2003) and foundations of offshore oil and gas installations and (planned) wind farms (Velenturf et al., 2021). Moreover, processes influencing these present-day evolving sand waves can provide understanding in the palaeo-conditions for the genesis of relict bed forms. In addition, relict bedforms constitute a nuisance to offshore projects and affect hydrodynamic processes as macroscale roughness to the bed, thereby impacting the entire ecosystem.

2.1.2. Occurrence

Sand waves are observed in shallow coastal sea in which bed shear stresses induced by the dominant symmetrical tidal flow are substantial enough to exceed the corresponding critical threshold value and thereby initiate sediment transport (Hulscher & Dohmen-Janssen, 2005). Figure 2.1 shows multiple locations worldwide where, among others, sand waves are observed, i.e. the continental shelves of Argentina (Aliotta & Perillo, 1987), Australia (Harris, 1989), Brazil (Figueiredo, 1980), Canada (Barrie et al., 2009), China (Wang et al., 2012), India (Wagle & Veerayya, 1996), Japan (Katoh et al., 1999), Korea (Park et al., 2003), Mozambique (Flemming & Kudrass, 2018), South Africa (Flemming, 1978), Taiwan (Zhou et al., 2018), the eastern and western U.S. (Field et al., 1981; Barnard et al., 2006; Bokuniewicz et al., 1977), the European margin, in the Irish Sea (Van Landeghem et al., 2009b) and North Sea (Damen et al., 2018), Denmark (Anthony & Leth, 2002), France (Franzetti et al., 2013), Germany (Antia, 1995), Greece (Lykousis, 2001), Italy (Santoro et al., 2004), Spain (Albarracín et al.,

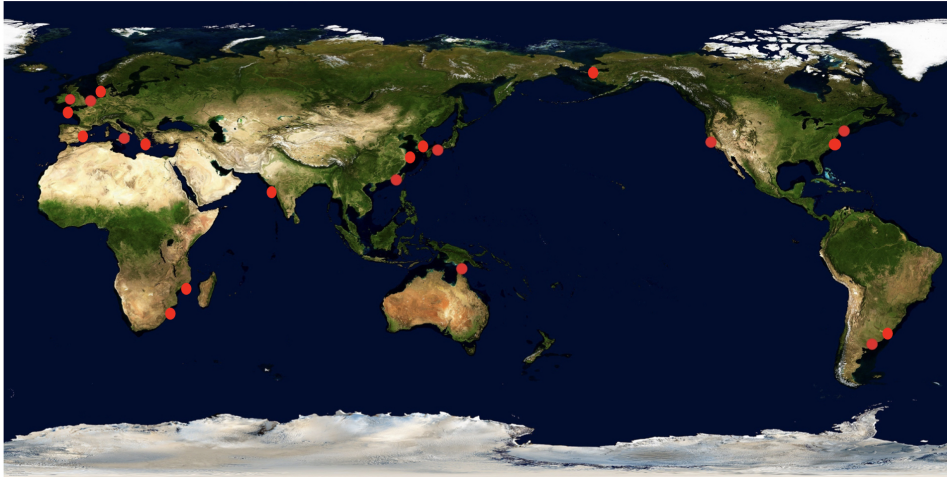


Figure 2.1: Observed sand waves at locations over the world (not complete) indicated with red dots. References for each location can be found in the main text. Image originally after worldmapsonline.com.

2014). This shows that sand waves are observed all over the world and that their practical relevance is not limited to a single location.

Sand waves differ from other marine bed forms in their properties shown in Table 2.1. Sand waves mainly have wavelengths of hundreds of metres and significant wave heights in the order of several metres to tens of metres (Van Landeghem et al., 2009b; Damen et al., 2018). Meanwhile, active sand waves are mobile and persistent and can migrate tens of metres per year (Roetert et al., 2017; Van Landeghem et al., 2012), while relict sand waves are moribund (Albarracín et al., 2014). The formation of sand waves takes several years to decades. The morphological time scale is thereby significantly larger than the timescale of the tidal motion (Damveld, 2020).

2.1.3. Characteristics

Sand wave fields are mostly referred to as 2D features perpendicularly orientated to the dominant symmetrical tide since the sand wave crests are much longer than their wavelengths (Hulscher & Dohmen-Janssen, 2005). However, their longitudinal length can vary strongly (Damveld, 2020). A planform geometry classification of bedforms is made by Perillo et al. (2014), see Figure 12. A sand wave field can form a two-dimensional (2D), two-and-a-half dimensional (2.5D) and three-dimensional (3D) pattern by observing the wave crests. In a 2D sand wave field the crest lines are continuous and straight, whereas curved and disconnected crest lines dominate in a 3D field. A 2.5D field represents either disconnected and straight (top) or continuous and curved (bottom) sediment wave crests.

According to Zhang et al. (2019), the wavelength of sand waves (L) is measured from trough to

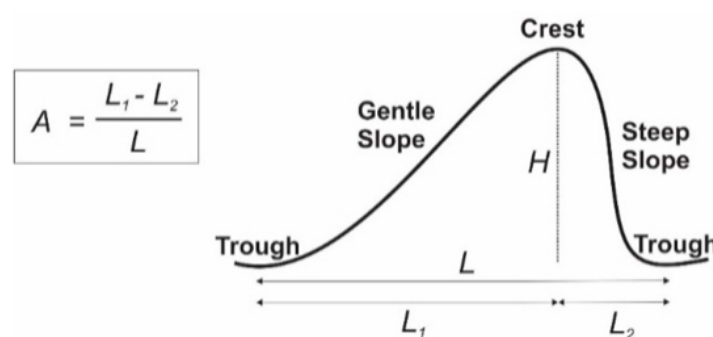


Figure 2.2: Schematic representation of an asymmetrical sand wave with the level of asymmetry A , sand wave height H , wavelength L , stoss-side length L_1 and lee-side length L_2 (Cheng et al., 2020).

Table 2.1: Marine bed form characteristics in order of magnitude: wavelengths, wave heights, migration speed, orientation with respect to the dominant tide and associated morphological time scale (Damveld, 2020).

Bed form type	Wavelength L [m]	Wave height H [m]	Migration [myr^{-1}]	Orientation [$^{\circ}$]	Morphological time scale
Ripples	$10^1 - 10^0$	$10^{-2} - 10^{-1}$	$10^2 - 10^3$	~ 90	<i>Minutes - hours</i>
Megaripples	$10^1 - 10^0$	$10^{-1} - 10^{-2}$	$10^2 - 10^3$	~ 90	<i>Hours - days</i>
Sand waves	$10^2 - 10^3$	$10^0 - 10^1$	$10^0 - 10^1$	~ 90	<i>Years - decades</i>
Long bed waves	$\sim 1,500$	~ 5	<i>Unknown</i>	–	<i>Centuries</i>
Shoreface- connected ridges	$\sim 10^3$	$10^0 - 10^1$	$\sim 10^0$	–	<i>Centuries</i>
Sand banks	$10^3 - 10^4$	$10^0 - 10^1$	–	$\sim 0 - 30$	<i>Centuries</i>

trough, while the wave height (H) represents the vertical distance between the crest and the adjacent trough. The migration rate of sand waves is determined by the horizontal displacement of the crest over a time interval. However, bathymetric data of two sufficiently far apart time periods is needed to determine migration rates. The water depth ($h(cr)$) is indicated as the distance from the crest of the sediment wave to the surface water of the sea (Van Landeghem et al., 2012).

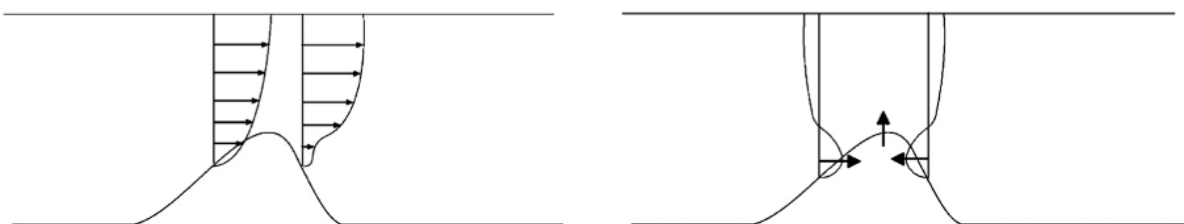
2.1.4. Formation

Hulscher (1996) approached the generation of tidal sand waves as small sinusoidal perturbations superimposed on a flat seabed that are submitted to the tide which results in flow alterations. Given continuity, the flow on the lee and stoss side decelerates and accelerates due to an increasing and decreasing water depth, respectively. This occurs in both ways since the tide is characterised by an oscillatory flow (Figure 14). The tide-averaged flow then induces vertical residual circulation cells and bedload sediment transport towards the sand wave crest (Figure 15). The upslope sediment transport is counteracted by gravitational forces, i.e. downslope bedload transport towards the troughs or slope-induced transport. Slope-induced transport is strongly dependent on the steepness of the sand wave slope.

In addition to bedload and slope-induced transport, Borsje et al. (2014b) identified a third dominant mechanism in relation to sand wave formation, that is, suspended sediment transport. Suspended sediment transport also dampens sand wave growth, like slope-induced transport, and depends on grain size and current strength. This damping effect is explained by the phase lag between sediment in suspension and sand waves (Borsje et al., 2014b). At locations where suspended load transport is dominant, sand waves might not form at all (Damen et al., 2018).

2.1.5. Processes influencing morphodynamics

Multiple processes can affect the morphodynamics of sand waves as is shown by various modelling studies, e.g., biota (Damveld et al., 2020a), dredging (Campmans et al., 2021), sediment availability (Damveld et al., 2021) and mixture (Damveld et al., 2020b), storms effects (Campmans et al., 2019),

**Figure 2.3:** Velocity profile (left) and time-averaged (residual) velocity profile (right) over a sand wave (Tonnon et al., 2007).

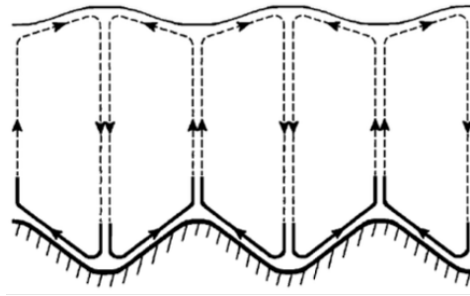


Figure 2.4: Residual vertical circulation cells over sand waves (Hulscher, 1996).

tidal forcing (Besio et al., 2004; Németh et al., 2002) and underlying seabed topography (Leenders et al., 2021). Below, the influence of the tidal current and sediment mixture are discussed as these processes align with this study.

Tidal current

The tide is known as the principal forcing mechanism to generate sand waves (Hulscher, 1996). Wang et al. (2019) concluded that the growth rate of sand waves depends on the magnitude of the tidal current, i.e. increasing tidal currents are associated with higher growth rates. However, sand wave formation is also limited by the tidal current strength since its formation is strongly dependent on the dominant sediment transport mode (Borsje et al., 2014a). Sand wave wavelengths and heights decrease with an increasing tidal current (Sterlini, 2009; Van Santen et al., 2007).

Only considering a symmetrical tide (e.g. M2) results in sand wave growth with no migration. When a residual current, e.g., due to wind stress or a pressure gradient is present, the vertical circulation cells (Figure 2.4) are distorted in the basic state which induces the migration in the flow direction of the residual current (Németh et al., 2002). The modelling study of Van Gerwen et al. (2018) concluded that an increasing residual current lowers the finite-amplitude of sand waves. This also applies to tidal asymmetry, e.g. due to the superposition of the M2 and M4 tidal constituents. The combination with its first harmonic results in an asymmetrical tidal wave and a phase lag. Consequently, substantial dissimilarities between the peak bottom stress during ebb and flood tide, as well as a mean bottom stress, emerge which are important in relation to sediment transport and thereby the morphodynamics of sand waves. The migration direction then depends on the phase shift between those constituents and can for a specific range of phase shifts even prevail a residual current (Besio et al., 2004). Moreover, combining suspended load transport and tidal asymmetry reduces equilibrium sand wave heights even more (Van Gerwen et al., 2018). Additionally, the spring-neap tidal cycle can influence sand wave formation substantially depending on the contribution of suspended load to the total load (Blondeaux & Vittori, 2010).

Sediment mixture

The formation and growth of sand waves is not only dependent on the magnitude of the tidal current, but also on the sediment mixture, i.e. in general larger, heavier grains are less easily entrained compared to smaller, lighter grains. The different sediment transport modes have adverse effects on sand wave growth. Therefore, differences in grain sizes can considerably affect sand wave morphology.

The uncertainty of sediment transport becomes larger when the seabed degree of sorting decreases (mixed sediments) and the calculations become more complicated since the different grain sizes interact uniquely with the flow which results in selective resuspension, i.e., the hiding-exposure effect. The hiding-exposure effect represents the process in which larger and more exposed grains hide the smaller particles from the flow (McCarron et al., 2019). This effect influences the properties of sand waves and is included in different sediment transport models (e.g. Roos et al., 2007; Van Oyen et al., 2013). McCarron et al. (2019) concluded that the hiding-exposure effect is dependent on the ratio between the coarsest and finest sediment and results in a significantly larger and smaller critical bed shear stress regarding the mobility of fine and coarse material, respectively. During the formation and evolution of sand waves, the mixed sediments are gradually sorted. Therefore, it is expected that the hiding-exposure effect is time-dependent (Van Oyen & Blondeaux, 2009a).

Several modelling studies investigated sorting patterns along sand waves. Roos et al. (2007) investigated the nonlinear effects of a bimodal sediment mixture. They concluded that sand wave troughs remain relatively well mixed, while coarser grains concentrate at the crest. Van Oyen & Blondeaux (2009a) also investigated grain sorting along sand waves by means of a bimodal sediment mixture and concluded that the hiding-exposure effect leads to finer crests for weaker tidal currents, while strong currents induce coarser crests. In these cases, the sorted sediments in the crest functions as a stabilizing and destabilizing factor, respectively (Van Oyen & Blondeaux, 2009b). In addition, it was found that sediment sorting is opposed by a heterogeneous sediment mixture since grain sizes each have varying transport lengths which can equal to multiple sand wave lengths. Van Oyen & Blondeaux (2009b) explained that the growth rate of sand waves increases for finer sediment mixtures and linked this to suspended load transport which is not in line with the findings of Borsje et al. (2014b).

Damveld et al. (2020b) examined sediment sorting processes of sand wave morphodynamics towards equilibrium by including multiple sediment fractions and excluding hiding-exposure. Increasing the sortedness of the sediment mixture resulted in longer and lower sand waves. The sorting pattern showed that the troughs consisted of finer grains compared to the crests which coincides with field observations. Furthermore, tidal asymmetry caused a concentration of coarser and finer sediments on the respective upper and lower lee slope. The results showed an unerodable layer towards finite-amplitude sand waves due to the immobility of coarse sediments.

2.2. The Irish Sea

The present-day Irish Sea is known as a water body located between the islands of Great Britain and Ireland in the Northeast Atlantic region. The Irish Sea geology and tidal dynamics however are in its history strongly affected by glacial and post-glacial processes, which in turn likely impacted the formation and evolution of bedforms. Therefore, its history is generally elaborated in the following subsection. The current Irish Sea environment is discussed hereafter.

2.2.1. Quaternary glacial history

The Quaternary, that is, the recent geological period of circa 2.6 million years, is characterised by a strongly fluctuating temperature with cold glacial and warm interglacial periods due to the Earth's varying orbit. These periods are represented with growing and decaying ice sheets, respectively. Most of the Irish Sea was constantly glaciated during the cold periods in which the British-Irish Ice Sheet (BIIS) overconsolidated seabed sediments. Three major phases of glacial incisions into older sediments due to the advancing icesheet are documented in the Irish Sea and are linked to the largest glaciations in the Mid to Late Quaternary, i.e. Elsterian, Saalian and Weichselian. The latter is assumed to have the most sustained effect on the present-day environment. These incisions are associated to the bathymetric deeps of the Irish Sea. The glacial incisions eroded and filled these deep channels with seabed sediments, sequentially, diamictons, sands and muds (Jackson et al., 1995).

After the Last Glacial Maximum (LGM), i.e. circa 26 kiloannum (ka or 10^3) years before present (BP), temperatures evolved gradually and resulted in the retreat of the last BIIS allowing water to enter the Irish Sea, see Figure 1.2. Uehara et al. (2006) reconstructed palaeo-tidal dynamics of the dominant M2-constituent using Lambeck (1995) and Peltier (1994) palaeo-bathymetries for every 1,000 years from 16 ka BP to the present day (Figure 2.5). The study of Clark et al. (2022) later recreated scenarios for the pattern and timing of the retreat of the last BIIS for the period between 15 and 31 ka BP.

The change in ocean tidal currents appears to relate strongly to sea-level rise, the emergence of shallow seas and the retreat of the ice sheets over the world, thereby altering the geometry of the ocean basin. The opening of the Hudson Strait which connects the Atlantic Ocean and Labrador Sea to Hudson Bay in Canada is linked to a significant decrease of the M2 tidal amplitude in the Irish Sea between 8 and 10 ka BP. Before this significant change in tidal dynamics, palaeo-bed stresses peaked in the Irish Sea (Uehara et al., 2006). A significant increase in magnitude of peak bed stresses due to enhanced ocean tidal dynamics occurred between 10 and 15 ka BP in the southern and northern Irish Sea, i.e. approximately south of 52.25°N and north of 53.25°N latitude. The shallower regions in between were influenced less due to low sea-levels. However, local configuration changes also increased peak bed shear stresses in these areas between 7 and 10 ka BP, see Figure 2.5.

As sea-levels rose in the southern Irish Sea after the opening of the North Channel between 12-14

ka BP, the bedload convergence and divergence zones relocated northward and more centrally (Uehara et al., 2006). After 9 ka BP, the tides were symmetric in most of the Irish Sea and the vector directions of the modelled bed stresses were comparable to the present-day state, i.e. directing southwards in the southern Irish Sea and northward in the central and northern Irish Sea. After 5 ka BP, the ocean tides and hydrodynamics in the Irish Sea stabilised (Van Landeghem et al., 2009a).

2.2.2. Present-day environment

A map of the present-day Irish Sea is shown in Appendix A.2. The Irish Sea can be considered as a finite channel due to its two entrances, indirectly connected to the Atlantic Ocean at the northern, via the North Channel and Malin Shelf Sea, and southern side, via the Celtic Sea and St. George's Channel. The width of the Irish Sea ranges between 75 and 200 km, while the North Channel is considerably narrower, i.e. approximately 30 km. The width of the southern entrance is larger and in the order of 100 km. Furthermore, its bathymetry can be divided into (1) relatively shallow smooth platforms ($d < 50$ m) located southwest of the Isle of Man and in the eastern Irish Sea, and (2) a rather deep, rough, north to south oriented channel ($d < 150$ m) that connects the two entrances (Howarth, 2005).

At the shallow smooth platforms, relatively low tidal currents (< 0.4 $m s^{-1}$) can be observed due to the juncture of the two incoming tidal waves from the northern and southern entrance (Robinson, 1979). Consequently a standing wave develops, whereas a progressive wave forms in southern Irish Sea (Ward et al., 2018). Relatively large depth-averaged tidal currents (exceeding 1 $m s^{-1}$ during spring-tide) develop near the amphidromic points in the western St. George's Channel and the North Channel, to the north-west of Anglesey and north of the Isle of Man. Especially offshore Anglesey, these tidal currents can reach values above 2 $m s^{-1}$ (Howarth, 1984, 2005; Robinson, 1979).

The sediment distribution in the Irish Sea (Appendix A.4) is a complicated patchwork of various erodible sediment types which are heavily affected by historic events, e.g., glacial and post-glacial processes (Dobson et al., 1971; Tappin et al., 1994; Jackson et al., 1995). The seabed sediment distribution of the Irish Sea can be categorised into the Western and Eastern Irish Sea Mudbelt, the Central Irish Sea gravel belt, areas of mixed sediments and areas of rock and thin sediments. The mobile sediment layer in the Irish Sea ranges from several metres up to 40 m (Mellet et al., 2015).

The semi-diurnal tides, M_2 and S_2 , are the dominant constituents of the Irish Sea which have a velocity amplitude ratio of approximately 3:1, see Appendix A.3 (Pugh, 1981). Higher frequency tides are only significant in shallow water and abruptly changing topography. The semi-diurnal current ellipses located in St. George's Channel are basically rectilinear, almost symmetrical, and north to south oriented, while at locations of weaker tidal currents the ellipse is more rotating resulting in an absence of slack water (Horrillo-Caraballo et al., 2021). There is little vertical variability of the tidal current in the water column. However, the largest changes are found near the bottom compared to mid-depth values, that is, changes in the direction, lag and magnitude of the current and shape of the ellipse (Dobson et al., 1971; Howarth, 1984). In the St. George's Channel, bed load convergence and divergence zones are observed (Figure 4.3). Exact knowledge about sediment transport in these zones is still rather

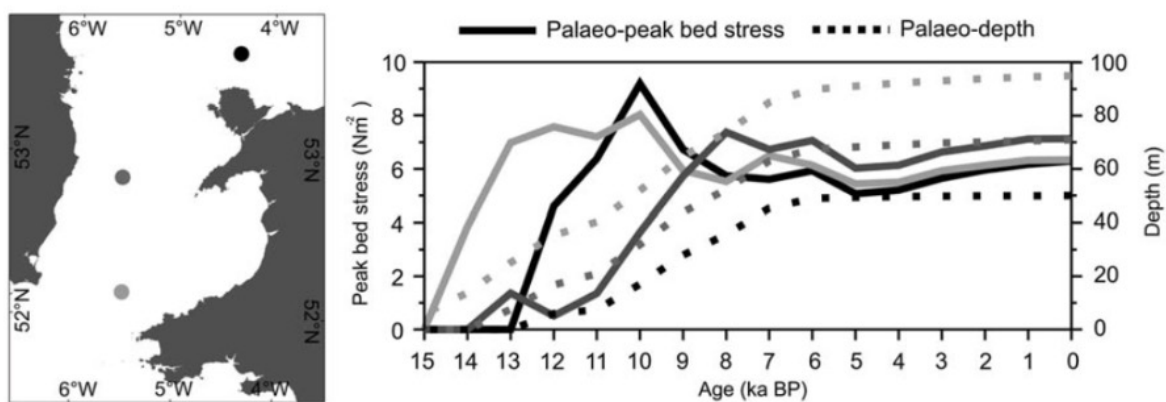


Figure 2.5: Variations in palaeo-peak bed stress and -depth for three locations in the Irish Sea over the last 15,000 years using Lambeck (1995) glacial isostatic adjustment (GIA) model with an ocean-tide open boundary (Van Landeghem et al., 2009a).

incomplete due to a shortage of long-term and short-term data of bed evolution and near bed water motion (Van Landeghem et al., 2012; Creane et al., 2021).

2.3. Trochoidal sediment waves

Trochoidal sediment waves are observed in the Irish Sea with very large heights. Due to its coarser nature, the term “sediment wave” is adopted rather than sand wave. These bedforms are considered relicts and their formation and evolution are linked to palaeo-conditions. However, the processes influencing the formation and evolution of these types remain poorly understood due to relatively few studies and the large uncertainty associated with the timescale of millennia.

2.3.1. Occurrence

Abnormally high trochoidal sediment waves have been observed at multiple locations over the world, e.g. the continental shelves of Canada (Barrie et al., 2009), France (Franzetti et al., 2013), Spain (Albarracín et al., 2014), the eastern U.S. (Valentine et al., 2002) and in the Irish Sea (Van Landeghem et al., 2013). At these locations, the formation and evolution of these relict bedforms are linked to palaeo-conditions during the marine transgression after the Last Glacial Maximum since present-day hydrodynamics are considered insufficient to its construction.

In the Irish Sea, these types of sediment waves are mainly located in bathymetric deeps. In addition, the very large trochoidal sediment waves have been observed adjacent to asymmetrical, normal-sized sediment waves and the trochoidal sediment waves consistently ending up in characteristic deep scour hollows (Van Landeghem et al., 2009a).

2.3.2. Characteristics

Trochoidal sediment waves in the Irish Sea differ significantly from the most known active sand waves. Therefore, their known differing characteristics are described below. A more detailed description of the processes influencing the evolution of these trochoidal sediment waves can be found in the following subsection.

- Their shape is nearly symmetrical to symmetrical and sharp crested with trochoidally shaped flanks;
- Their very large heights do not scale with water depth. They average 15 m and amplify from 5 m up to 36 m, which can comprise more than one third of the water column (Van Landeghem et al., 2013);
- The wavelength of trochoidal sediment waves is dependent on whether they are located in a regularly spaced sediment wave assemblage or in isolation, i.e. when mobile sediment supply is sufficient or limited, respectively.
- They are observed adjacent to actively migrating, asymmetrical, smaller-sized sediment waves and end up in distinctive deep scour hollows;
- They are considered relicts and have most likely been generated between 7 and 10 years ka BP. Their formation and evolution are linked to the bi-directional tidal currents, locally increase of mobile sediment supply due to glacial incisions and scour mechanisms (Van Landeghem et al., 2009a);
- They consist mainly of a coarser, more poorly sorted sediment core which cannot be mobilised by present-day hydrodynamics and of a thin sand veneer covering and migrating over this core during high-energy events (Van Landeghem et al., 2009a; Albarracín et al., 2014; Neto et al., 2018).

2.3.3. Key processes influencing morphodynamics

Besides natural processes influencing sand wave morphodynamics which are described in Section 2.1.5, several other key processes most likely affected the formation and evolution of relict trochoidal sediment waves.

Palaeo-tidal conditions

After the Last Glacial Maximum at 21 ka BP, temperatures evolved gradually and resulted in the retreat of the last British-Irish Ice Sheet significantly changing ocean tidal dynamics (Clark et al., 2012). In the central part of the Irish Sea, tidally induced bed shear stresses peaked between 7 and 10 ka BP due to enhanced ocean tidal dynamics and local configurations. The further retreating ice sheet resulted in substantial sea-level rise and a declining bed shear stress (Uehara et al., 2006; Ward et al., 2016). During this period, the predicted bed load transport directions in the central Irish Sea changed to the present-day environment which is associated with a nearly symmetrical tide and bed load divergence and convergence zones. Together with peak bed stresses, the nearly symmetrical tide and the long-term reversals (on a millennial scale) of tidally induced bed stresses in dominant direction are suspected to have contributed significantly to the bi-directionally piling up of coarse sediment and thus the formation of trochoidally-shaped sediment waves in these zones (Valentine et al., 2002; Van Landeghem et al., 2009a). After 5 ka BP, it is assumed that the trochoidal sediment waves in the Irish Sea became moribund since hydrodynamics stabilised (Uehara et al., 2006).

Glacial incisions

A continuous mobile sediment supply turns out to be crucial for the further growth of trochoidal sediment waves (Van Landeghem et al., 2013). During the glacial period in the Mid and Late Quaternary, the Irish Sea documented three major phases of glacial incisions due to the progressing icesheet (Jackson et al., 1995). This continuous supply is most probably from sediments infilling these glacial incisions which turn out to overlap with trochoidal sediment wave fields. This is also mentioned by Barrie et al. (2009). This process is triggered due to converging sediment transport paths in the bedload parting zone and due to scouring around nearby sediment waves which consist of coarse particles (Van Landeghem et al., 2009a) and is potentially strengthened by the formation of standing internal waves due to stratification (Cartwright, 1959).

Enhanced hiding-exposure effect

The hiding-exposure effect represents the process in which larger and more exposed grains hide the smaller particles from the flow (McCarron et al., 2019). This effect is enhanced in poorly sorted mixtures which increases bedform growth rates. Furthermore, the contribution of the hiding-exposure effect is most-likely time-dependent since mixed seabed sediments are gradually sorted during the formation and evolution of bedforms. In general, gravel and silt mixtures are more poorly sorted than sand due to its weight and clustering, respectively. Trochoidal sediment waves have a coarser and more poorly sorted nature compared to sand waves. It is therefore possible that the hiding-exposure effect initially enhanced the trochoidal sediment wave growth significantly in combination with the strong palaeo-tidal conditions (Van Landeghem et al., 2013).

3

Delft3D model description

In this chapter the basics of the Delft3D model are described. In Section 3.1, the Delft3D model is described briefly. Subsequently, the model set-up is discussed. Furthermore, the formulations of hydrodynamics, sediment transport and morphology as used in this study in the Delft3D-4 model are shown.

3.1. Basics of Delft3D

The complex numerical shallow water model Delft3D is a process based model developed by Deltares. The system of equations consists of the shallow water equations, flow- and sediment continuity equations and sediment transport equations. The model can be used to simulate sand wave morphodynamics in which various physical processes (e.g. wind- and wave-driven currents, density gradients, sediment transport, advanced turbulence models) can be incorporated in an advanced manner (Lesser et al., 2004). Such a model can be operated to investigate sand waves in multi-layer mode, i.e. 2DV or 3D, in which hydrodynamics, sediment transport and bed evolution are coupled and updated consecutively after each time step (Figure 3.1). High spatial and temporal resolution, that is required, results in a relatively large computation time which generally limits 3D model application for sand wave studies (Borsje et al., 2013). In the remainder of this chapter we limit to a summarised model description and refer the interested reader to the user manual for a detailed description (Deltares, 2022).

3.2. Numerical model parameters

The calculation grid of the 2DV-model consists of a variable resolution in both the horizontal (x -coordinates) and vertical (z -coordinates) direction. The model set-up is initially based on the set-up used by previous studies (Van Gerwen et al., 2018; Damveld et al., 2020b) and is optimised for this work using a sensitivity analysis, see Chapter 5. The total horizontal length of the modelling domain equals 50 km. The central

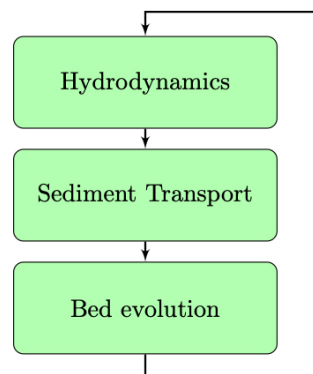


Figure 3.1: The morphodynamic loop, showing interactions among hydrodynamics, sediment transport and bed evolution. The three elements in morphodynamical systems interact forming a closed loop, which may result in complicated feedback mechanisms (Campmans, 2018).

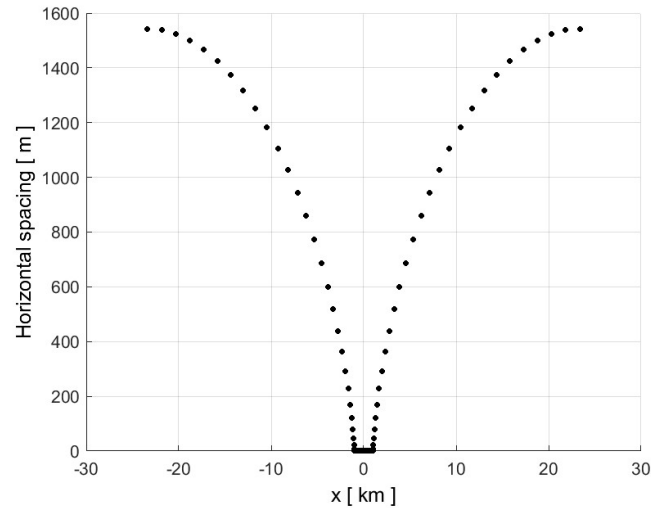


Figure 3.2: The horizontal grid spacing for Delft3D-4 model runs with a fine evenly-distributed grid in the centre ($\Delta x = 2\text{ m}$) at which sediment waves are present and a coarser grid towards the lateral boundaries.

part of this domain is considered the area of interest and contains a number of evenly distributed grid cells of width Δx . For a grid spacing of $\Delta x = 1\text{ m}$ Van Gerwen (2016) showed that the model run becomes inaccurate. To avoid possible inaccuracies and to reduce calculation times, a relatively coarse horizontal grid $\Delta x = 2\text{ m}$ of the finer part was used following Van Gerwen et al. (2018) and Damen et al. (2018).

The number of grid cells in the finer part of the domain affect the computation time and are therefore based on the (preferred) wavelength of the system for each case such that at least three complete sediment waves are present to reduce undesired side effects. The horizontal spacing between the grid cells outside the area of interest gradually increases towards a coarser grid, i.e. $\Delta x = 1,550\text{ m}$ at the lateral open boundaries, see Figure 3.2.

For the vertical schematization two options are available in both models: z - or σ -coordinates. For this study the σ -coordinates are chosen, as they give a better representation of the actual bed level. This means that equations for the hydrodynamics of (Section 3.3) are converted to the σ -grid. The z - and σ -grid are illustrated in Figure 3.3. The definition of water level and depth are shown in Figure 3.4. The number of 60 sigma-layers was unchanged since Van Gerwen (2016) showed that the equilibrium time-scale and wave height are both significantly sensitive to variations of this number. However, the distribution of the sigma-layers was adjusted to obtain an equally high near-bed resolution for an increasing water depth in comparison to previous modelling studies, see Section 6.1.

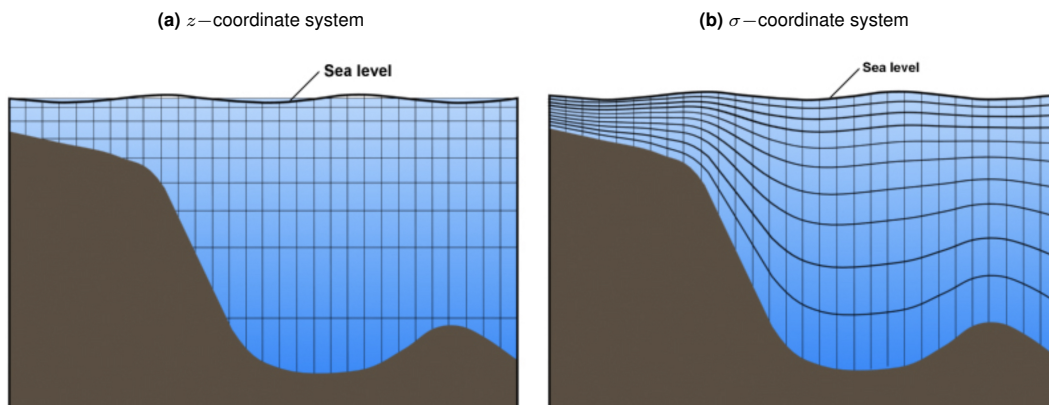


Figure 3.3: z - and σ - vertical coordinate system used in the Delft3D model. Images originally from the COMET program.

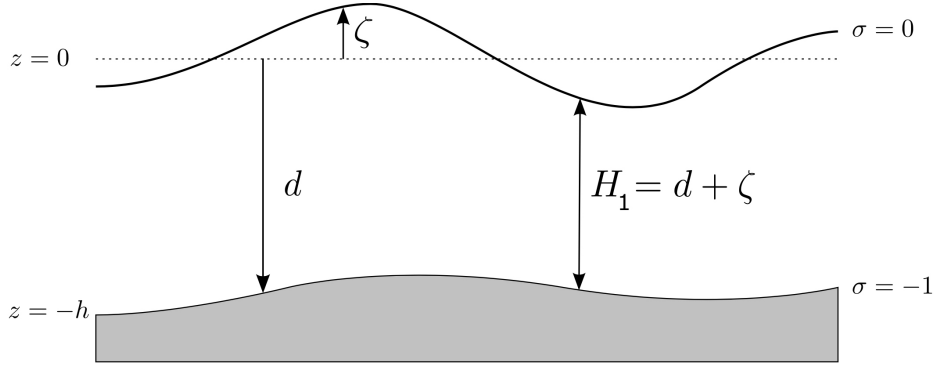


Figure 3.4: Definition of water level (ζ), water depth (d) and total water depth (H_1) (Deltares, 2022).

3.3. Hydrodynamics

The system is forced by a symmetrical tide, i.e. the principal semidiurnal solar (S_2) tidal constituent with angular frequency $\sigma_{S_2} = 1.45 \cdot 10^{-4} s^{-1}$. Accordingly, a depth-averaged tidal velocity amplitude U_{S_2} is attained at the boundaries. Despite the fact that the semidiurnal lunar tide is the most dominant constituent in the Irish Sea, the semidiurnal solar tidal constituent is preferable as it is easier to post-process.

Moreover, Riemann boundary conditions are imposed which allow outgoing waves to traverse the boundaries without reflection (Verboom & Slob, 1984). Residual currents are neglected in this modelling study, i.e. $U_{S_0} = 0 ms^{-1}$, as this results in asymmetrical sediment waves and migration. Therefore, migration of sediment waves is not taken into account. Furthermore, boundary-related effects in relation to hydro- and morphodynamics can be neglected as a result of the adequate distance between the area of interest and the lateral boundaries. A spin-up time of one tidal cycle is applied during which bed level changes are switched off. Afterwards bed load transport, slope-induced transport and suspended load transport is able to induce bed level changes.

The hydrodynamics are described by the shallow water equations supplemented with appropriate boundary conditions. The vertical momentum equation is reduced to the hydrostatic pressure relation as vertical accelerations are assumed to be small compared to gravitational acceleration. Turbulence is represented by a spatiotemporally varying vertical eddy viscosity (see below). For this study, sand waves are assumed to be perpendicular to the rectilinear tidal velocities. Following a 2DV approach we consider variations in the horizontal x and vertical z direction only, thus ignoring typical 3D-processes such as the Coriolis effect and wind forcing. In terms of the σ -coordinates, the 2DV hydrostatic shallow water equations are described by

$$\frac{\partial u}{\partial t} + u \frac{\partial u}{\partial x} + \frac{\omega}{(d + \zeta)} \frac{\partial u}{\partial \sigma} = -\frac{1}{\rho_0} P_u + F_u + \frac{1}{(d + \zeta)^2} \frac{\partial}{\partial \sigma} \left(v_T \frac{\partial u}{\partial \sigma} \right), \quad (3.1)$$

$$\frac{\partial \omega}{\partial \sigma} = -\frac{\partial \zeta}{\partial t} - \frac{\partial [(d + \zeta)u]}{\partial x}. \quad (3.2)$$

Here, u is the horizontal velocity, ω is the vertical velocity relative to the moving vertical σ plane, ρ_0 is the reference water density, d is the depth below some horizontal plane of reference (datum), ζ is the free surface elevation, P_u the hydrostatic pressure gradient, F_u describes the horizontal exchange of momentum due to turbulent fluctuations, and v_T the vertical eddy viscosity.

The above equations are solved using boundary conditions at bed level and the free surface. Assuming an impermeable bed and free surface, the kinematic vertical boundary conditions are both set to zero and are found as shown in Equation 3.3. The dynamic boundary conditions, representing the stresses at the bed level and at the free surface are shown in Equation 3.4 and Equation 3.5. At the bed ($\sigma = -1$) and the free surface ($\sigma = 0$), a quadratic friction law and a no-stress condition (neglecting

wind-stress) is applied, respectively, i.e.

$$\omega|_{\sigma=-1} = 0, \quad \omega|_{\sigma=0} = 0, \quad (3.3)$$

$$\tau_b \equiv \rho_0 \frac{v_T}{(d + \zeta)} \frac{\partial u}{\partial \sigma} \Big|_{\sigma=-1} = \rho_0 u_* |u_*|, \quad (3.4)$$

$$\rho_0 \frac{v_T}{(d + \zeta)} \frac{\partial u}{\partial \sigma} \Big|_{\sigma=0} = 0, \quad (3.5)$$

in which τ_b is the bed shear stress and u_* is the shear velocity that relates the velocity gradient at the bed to the velocity u in the lowest computational grid point by assuming a logarithmic velocity profile.

3.3.1. Roughness formulation

To calculate the bed shear stress τ_b a formulation for the bed roughness is required. In this 2DV-modelling study the Chezy roughness formulation is used. The bed shear stress is then computed as shown in Equation 3.6.

$$|\vec{\tau}_b| = \rho_0 \vec{u}_* |\vec{u}_*| = \frac{\rho_0 g \vec{U} |\vec{U}|}{C^2}, \quad (3.6)$$

where $|\vec{U}|$ is the magnitude of the depth-averaged horizontal velocity and C is the user defined Chezy coefficient that describes the bottom roughness. Assuming hydraulically rough conditions, the White-Colebrook equation is used, i.e.

$$C = 18 \log \left(\frac{12H_1}{k_s} \right), \quad (3.7)$$

in which H_1 is the total water depth ($H_1 = d + \zeta$; d positive downward) and k_s the Nikuradse roughness length. Despite its dependency on the water depth and grain size diameter, the Chezy roughness value is kept constant in space and time during the entire simulations for this modelling study. Following Cherlet et al. (2007), the roughness length can be evaluated by

$$k_s = 202dR_p^{-0.369}, \quad (3.8)$$

in which the Reynolds number R_p is evaluated by

$$R_p = \frac{\sqrt{(\rho_s/\rho_0 - 1)gd^3}}{\nu}, \quad (3.9)$$

where ν is the kinematic viscosity of water. In the remainder of this study the values $\rho_s = 2,650 \text{ kg m}^{-3}$, $\rho_0 = 1,050 \text{ kg m}^{-3}$ and $\nu = 10^{-6} \text{ m}^2 \text{ s}^{-1}$ are used.

3.3.2. Turbulence formulation

The vertical eddy viscosity ν_T is calculated by means of the $k - \epsilon$ turbulence closure model as recommended by Borsje et al. (2013) in which both the turbulent energy k and the dissipation ϵ are computed (Rodi, 1984). The resulting vertical eddy viscosity ν_T is variable both in time and space. For details on the $k - \epsilon$ turbulence model formulations, see Burchard et al. (2008).

3.4. Sediment transport

3.4.1. Sediment transport formulation

The bed load transport of sediments, S_b is calculated by Van Rijn (1993) following previous studies. Its magnitude is corrected for the bed slope and is calculated with Equation 3.10.

$$|S_b| = 0.006\alpha_s\rho_s w_s D_{50} M_s^{0.5} M_e^{0.7} \quad (3.10)$$

In this formulation α_s is a correction factor for the bed slope. ρ_s is the density of the sediment, w_s is the particle settling velocity and D_{50} is the median diameter of the sediment. M_s represents the sediment mobility number and M_e the excess sediment mobility number which are calculated with Equation 3.11.

$$M_s = \frac{u_r^2}{(\rho_s/\rho_0 - 1)gD_{50}}, \quad M_e = \frac{(u_r - u_{cr})^2}{(\rho_s/\rho_0 - 1)gD_{50}}, \quad (3.11)$$

In this formulation u_{cr} represents the critical depth averaged velocity for initiation of motion, which is based on the Shield's curve. The velocity u_r is the magnitude of the equivalent depth averaged velocity, computed using the velocity in the bottom computational layer and assuming a logarithmic velocity profile. If u_r is lower than the critical velocity u_{cr} , the bed load sediment transport is set to zero. The suspended load transport of sediments, S_s is calculated by

$$S_s = \int_a^{d+\zeta} \left(uc - \varepsilon_{s,z} \frac{\partial c}{\partial z} \right) \partial z, \quad (3.12)$$

where a is the reference height and c is the suspended sediment mass concentration. The reference height $a = 0.01H_1$ characterises a transitional level between two transport modes. Sediment transported below the reference height is regarded as bed load transport as it responds almost instantaneously to changing flow conditions (Van Rijn, 2007). Transport above this height is considered to be in suspension. The suspended sediment concentration is calculated by solving the advection–diffusion equation, i.e.

$$\frac{\partial c}{\partial t} + \frac{\partial(cu)}{\partial x} + \frac{\partial(w - w_s)c}{\partial z} = \frac{\partial}{\partial x} \left(\varepsilon_{s,x} \frac{\partial c}{\partial x} \right) + \frac{\partial}{\partial z} \left(\varepsilon_{s,z} \frac{\partial c}{\partial z} \right), \quad (3.13)$$

where w is the vertical velocity (Cartesian coordinate system), w_s is the sediment settling velocity. Further, $\varepsilon_{s,x}$ and $\varepsilon_{s,z}$ are the sediment diffusivity coefficients in x and z direction, respectively. For further details on initial and boundary conditions (e.g. pickup and deposition), and the relation between the vertical velocities w [Eq. (3.13)] and ω [Eq. (3.1)], we refer the reader to the manual (Deltares, 2022).

3.4.2. Bed slope effect

The sediment transport is corrected for the bed slope using the factor α_s . To calculate this factor a formulation by Bagnold (1966) is used, which is shown in Equation 3.14.

$$\alpha_s = 1 + \alpha_{BS} \left(\frac{\tan(\phi)}{\cos(\tan^{-1}(\frac{\partial z}{\partial x})) (\tan(\phi) + \frac{\partial z}{\partial x})} - 1 \right), \quad (3.14)$$

where α_{BS} is a slope effect parameter, ϕ is the internal angle of friction of the bed material and $\partial z/\partial x$ is the bed slope in the direction of the flow. The slope effect parameter α_{BS} is a non-physical parameter which corrects the magnitude of the bed load transport for slope effects. This parameter is mainly used as a tuning parameter.

3.5. Bed evolution

3.5.1. Bed evolution formulation

Finally, the bed evolution is governed by the sediment continuity equation (Exner equation), which reads

$$(1 - \varepsilon_p) \frac{\partial z_b}{\partial t} + \frac{\partial(S_b + S_s)}{\partial x} = 0, \quad (3.15)$$

in which $\varepsilon_p = 0.4$ is the bed porosity, S_b the bed load transport [Eq. (3.10)], and S_s the suspended load transport [Eq. (3.12)]. Equation 3.14 simply states that convergence (or divergence) of the total transport rate must be accompanied by a rise (or fall) of the bed profile (z_b).

Morphological changes occur on a much larger time-scale than the hydrodynamic changes. Therefore a morphological acceleration factor (MF) is introduced. This allows for faster computations by multiplying the bed evolution after each time step by the factor (Lesser et al., 2004). A morphological acceleration factor of 2,000 means that the bed evolution is multiplied by a factor 2,000. If the model calculates one tidal period (considering a tidal period in the order of 12 hours), the morphological evolution is then simulated over 2.7 years. A sensitivity analysis is used to determine the appropriate/maximum MF , given that the model results are still independent of the MF (Ranasinghe et al., 2011).

3.5.2. Active layer and bed stratification

To model bed stratification a shallow sea of average reference depth H_0 , with a sandy seabed consisting of cohesionless sediments on top of an unerodible bedrock layer is considered in Figure 3.5. Through a 2DV approach, a Cartesian coordinate system (x, z) with the x -coordinate pointing horizontally and the z -coordinate pointing upward is defined, corresponding to the velocity components u and w , respectively. The exchange of sediments between the bed and water column is modelled by means of an extended version of the classical active layer approach (Hirano, 1971; Ribberink, 1987). In the classical approach, it is assumed that the seabed consists of two layers: the active layer (formally the dynamical active layer (Church & Haschenburger, 2017)) with constant thickness L_a and the substrate underneath the active layer. The total available sediment thickness L_{tot} may vary in space and time, but is initially spatially uniform. All layers are assumed to be well-mixed and only the sediments in the active layer are instantaneously available for transport.

While the active layer approach is suitable for the initial formation of sand waves, as shown by Van Oyen & Blondeaux (2009a) and Van Oyen & Blondeaux (2009b), the method is unable to describe the vertical sedimentary structure (e.g. the internal history) of a sand wave in the finite-amplitude stage. Therefore a layered approach to the passive substrate is also applied in order to allow for bed stratification (Deltares, 2022). The substrate is divided into a number N of (well-mixed) underlayers

of thickness c and maximum thickness $L_{u,max}$, and a (well-mixed) baselayer. The thickness of the baselayer L_b follows from the total sediment thickness L_{tot} minus the combined thickness of the active layer and underlayers.

Figure 3.5 illustrates the procedure of deposition and erosion within the layered bed. Deposition leads to a flux of sediments from the active layer towards the underlayers. If the top underlayer reaches its maximum thickness $L_{u,max}$, a new (top) underlayer is created and the bottom underlayer merges with the base layer. Conversely, in case of erosion, the active layer will be replenished from the top underlayer. Depending on the amount of erosion, the top underlayer may disappear and the process will continue with the next underlayer. Note that in case of deposition this implementation neglects the contribution of the bed load to the sediment flux towards the substrate, which would physically more realistic (Parker et al., 1982). Nonetheless, this approach has been successfully applied in modelling studies in the riverine (Williams et al., 2016), estuarine (Van der Wegen et al., 2011) and coastal (Reniers et al., 2013; Huisman et al., 2018; Damveld et al., 2020b) environments.

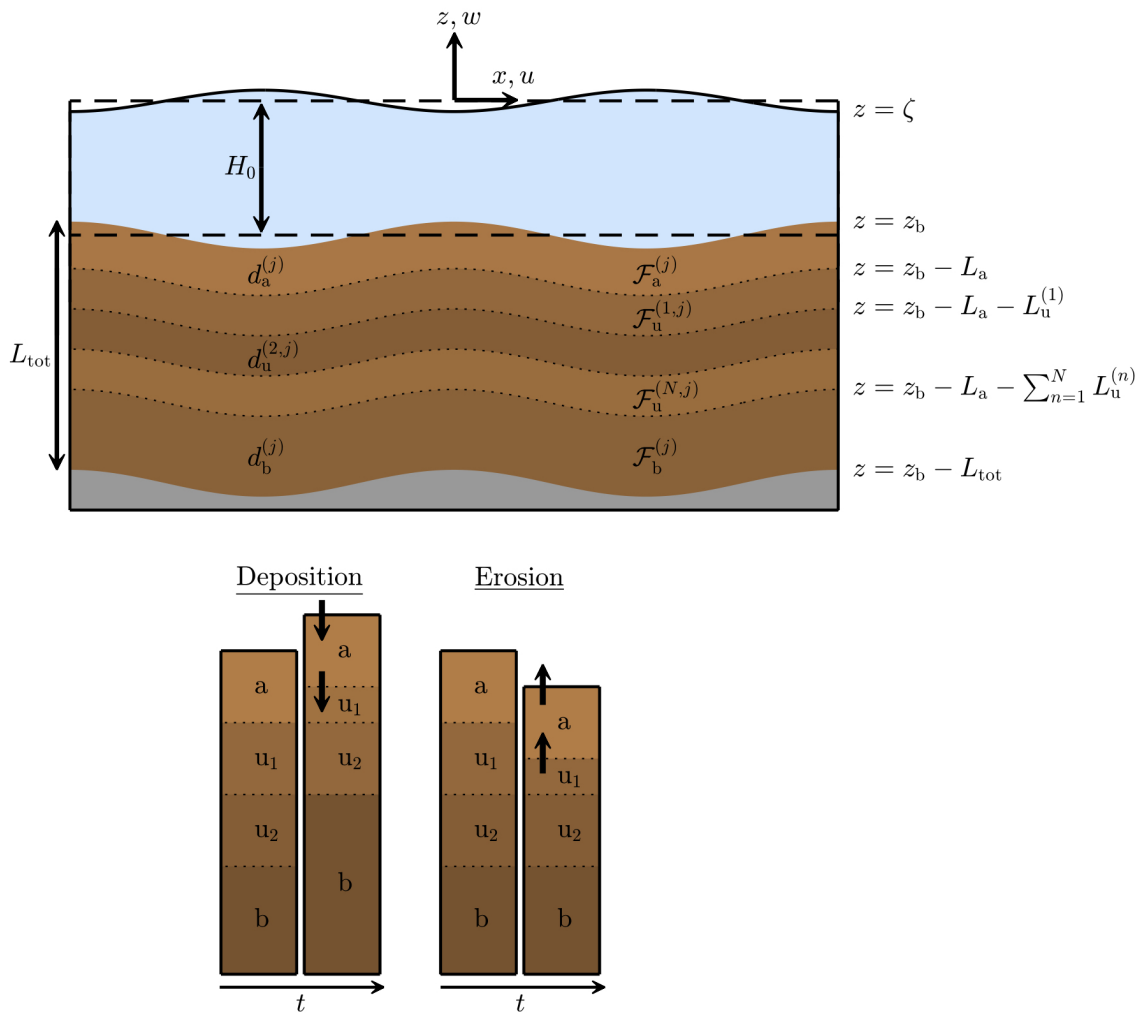


Figure 3.5: (top) Side view of the water column and stratified bed, illustrating the coordinate system (x, z) with corresponding velocity components (u, w) , bed level z_b , free surface level ζ , and average depth H_0 . Within each layer (n) the grain-size class (j) is characterized by a grain size d and mass sediment fraction F . The thickness of the layers is indicated by L , where the subscripts a, u, b, tot refer to the active layer, underlayer, base layer, and total layer, respectively. The gray area below denotes the unerodible bedrock layer. (bottom) Deposition and erosion process for a total number of underlayers $N = 2$. Note that in the deposition example the layers are rearranged due to the new top underlayer ($u_1 \rightarrow u_2$), the lowest one being absorbed by the base layer (Damveld et al., 2020b)

4

Data-analysis

This chapter describes the data-analysis prior to the modelling phases. First, the model output of the GIA model and the data from the AmSedIS project are described. Subsequently, the data is analysed for correlations and trends. It should be noted that this chapter partially contains unpublished work by Van Landeghem.

4.1. Description of data

4.1.1. GIA model output

The outputs from the model of Uehara et al. (2006) were extracted for the palaeo-hydrodynamics at grid cells closest to the survey areas of the AmSedIS project, see Figure 4.1. The palaeo-tidal reconstructions were generated using palaeo-bathymetries for every 1,000 years from 16 ka BP to the present day in a 2D model which has a resolution of 1/12 degrees. Here, the Lambeck (1995) Ocean Tide (LOT) model was used as this was advised by the main author (Van Landeghem et al., 2009a). In this model, the North Channel was still open at 15 ka BP in comparison to the Peltier (1994) glacial isostatic adjustment (GIA) model. Figure 4.2 shows the retreating ice for several time frames using this LOT GIA model. Additionally, the reconstruction of the bed stress vectors is presented. The bed load parting zones which are considered vital for the formation and evolution of trochoidal sediment waves are clearly visible near the survey areas. The model output consists of water depths, tidal symmetry and direction and peak tidally induced bed shear stresses. Here, the peak value of bed stress vectors were extracted during each model run (ca. 29.5 days, two fortnights) as tide-averaged sediment transport is directed towards the highest current velocities.

4.1.2. AmSedIS data

At several locations in the Irish Sea during a survey of the AmSedIS project in April 2012, inter alia, high resolution swath bathymetry and sampling data of 22 sediment waves have been collected with a multibeam echosounder (MBES) and Shipek grab, respectively. An overview of the survey areas with the spatial variation in mean grain size is presented in Figure 4.1.

The sediment waves were measured for its geometry and migration rate using bathymetry data. A schematic representation of sediment waves shows the different geometrical parameters used in this study (Figure 2.2). Two types of sediment waves have been distinguished based on their cross-sectional shape, that is, the “normal” and “trochoidal” type. This study only focuses on extremely large trochoidal sediment waves, i.e. $\Delta S > 10 m$.

Sediment wave migration rate was determined by the changing crest position over a time interval using periodic swath bathymetry data and was expressed as an annual average in m/year. The time interval between surveys was generally one to several years. The sediment wave height ΔS was measured vertically from the base to the sediment wave crest. Its wavelength was derived from sediment wave trough spacing (L) rather than crest spacing, since trochoidal sediment waves are found in isolation. The water depth at the base of the sediment wave was derived from the sum of the water depth of the crest $h(cr)$ and the wave height.

For each sediment wave a transect of at least 4 to a maximum of 10 samples of surficial seabed sediments have been collected during the surveys using a $0.04 m^2$ Shipek grab. The grain size

measurements were executed through sieving or laser granulometer of the sample particles. To classify the sedimentary environment of the sediment waves this dataset was further analysed using GRADISTAT: a grain size distribution and statistics package (Blott & Pye, 2001). This package calculates arithmetically, geometrically and logarithmically a considerable number of statistical parameters from the grain size measurements using moments statistics. This study focuses on the logarithmic phi scale since it is used for log-normal distributions which are generally applied by sedimentologists. The phi scale is expressed as $\phi_i = -\log_2(d_i/d_{ref})$, where d_i indicates the grain size of the i -th percentage and d_{ref} the reference grain size, both in millimetres (Krumbein, 1934). Hereinafter, sediment types are classified based on Wentworth (1922).

4.2. Observations from the AmSedIS project

4.2.1. Palaeo-tidal conditions

The palaeo-tidal reconstruction of water depths and maximum tidally-induced bed shear stresses close to the survey areas at which trochoidal sediment waves were observed during the AmSedIS project (Table 4.1) is shown in Figure 4.3. Both figures 4.3a and 4.3b show a clear trend.

The modelled water depths increase over time due to the melting British-Irish Ice Sheet as is visualised in Figure 4.2. The reconstruction shows that the ice retreated at 11 ka BP at the survey areas 8 which is relatively close to Area 9, while other survey areas were already flooded several thousands of years before. The increasing water depth at all survey areas stagnated around 6 ka BP.

A similar trend is found for the modelled maximum tidally-induced bed shear stresses. The first increase between 12 and 15 ka BP can be linked to enhanced ocean tidal dynamics. A strong increase occurred for all survey areas between 11 and 12 ka BP which lasted until 6 ka BP, most likely due to local configuration changes (in combination with ocean tidal dynamics) as is stated by Van Landeghem et al. (2009a). Hereafter, the stresses converged towards present-day values, i.e. $\tau_{b, \max} = 2.5 - 7.0 \text{ Nm}^{-2}$. Van Landeghem et al. (2009a) also mentioned local enhancements due to the open North Channel which might explain the peaks in bed shear stress between 12 and 16 ka BP at several survey areas.

4.2.2. Present-day trochoidal sediment waves

In this section the data obtained during the AmSedIS project is analysed. First, the bathymetry data is visualised and the trochoidal sediment waves are distinguished and investigated. Subsequently, grab sample data is examined. At last, significant correlations between trochoidal sediment wave

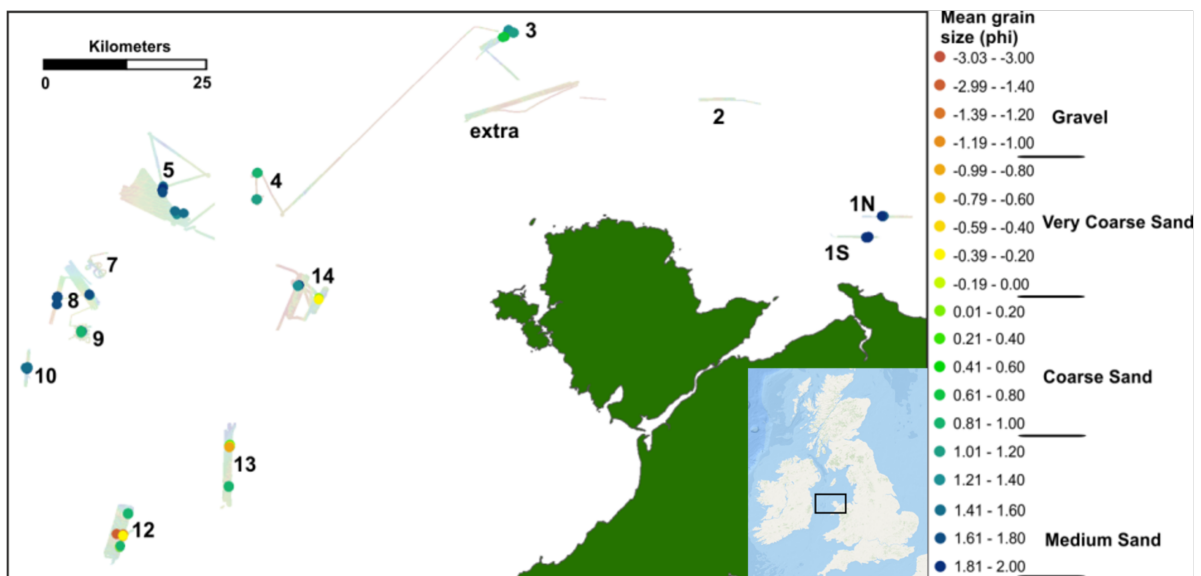


Figure 4.1: Overview of survey areas in the Irish Sea during the AmSedIS project in April 2012 with mean grain sizes of combined individual grain size distributions along sediment waves (Van Landeghem et al., 2013).

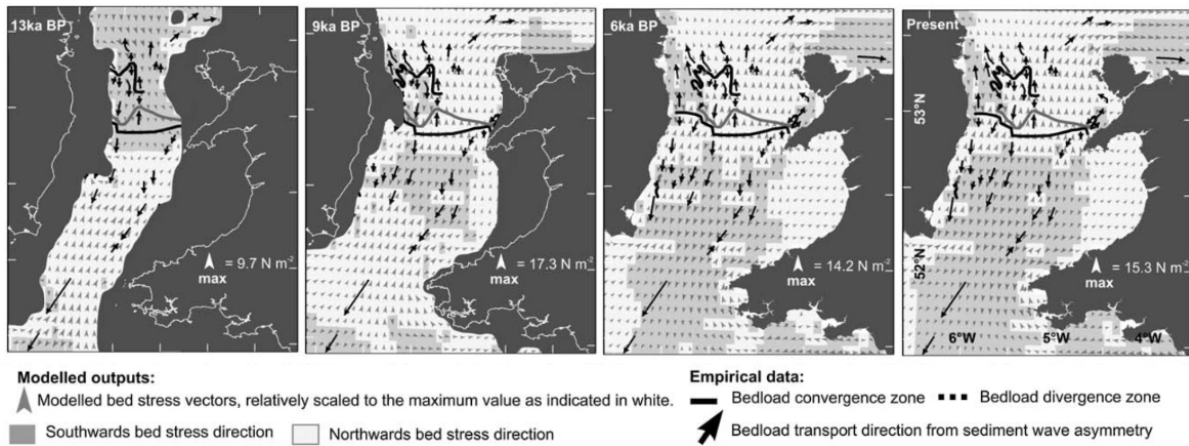


Figure 4.2: Empirically observed bedload transport patterns in the Irish Sea with modelled bed stress vectors from the Lambeck (1995) ocean-tide GIA model for the periods 13ka, 9ka and 6 ka BP and the present-day (Van Landeghem et al., 2009a).

characteristics and grain size distributions are analysed.

Wave characteristics

In total, trochoidal sediment waves at seven survey areas are identified based on their (nearly) symmetrical shape, sharp crest and significant height ($\Delta S > 10 m$). The trochoidal sediment wave characteristics with the corresponding water depth at these survey areas are shown in Table 4.1. The migration rate of the trochoidal sediment waves ranges from no migration to several metres per year. Most likely, this migration refers to the mobile sand veneer on top of the coarse core as is described by Van Landeghem et al. (2009a). A wide range of wave heights is measured, i.e. 11 to 35 metres, whereas wavelengths extend from 340 to 560 m. Also, water depths at the survey area vary considerably. A plan view of the bathymetry and a cross-section for each survey area can be found in Appendix B.

The visualised bathymetry data shows that the trochoidal sediment wave at Area 4N is isolated, whereas the sediment waves at the other survey areas are observed in a sequence. This sequential pattern is particularly visible at Areas 9, 12M, 13N and 14E, while it seems more irregular at Areas 3-3 and 14W. Furthermore, "normal" sediment waves are observed flanking the trochoidal sediment waves at the Areas 3-3, 9, 12M and 13N. These normal sediment waves are significantly lower in height.

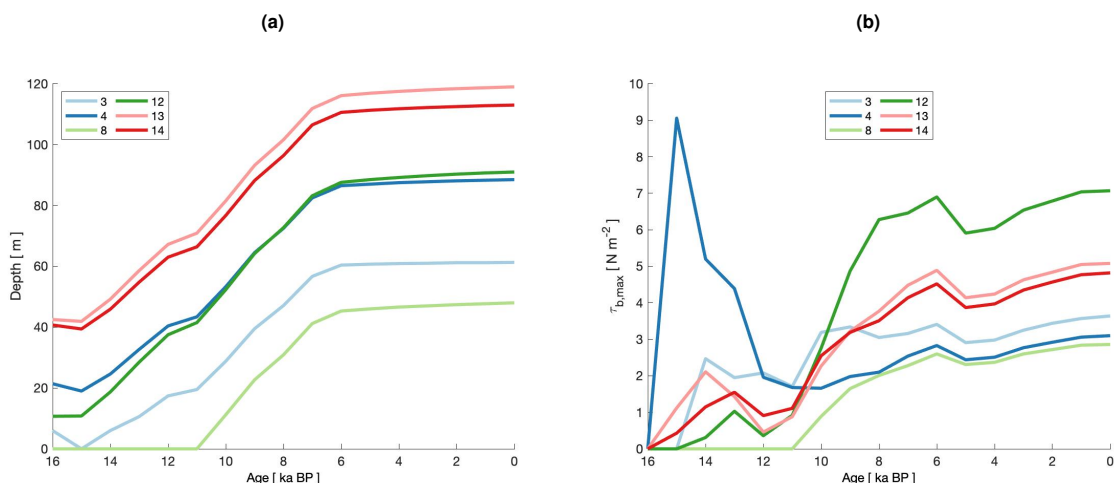


Figure 4.3: Palaeo-tidal reconstruction of (a) water depths and (b) maximum tidally-induced bed shear stresses for every 1,000 years from 16,000 years to present-day. Model results were chosen at grid cells closest to the survey areas at which trochoidal sediment waves were observed during the AmSedIS project, April 2012. The Lambeck (1995) GIA model was used with ocean-tide open boundaries (Uehara et al., 2006).

Table 4.1: Measured trochoidal sediment wave characteristics from MBES data at several survey areas during the AmSedIS project, April 2012; migration rate c_{mig} , wave height ΔS , wavelength L with components L_1 and L_2 and water depth d as the sum of the distance from the sediment wave crest to the surface water and the wave height.

Survey area	c_{mig} [myr^{-1}]	ΔS [m]	L [m]	L_1 [m]	L_2 [m]	d [m]
3-3	1.06	14	340	210	130	77
4N	0.00	11	440	190	250	89
9	0.59	19	360	220	140	70
12M	2.68	35	560	300	260	100
13N	1.95	24	500	310	190	111
14E	0.39	20	360	180	180	160
14W	0.26	26	460	270	190	135

Grab samples

Several grab samples were taken along trochoidal sediment waves in the Irish Sea. The individual grain size distributions and the locations of the grab samples per survey area are shown in Appendix B. First, the four main shape parameters of the individual grain size distributions were analysed, that is, the central tendency (mean grain size), dispersion (sorting), symmetry (skewness) and peakedness (kurtosis).

A relationship between mean grain size and sorting of the individual particle size distributions is demonstrated for the different survey areas in Figure 4.4a. Here, it is noted that the particle distributions for Area 14W (and one for Area 12M) can be considered outliers. Their distributions show an excessive amount of silt. Since this study focuses mainly on gravel and sand, the silt is removed from the particle distributions and the shape parameters are recalculated. Subsequently, the mean grain size and sorting strongly correlate ($r = -0.65$) with high confidence ($p < 0.01$). The mean grain sizes of the individual distributions along the trochoidal sediment waves are widespread and range from gravel to medium sand. In line with the mean grain sizes, the sortedness of the distributions along the trochoidal sediment waves is widely dispersed from very well to very poorly sorted samples.

Figure 4.4b shows the relation between the skewness and kurtosis of the different grain size distributions. Again with a high level of confidence ($p < 0.01$), a (moderate) negative correlation ($r = -0.45$) is found between the skewness and kurtosis. The spread of skewness is significantly wide and is categorized from very coarse (positively) skewed to very fine (negatively) skewed. Meanwhile, the kurtosis of the individual distributions along trochoidal waves varies considerably from very platykurtic to extremely leptokurtic shape.

Variations in skewness and kurtosis in sediment mixtures can be linked to multimodal distributions, i.e. the mixing of more than one grain size population in different proportions (Cronan, 1972). Except for the unimodal grain size distributions of Area 4N, these multimodal distributions can also easily be noticed for each location in Appendix B. Multimodality and the degree of overlapping, or no overlapping at all, can significantly alter the value of the shape parameters when only fitting a single distribution function as is done using GRADISTAT. Thereby, its usability could be questioned. Grain-size components in multimodal sediments indicate different transportation or depositional processes Sun et al. (2002). Therefore, multimodality can affect sediment wave dynamics and knowledge about the grain size distribution at the seabed helps to better understand sediment wave behaviour.

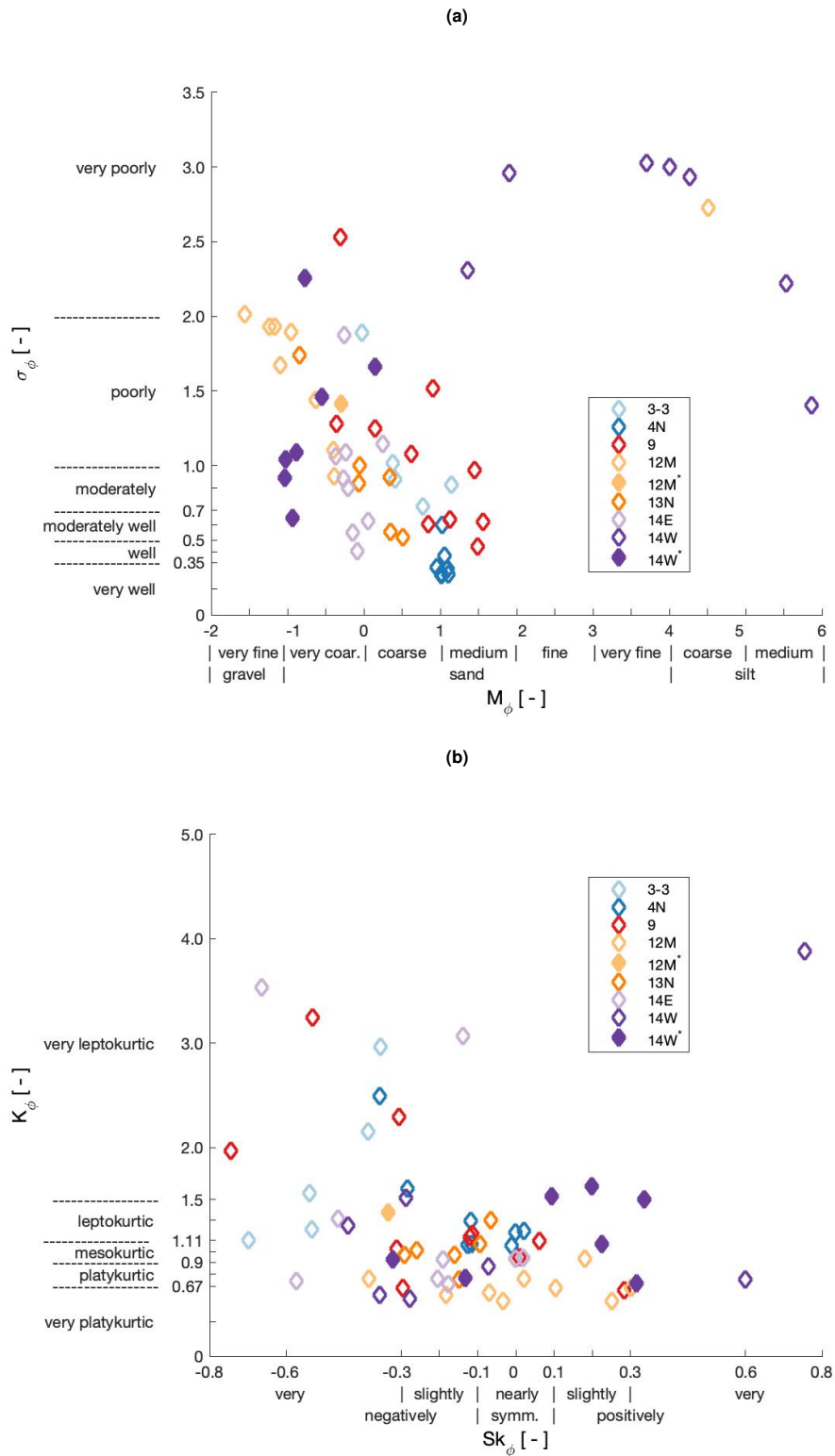


Figure 4.4: The four main shape parameters of the individual grain size distributions, i.e. (a) the central tendency (mean grain size M_ϕ), dispersion (sorting σ_ϕ), (b) symmetry (skewness Sk_ϕ) and peakedness (kurtosis K_ϕ) in logarithmic phi scale (Krumbein, 1934). The mean grain size is classified into gravel, sand and silt after Wentworth (1922). The degree of sorting ranges from very well to very poorly sorted samples. The skewness is categorised from very coarse (positively) to very fine (negatively) skewed, while the kurtosis varies considerably from very platykurtic (flatter with thinner tails) to extremely leptokurtic (flatter with thinner tails) to extremely leptokurtic shapes (higher peaks and fatter tails). Note that the original distributions of Area 12M and 14W are treated as outliers and are modified by removing the silt (Area 12M* and 14W*). Individual grain size distributions follow from grab samples along trochoidal sediment waves during the AmSedIS project, April 2012, and can be found in Appendix B.

The theory states that present-day trochoidal sediment waves can be distinguished between a coarse core and a mobile sand veneer. Therefore, the mean of the first two modes are plotted individually in Figure 4.5 to obtain a diameter range for gravel and sand. It can be seen that the mean of mode 1 generally ranges between $1 < \phi < 2$ which corresponds with medium sand. The second most dominant mode is linked to very fine gravel as its mean mainly lies between $-2 < \phi < -1$. The coarsest sediment is mainly found in the trough in particular near areas of scour, cf. Areas 3, 9, 12M, 13N and 14E. This is likely lag exposed in areas of erosion. However, other significant grain size trends over multiple trochoidal sediment waves are not found.

At last, the correlation between the field averages of the individual distributions and the trochoidal sediment wave height and wavelength are analysed. Whereas no significant correlation is found for the wavelength, the wave height correlates very strongly with the mean of mode 1 ($r = -0.88$) and the deviation of this mean ($r = 0.85$) both with a significant confidence level, i.e. $p < 0.02$.

4.3. Conclusions

The palaeo-tidal reconstruction shows a clear trend of a strong sea level rise and enhanced hydrodynamics between approximately 12 to 6 ka BP due to the retreat of the ice thereby significantly changing the Irish Sea basin. After this, tidal conditions stabilised. More recently, trochoidal sediment waves are observed at the survey areas of the AmSedIS project with wavelengths between 340 and 560 m, whereas their wave heights range from 11 to 35 m. Individual grab samples along these bed features are mainly multimodal with its two most dominant modes corresponding to medium sand and very fine gravel.

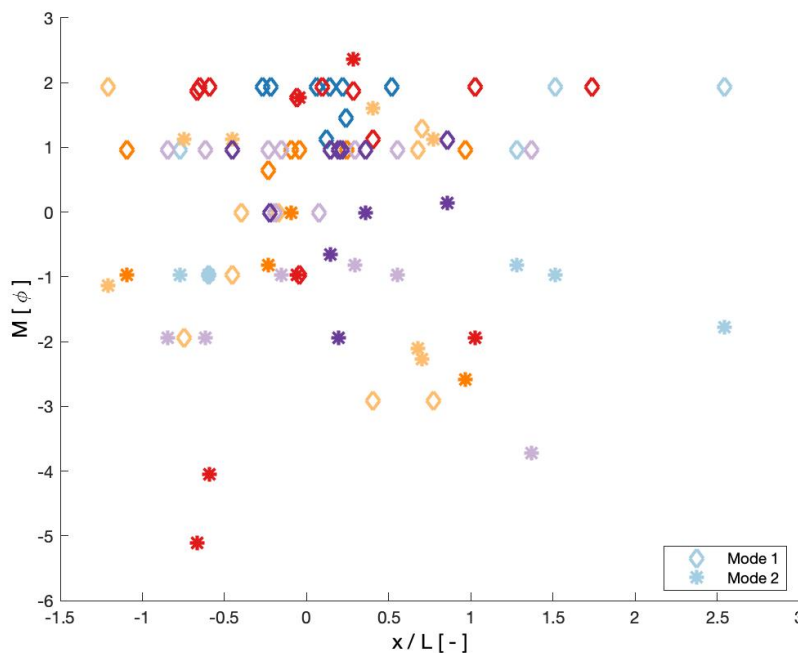


Figure 4.5: The mean grain size in phi-scale along the normalised x-axis. Note that the crest is located at $x = 0$. The left side of the domain $x < 0$ is divided by the wavelength component L_1 , whereas the right side $x > 0$ is divided by L_2 of the corresponding trochoidal sediment wave. Both troughs are therefore at $x/L \pm 0.5$.

5

Sensitivity analysis

Model predictions can be very sensitive to model and process parameters as is already shown by Van Gerwen (2016). Therefore, the aim of this chapter is to discuss the sensitivity of these parameters on gravel wave growth during the small- and finite-amplitude stage. This sensitivity analysis is executed prior to the various cases mentioned in Section 6.1. More detailed results of the individual simulations can be found in succeeding Appendices C (FGM), D (tidally-averaged circulation cells), E (sediment transport) and F (long-term bed level development). To be able to compare the results are normalised. Furthermore, Table 5.1 shows the used parameter values which generally correspond to Case I, see Section 6.1.3.

5.1. Numerical model parameters

First, the influence of the grid on the model outcomes was reduced by conducting a grid refinement study to establish a stable model for the Irish Sea setting. Initial parameter values were assumed based on test simulations and previous sand wave modelling studies, see Table 5.1. The numerical model parameters consist of the horizontal and vertical grid in the 2DV-plane, the hydrodynamic time step and the morphological acceleration factor.

An amount of 1,000 x -points was chosen since the system during the small-amplitude stage mainly showed preferred wavelengths between 100 and 350 m , see Appendix C. With the grid spacing of $\Delta x = 2\text{ m}$, this resulted in 50 to 175 grid cells to describe one sediment wave wavelength which was found to be acceptable.

To optimise the hydrodynamic time step and thus reduce computational times several long-term calculations were performed (not shown here). For a hydrodynamic time step of $\Delta t = 4.5$ and 6 s the run becomes unstable due to excessive velocity changes, which leads to termination of the simulations. The time steps $\Delta t = 1.5$ and 3 s show similar behaviour. Therefore, a hydrodynamic time step of $\Delta t = 3\text{ s}$ was selected.

At last, the sensitivity of the morphological acceleration factor MF or MORFAC was determined based on the finite-amplitude stage as the initial growth showed identical behaviour, see Figure 5.1. The MORFAC was varied between $MF = 125$ and 2,000. For a relatively high MORFAC value of $MF = 2000$ the morphodynamics are updated every 2.74 years, whereas this update occurs every 0.34 years for a $MF = 125$. By decreasing this factor more realistic outcomes are expected since the hydrodynamics are then not updated within this period. However, this also results in a significant increase of computation times. For instance, the computation time of 25 desired simulation years for $MF = 2000$ lasted approximately 7.5 hours, while the simulation for $MF = 125$ lasted circa 5 days. Additionally, the results show that the long-term evolution of sediment waves is sensitive to changes to the MORFAC value.

The bed level development over time in Appendix F indicates that the equilibrium time-scale is significantly lower for higher MORFAC values, while a lower MORFAC produces larger sediment wave heights, more specifically higher positioned crests. Over time, the wave height for lower MORFAC values seems to converge towards circa 12 m before reaching a maximum value, see $MF = 125$ and 250. After reaching this maximum value, sediments are transported from the crest towards the troughs thereby reducing its wave height towards an equilibrium. This process is not particularly observed for higher MORFAC values. Also, the bed level development plots show a flattening and widening of the troughs and a more narrow and symmetrical crest over time for lower MORFAC values.

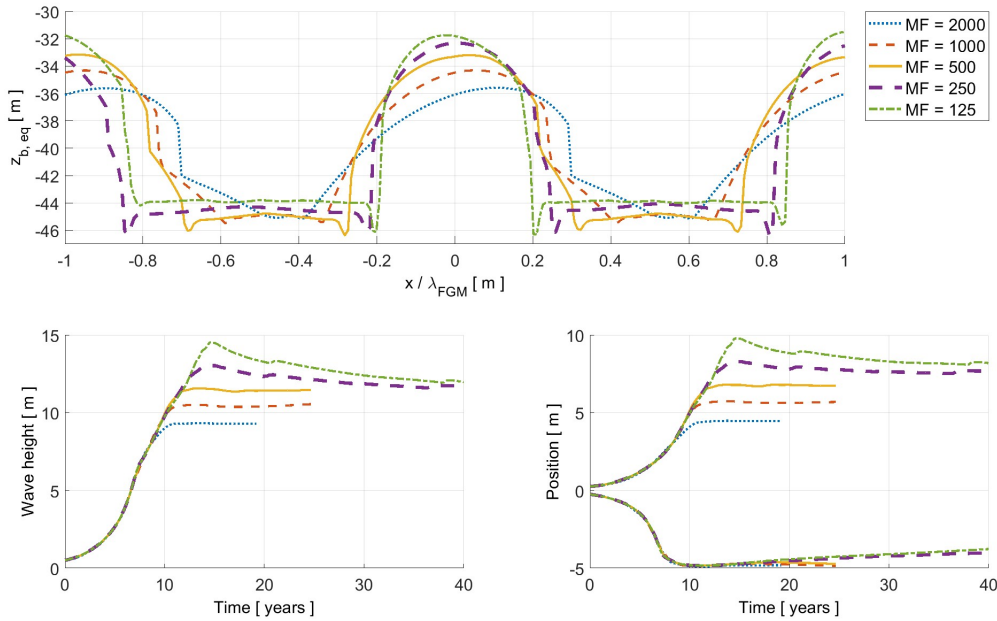


Figure 5.1: Normalised equilibrium bed level $z_{b,eq}$, wave height and crest-trough development for variations in the morphological acceleration factor MF .

5.2. Process parameters

In contrast to the model parameters described in the previous section, process parameters are related to the various processes influencing sediment wave formation and evolution. A sensitivity analysis was executed to show how changes in process parameters affect relevant model outputs. To determine the sensitivity on the small- and finite-amplitude stage of sediment wave growth an initial setting was selected as is shown in Table 5.1. Subsequently, a set of values was chosen for each process parameter, i.e. the slope effect tuning parameter α_{BS} , the Chezy roughness C , the grain size of gravel d_g , the tidal velocity amplitude U_{S2} and the ex- and inclusion of suspension. Here, process parameter values were selected to stimulate sediment wave growth, i.e. positive growth rates during the small-amplitude stage.

A MORFAC value of $MF = 2,000$ was used to reduce computation times significantly. The effect of the MORFAC value on the sediment wave development over time however should not be neglected, see Section 5.1. The next sections are divided into the sensitivity of the process parameters on the small- and finite-amplitude stage of sediment wave evolution.

5.2.1. Small-amplitude stage

Small differences in values of process parameters may lead to an alteration of the sand wave wavelength preferred by the system, i.e. the fastest growing mode FGM (Damveld, 2020). Therefore, the sensitivity of various process parameter during the small-amplitude stage are discussed before simulating towards equilibrium. The results of the individual runs can be found in Appendices C, D and E.

The area of interest consists of sinusoidal sediment waves with initial wave amplitude A_0 as initial topography. This field is multiplied by an envelope function to obtain gradual growth from a flat bed towards a sediment wave field and to therefore minimise undesired side-effects (Figure 5.2). The initial wavelength λ_0 results from the fastest growing mode (FGM), i.e. the wavenumber $k (= 2\pi/\lambda)$ with the largest (positive) growth rate which is assumed to be the preferred mode by the system. Subsequently, the FGM is used as a starting point for the finite-amplitude stage, such that the initial growth stage is omitted and valuable computational resources is saved.

The FGM is determined based on the initial morphodynamic response during one tidal cycle. This response is analysed by the growth rate as a function of the topographic wave number. The wave number k is divided into steps, i.e. $k = 0.010, 0.016, 0.025$ and 0.063 m^{-1} which correspond to $\lambda = 600,$

Table 5.1: Overview of the used values and dimensions of model and process parameters during the sensitivity analysis. The range for the examined parameters is shown as well. Note that the sensitivity of the parameters in turn is analysed.

Description	Symbol	Value	Range	Unit
Number of σ layers	-	60		-
Hydrodynamic time step	Δt	3		s
Grid spacing (finer part)	Δx	2		m
Number of grid cells (finer part)	-	1,000		m
Morphological acceleration factor	MF	2,000	125 – 2,000	-
Reference water depth	H_0	40		m
Initial gravel wave amplitude	A_0	0.25		m
Tidal velocity amplitude	U_{S2}	1.85	1.60 – 1.95	ms^{-1}
Residual current strength	U_{S0}	0		ms^{-1}
Uniform gravel diameter	d_g	3.00	2.50 – 3.50	mm
Slope effect parameter	α_{BS}	3.00	2.50 – 3.50	-
Chezy roughness	C	70	65 – 75	$m^{0.5}s^{-1}$

400, 250 and 100 m , respectively. Hereafter, a fourth-order polynomial is fitted to the calculated growth rates for each wave number. The results show that this number of steps was sufficient to obtain a respectable maximum (positive) value of the polynomial for this setting. The growth rates of initial bed perturbations with varying wavelengths are calculated using $MF = 1$. First, a function for the bed level z_b is formulated using a complex notation, i.e.

$$z_b = \Re\{A \exp(ikx)\}, \quad (5.1)$$

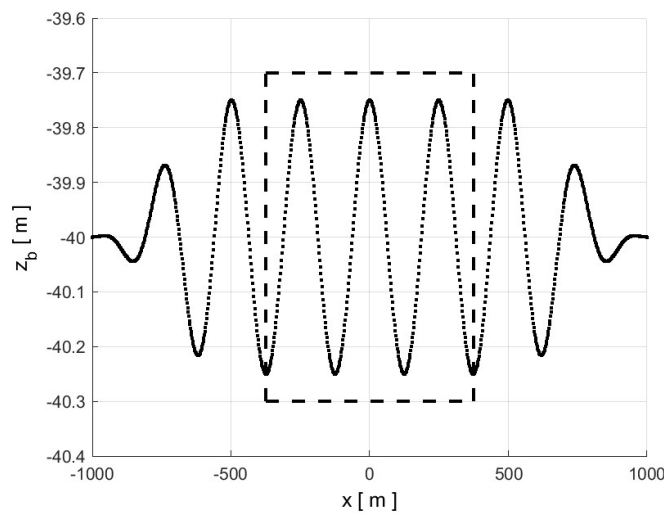


Figure 5.2: Initial topography at the area of interest for Case I with $A = 0.25$ m and $\lambda = 249$ m , i.e. $k \approx 0.025$ m^{-1} . Box indicates $-1.5\lambda \leq x \leq 1.5\lambda$.

where \Re stands for the real part and A represents the complex bed amplitude. Since exponential growth can be assumed during the small-amplitude stage (Besio et al., 2008), the growth rate for the bed perturbation is computed with

$$\gamma = \frac{1}{T} \Re \left[\log \left(\frac{A_1}{A_0} \right) \right] \quad (5.2)$$

in which T is the tidal period, A_0 and A_1 are the initial and calculated bed amplitude, respectively (Borsje et al., 2014b). A Fast Fourier Transform of the most central sand wave in the domain is used to determine the calculated bed amplitude. Positive growth rates indicate sediment wave growth, whereas negative growth rates show decay towards a stable flat bed. The growth rate is dependent on the interactive processes described in Section 2.1.4. Hereafter, the non-linear evolution of sediment waves towards a stable equilibrium is analysed with the initial wavelength λ_0 which follows from the FGM.

It should be noted that changes of the process parameter value affect the preferred sediment wave wavelength of the system. In turn, these bathymetrical alterations disturb the size and strength of the tidally-averaged circulation cells which again influence the preferred wavelength. This feedback mechanism continues until a balance is reached. Consequently, it might be difficult to determine which of these two processes is the dominant source of a particular effect.

Suspended load transport

Suspended load transport is strongly depended on grain size and current strength. Borsje et al. (2014b) showed that the preferred wavelength of sand waves in the North Sea for a relatively large grain size increases by the inclusion of suspended sediment. In this modelling study gravel is used to mimic the Irish Sea setting several thousands of years ago. Also, the current strength is increased in comparison to previous modelling studies to initiate gravel wave growth. Therefore, the effect of suspended load transport is shortly revised.

The FGM plots shows opposite results for the Irish Sea setting compared to the contemporary North Sea, i.e. larger initial growth rates and smaller preferred wavelength while including suspended load transport (Figure C.1a). This might be explained by the reduced phase lag, that is, the settling velocity is significantly larger for gravel. In addition, the normalised circulation cells corresponding to the case with suspended load transport are larger, cf. Figure D.1a and D.1b. This results in lower tidally-averaged bed load transport, yet larger total sediment transport (Figure E.1).

Slope effect parameter

From the FGM results in Figure C.1b, it can be concluded that a lower α_{BS} results in smaller wavelengths corresponding to the FGM λ_{FGM} and larger growth rates. The initial value of $\alpha_{BS} = 3.0$ followed from Van Gerwen et al. (2018). This can be explained by the formulation of α_{BS} which is inversely correlated to the absolute magnitude of bed load transport, see Equations 3.10 and 3.14. Therefore, smaller α_{BS} values constitute more normalised tidally averaged bed load transport (Figure E.3). Also, larger α_{BS} values tend to suppress the steepness of the sediment waves more which result in longer preferred wavelengths.

In contrast, lower α_{BS} and thus smaller λ_{FGM} are accompanied with higher initial steepness of the sediment wave flanks assuming equivalent initial wave amplitudes, i.e. $A_0 = 0.25 m$. This results in higher tide-averaged flow velocities at the middle of the sand wave flanks which enhances bed shear stresses and therefore sediment transport, cf. Figures D.2a up to e. This also increases the tidally averaged suspended load transport which is known to have a dampening effect on sand wave growth (Borsje et al., 2014b). Nevertheless, bed load is the most dominant transport mode.

Chezy roughness

In contrast to the effect of the slope effect parameter, the effect of changes in Chezy roughness on the FGM results is less pronounced. The results show that lower Chezy roughness values are associated with higher initial growth rates and smaller preferred wavelengths (Figure C.1c). The first can easily be explained by the fact that a lower Chezy roughness value indicates a rougher seabed which induces

more turbulence and therefore more sediment transport. However, this conclusion does not hold for $C = 72.5$ and $75 m^{0.5} s^{-1}$, see Figure E.5. For these C values, particularly the latter, the model seems to become inaccurate which leads to small and large 'jumps' in tide-averaged bed load and suspended load transport, respectively. This considerably affects the total tide-averaged sediment transport. Therefore, the FGM results for these Chezy roughness values should be treated carefully. Additionally, stronger normalised circulation cells can be found for lower C values which is most likely due to the smaller preferred wavelength λ_{FGM} and therefore more steeper sediment waves flanks.

Grain size

The short-term calculations indicate that more rapidly growing sediment waves with smaller preferred wavelengths emerge for larger grain sizes (Figure C.1d). As the preferred wavelength gets smaller, less total sediment is needed for sediment waves to (initially) grow. The normalised tidally-averaged sediment transport plots support this statement as the total sediment transport equals the area under the curve, see Figure E.7. Additionally, smaller preferred wavelengths are accompanied with stronger, yet significantly smaller, circulation cells which induce more normalised tidally-averaged sediment transport (Figure 5.3). This results in larger normalised tidally-averaged bed load transport which enhances sediment wave growth. The differences in suspended load transport are minimal for $d_g \geq 3.00 mm$.

Similar to the Chezy roughness in the previous section, the model seems to be inaccurate for two parameter values, i.e. $d_g = 2.50$ and $2.75 mm$. As a result, both transport modes almost equally contribute to the total transport. This might be explained by the fact that the boundary between these transport modes is approached closely during the model runs. The effect of the strong increase in suspended load transport is also seen in the FGM plot and should be treated thoughtfully.

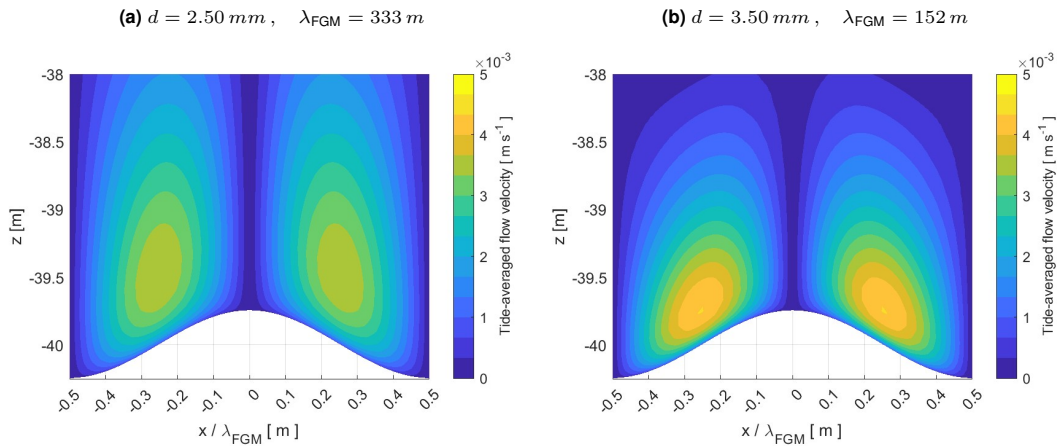


Figure 5.3: Normalised circulation cells for a varying median diameter d with its corresponding fastest growing mode λ_{FGM} .

Tidal velocity amplitude

To obtain a parameter range which ensured gravel wave growth with $\lambda_{FGM} > 100 m$ several test runs were initially performed. This resulted in a range from $1.60 m s^{-1} \leq U_{S2} \leq 1.95 m s^{-1}$. From the FGM plot in Figure C.1e it can be concluded that a lower tidal velocity amplitude leads to smaller preferred wavelengths with larger initial growth rates as less total sediment is needed to grow. In addition, the normalised circulation cells are smaller, yet slightly stronger due to the steeper flanks of the smaller wavelengths (Figure D.5). This explains the larger normalised bed load transport for $U_{S2} = 1.60 m s^{-1}$, see Figure E.9. Logically, higher tidal velocity amplitudes lead to larger normalised tidally-averaged suspended load transport. However, for $U = 1.95 m s^{-1}$ the curve of the normalised tidally-averaged suspended load transport consists of inaccuracies. This also leads to a significant increase in total sediment transport during one tidal cycle thereby most likely affecting the FGM results.

5.2.2. Finite-amplitude stage

Van Gerwen (2016) already showed that the sensitivity of various process parameter can be significant for the North Sea setting. However, the preferred wavelength was not calculated and applied for each individual run. In addition, the post-glacial Irish Sea setting is considerably different from the North Sea. Therefore, the sensitivity of the process parameters during the finite-amplitude stage of sediment wave development is revised in this section. Here, the wave height, the crest-trough and normalised bed level development over a specific equilibrium time-scale are compared for the different parameter settings, see Figure 5.4. The bed level development of individual runs from the process parameters can be found in Appendix F.

The sediment wave crest is characterised by the highest bed level in the centre of the area of interest, whereas the trough is considered as the lowest bed level succeeding this crest or the local maxima within this trough. The local maxima is selected since this is most likely the most realistic location within the trough where the threshold of motion for sediment transport is not reached. The wave height consists of the distance between the crest and succeeding trough.

The fastest growing mode which followed from the small-amplitude stage is used as initial wavelength λ_0 to shorten computation time. Also, a MORFAC value of $MF = 2000$ is used to further reduce calculations. A line is fitted between the time steps of approximately 2.74 years to obtain a curve that represents the wave height and crest-trough development over time. However, the effect of the MORFAC value should be taken into account, see Section 5.1.

Suspended load transport

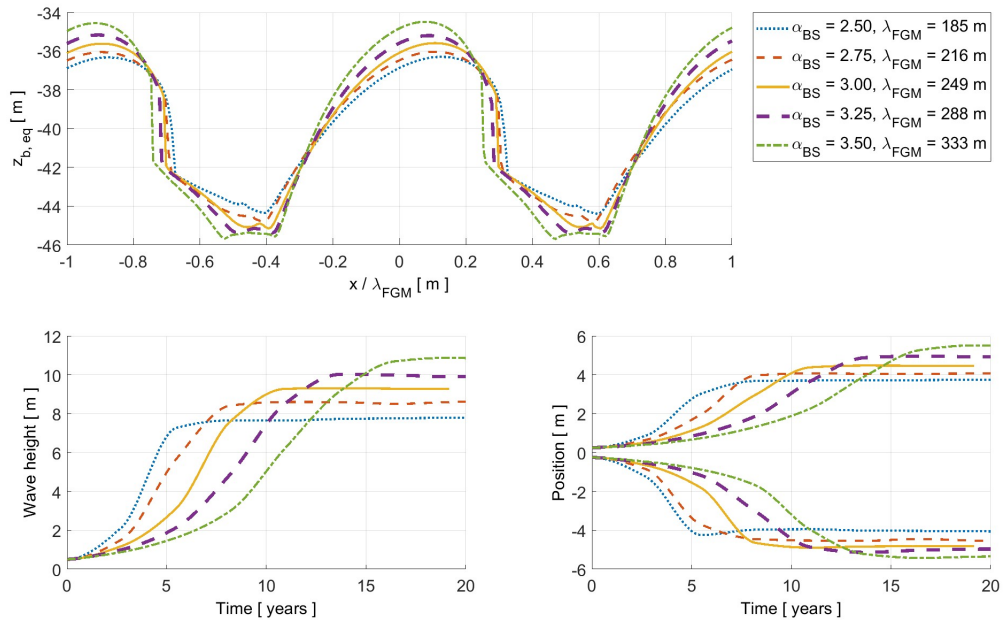
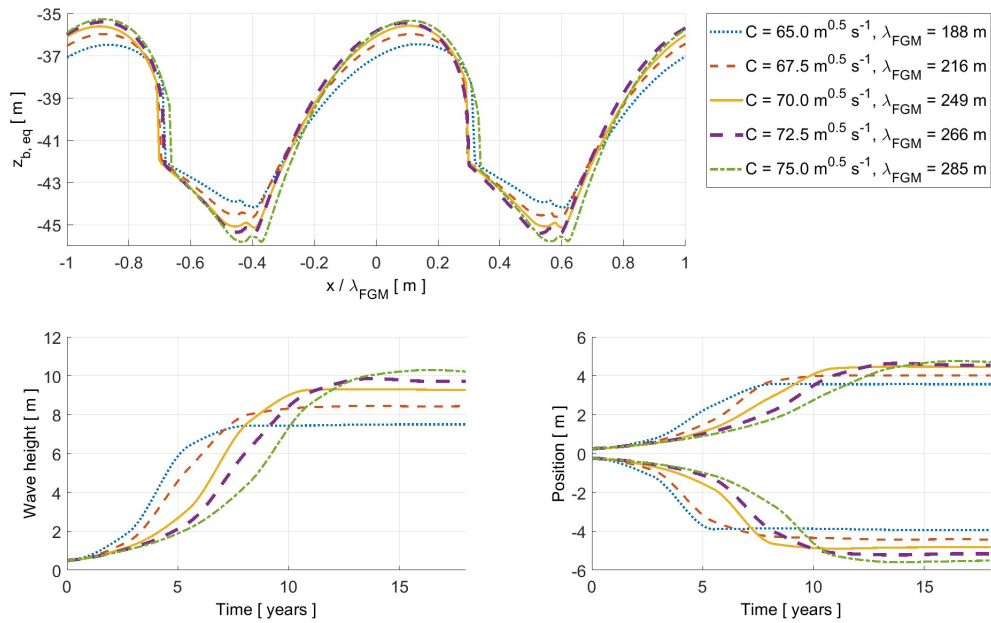
The bed level development over time with and without suspended load transport are shown in Figure F.2. The long-term effects of including suspended load transport indicate that the equilibrium time-scale is significantly shorter in comparison to excluding this transport mode, i.e. approximately 11 and 16.5 year, respectively. Besides, including suspended load transport results in a slightly lower equilibrium wave height. However, this might also be an effect of the smaller wavelength. Even though both equilibrium bed levels hardly differ, the sensitivity of various parameters on the small-amplitude stage point out the importance of this process as this might result in inaccuracies of the model results.

Slope effect parameter

It can be concluded that the equilibrium time-scale for sediment waves in the Irish Sea setting is strongly affected by changes of the slope effect parameter. Similar to the study of Van Gerwen (2016), lower α_{BS} values results in a shorter time-scale. For a higher α_{BS} value and thus longer preferred wavelength sediment waves tend to grow larger in equilibrium wave height. Moreover, the position of the equilibrium trough seems to converge towards a maximum depth as it flattens for larger slope effects. Here, the flow velocities are too weak to set the sediments in motion. In turn, the crest seems to grow in height which is most likely possible due to the longer wavelength. However, the slope effect parameter is not considered of paramount importance for this study since it is used as tuning parameter.

Chezy roughness

The larger initial exponential growth for lower Chezy roughness values $C = 65$ and $67.5 m^{0.5} s^{-1}$, and thereby smaller preferred wavelengths, is clearly visible in Figure 5.4b. More or less a similar (normalised) equilibrium shape of the sediment wave is generated for different Chezy roughness values. However, increasing the Chezy roughness value affects the sediment wave equilibrium height and time-scale significantly. Here, changes of the C value particularly affect the equilibrium trough of the sediment waves, i.e. a further deepening of the trough for larger parameter values. In contrast, the equilibrium crest seems to converge towards a maximum value or minimum water depth. The equilibrium time-scale ranges from approximately 8 to 16 years.

(a) α_{BS} (b) C 

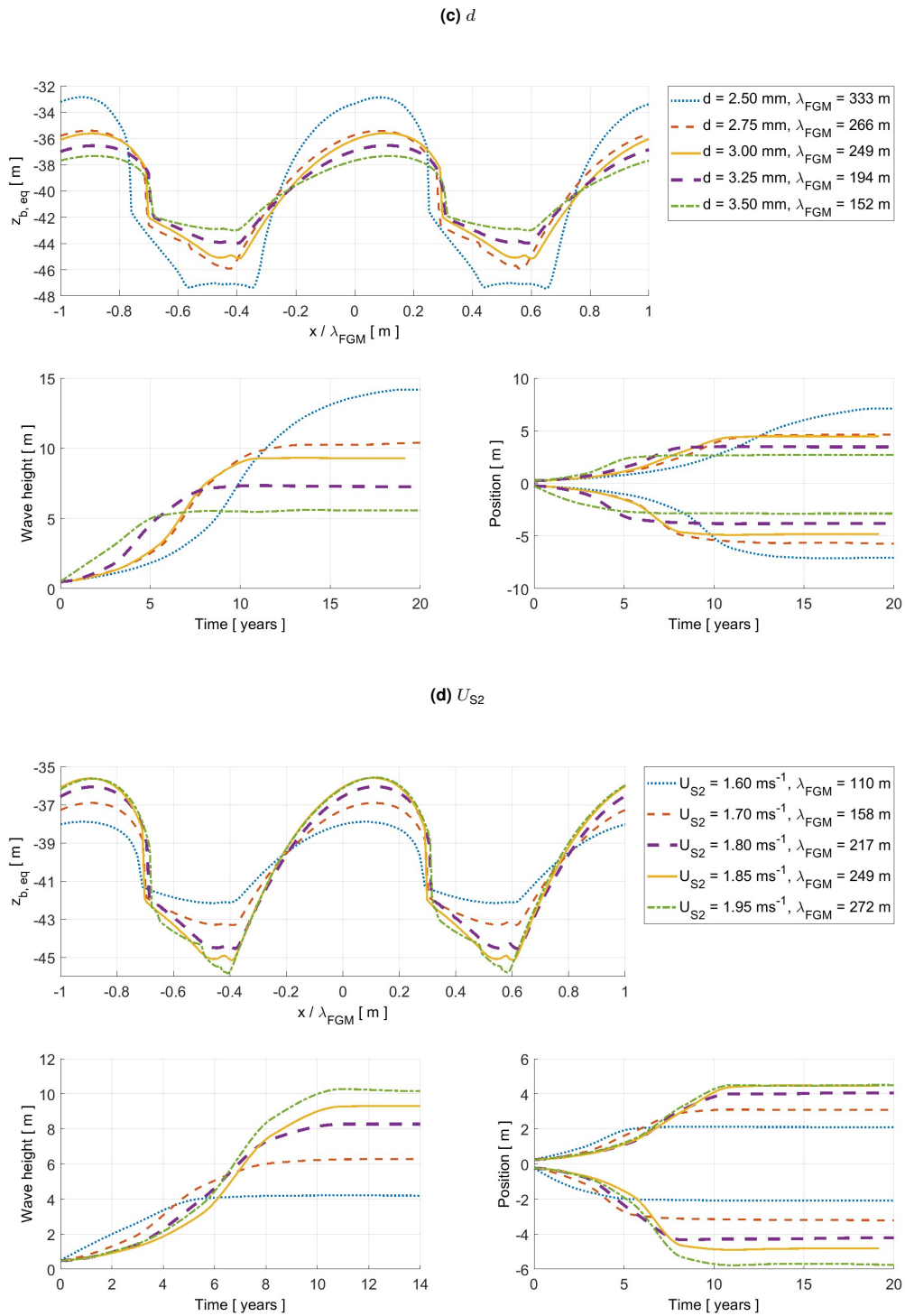


Figure 5.4: Normalised equilibrium bed level $z_{b,eq}$, wave height and crest-trough development for variable process parameters: a) slope effect tuning parameter α_{BS} , b) Chezy roughness coefficient C , c) uniform grain size diameter d and d) tidal velocity amplitude U_{S2} .

Grain size

Figure 5.4c shows the effect of changes in grain size diameter to the sediment wave height and its position of the crest and through over time. It can be concluded that the coarser sediment waves with their smaller λ_{FGM} initially grow faster in wave height which confirms the FGM result described in the previous section. However, their equilibrium wave height and time-scale differ both significantly, cf. $d_g = 2.50$ and $d_g = 3.50$ mm. It should be noted here that the relatively short equilibrium time-scale of the sediment waves for $d = 3.50$ mm with respect to the time step of circa 2.74 years ($MF = 2000$) conceals exponential growth of the fitted line. On the contrary, the differences in sediment wave development for $d_g = 2.75$ and $d = 3.00$ mm are minimal. This could be an effect of the earlier mentioned inaccuracies of the suspended load transport, see Figure E.7. Furthermore, the finest grain size $d_g = 2.50$ mm shows a considerable sediment wave height equilibrium with a deviating equilibrium seabed $z_{b,eq}$ with respect to the other parameter values. Here, the initial sinusoidal pattern is absent due to the relatively flat wide troughs which are also observed in previous modelling studies, e.g. Damveld et al. (2020b).

Tidal velocity amplitude

From Figure 5.4d it can be inferred that the differences in initial growth for different U_{S2} are less pronounced than for other process parameters, cf. α_{BS} and C . Again, exponential growth is hidden due to the selected MORFAC value, cf. $U_{S2} = 1.60$ ms^{-1} and $d = 3.50$ mm. The equilibrium normalised sediment wave shape $z_{b,eq}$ remains largely identical for changes in U_{S2} . However, the equilibrium wave height is noticeably sensitive to these changes, i.e. enhanced hydrodynamics result in greater heights in the order of metres. This effect nevertheless seems to weaken as the U_{S2} value increases which might be due to the intensified suspended load transport, see Figure E.9. The equilibrium crest develops on a longer time-scale compared to the trough. Similar to an increasing Chezy roughness value, the convergence towards a maximum crest height is observed. Furthermore, tidal velocity amplitudes values $U_{S2} \geq 2.00$ ms^{-1} resulted in instabilities of the model simulations.

5.3. Conclusions

The hydrodynamic time step of $\Delta t = 3$ s is most sufficient as model results seem independent of a smaller time step. The sediment wave evolution towards equilibrium is significantly affected by the selected MORFAC value. Due to time restrictions and the specified scope, however, the influence of the morphological acceleration factor is not further analysed in the remainder of this research as this is beyond the scope. A MORFAC value of $MF = 1,000$ is chosen for the following modelling phase based on computation time. Consequently, the morphological evolution is simulated for approximately each 1.37 years. A model simulation time of 20 years is adequate following the MORFAC value and the equilibrium time-scales.

Since the results in this chapter are focused on the parameters individually, the effect of changes to the process parameters on the fastest growing mode and the wave height are normalised in Figure 5.5. Both the Chezy roughness value and the tidal velocity amplitude affect the FGM similarly, whereas the sediment diameter has the complete opposite effect (longer preferred wavelengths for larger grains). Likewise, these effects are observed for equilibrium sediment wave heights. Larger Chezy roughness values and tidal velocity amplitudes generate sediment waves with greater equilibrium heights. In addition, changes in both process parameters are shown to affect the maximum bed shear stresses most significantly. These parameters can therefore be used to mimic the evolution of sediment waves due to sea level rise and enhanced hydrodynamics during the post-glacial period. The effect of the slope effect tuning parameter is less compared to the other process parameters and is therefore neglected in the remainder of this study.

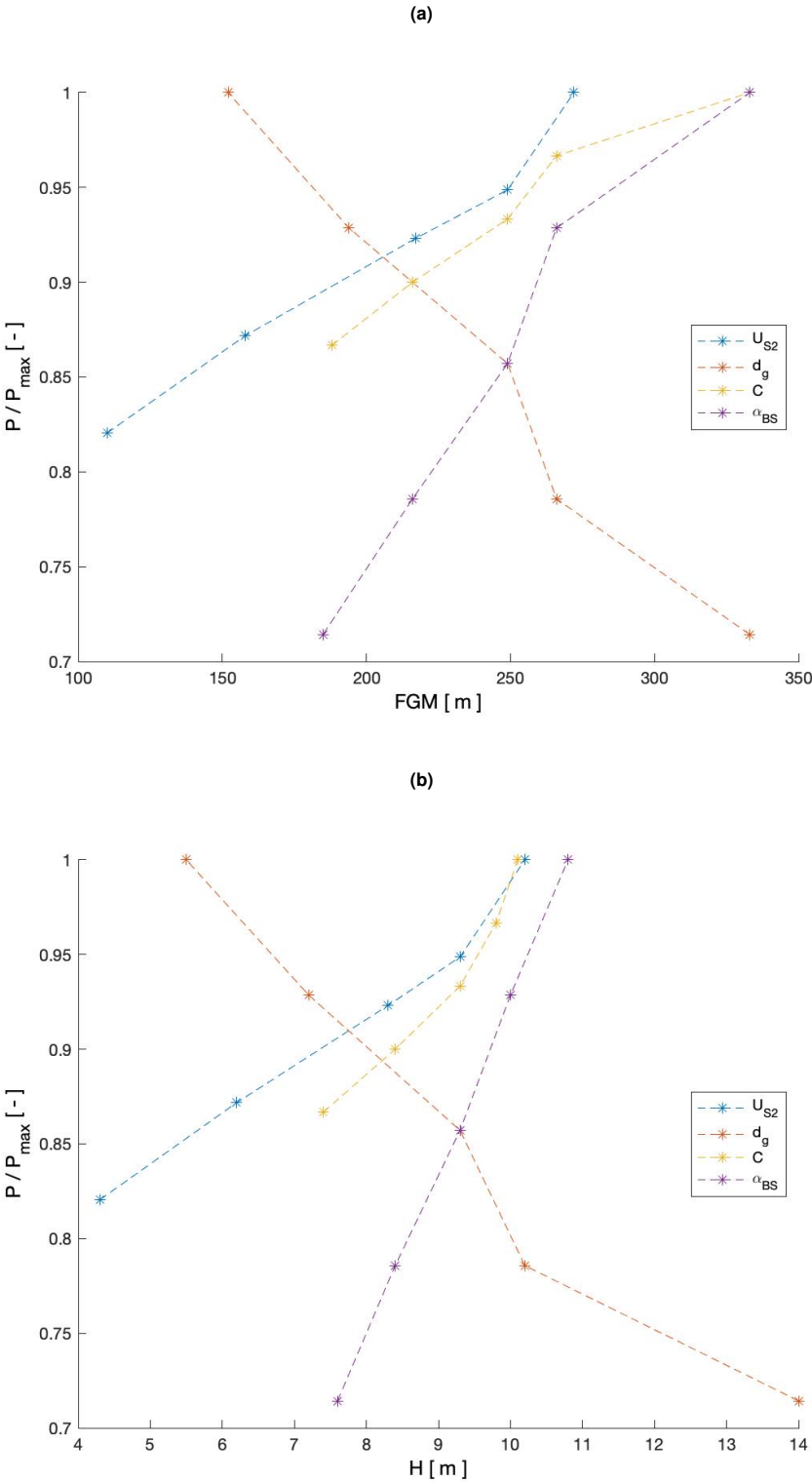


Figure 5.5: Normalised process parameter values P/P_{\max} against (a) fastest growing mode FGM and (b) equilibrium wave height H . Values follow from individual short- and long-term simulations, respectively. Parameter ranges can be found in Table 5.1.

6

Post-glacial modelling

This chapter describes the reconstruction of the formation and evolution of the coarse core of trochoidal sediment waves throughout the post-glacial period using an existing sand wave model. At the heart of this modelling phase is the palaeo-tidal reconstruction by Uehara et al. (2006): potentially the driving force behind the formation and evolution of some of the trochoidal sediment waves. This is done through a 2DV case study model which is discussed first. Subsequently, the model results are presented.

6.1. Model set-up

The vertical grid consists of 60 σ -layers with a high near-bed resolution and gradually decreasing towards the water surface. The amount of sigma layers are unchanged with respect to previous modelling studies. These studies considered a shallow sea with a constant reference water depth $H_0 = 25\text{ m}$. The distribution profile of the σ -layers is shown with the solid (purple) line in Figure 6.1. This study however focuses on sediment wave formation and evolution at larger variable reference water depths, i.e. $H_0 = 40\text{ m}$ (Case I), 60 m (Case II) and 80 m (Case III) which are each linked to a certain time period, see following sections. Therefore, the distribution profile is adjusted analogously to the study of Singh (2021) to avoid a decrease in (near-bed) resolution, only for an increasing water depth (Figure 6.1). This near-bed resolution is most important since sediment transport is concentrated in this area. The resolution of the first 20 σ -layers closest to the bed is unchanged in order to maintain the same near-bed resolution, e.g. the near-bed layer has a thickness of $z_{\sigma_1} = 0.0125\text{ m}$. Above these layers, a power function is used to gradually increase the vertical spacing between the σ -layers towards the water surface, i.e.

$$z_{\sigma_n} = -H_0 + a_{H_0} \cdot \sigma_n^{b_{H_0}}, \quad 21 \leq n \leq 60, \quad (6.1)$$

$$a_{H_0} \approx \begin{cases} 2.17 \cdot 10^{-3}, \\ 7.18 \cdot 10^{-4}, \\ 3.28 \cdot 10^{-4}, \end{cases} \quad b_{H_0} \approx \begin{cases} 2.40, & H_0 = 40\text{ m}, \\ 2.77, & H_0 = 60\text{ m}, \\ 3.03, & H_0 = 80\text{ m}, \end{cases} \quad (6.2)$$

where z_{σ_n} is the z -coordinate of the corresponding σ -layer number n with $z_{\sigma_{60}} = 0\text{ m}$, a_{H_0} and b_{H_0} are constants at reference depth H_0 . Note that this is the case for a flat bed. Its computed resolution however is applied in the entire domain.

Table 6.1 shows an overview of values and dimensions of the model and process parameters for the three earlier mentioned cases. A description of the basic model set-up in Delft3D can be found in Chapter 3. Below, the model set-up of each case is substantiated.

6.1.1. Case I: 12-11 ka BP, 40 m deep, low bed stresses

An (almost) flat seabed is assumed at the start of the simulation, see Figure 5.2. This bathymetry is linked to the time period of 11 to 12 ka years ago. During this period the modelled peak bed shear stresses at the various survey areas in the Irish Sea started to increase significantly, see Figure 4.3b.

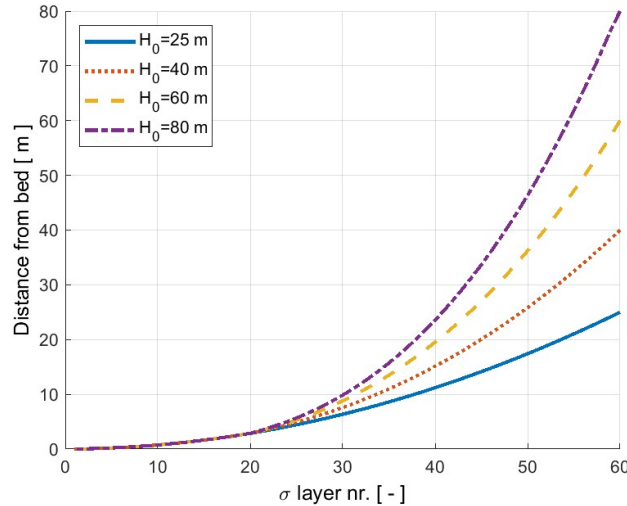


Figure 6.1: The distribution of the σ -layers over the water column, showing the distance from the bottom per layer for a reference water depth of 25 m, 40 m, 60 m, 80 m.

Additionally, the initial depth $H_0 = 40$ m is based on the average of the palaeo-tidal reconstruction of the water depths throughout this time. The number of grid cells in the finer part of the domain, i.e. area of interest, follow from the preferred wavelengths with respect to the process parameter sensitivity, see Section 5.2.

The values of the various process parameters α_{BS} , C , d_g and U_{S2} are selected for Case I based on different arguments. The slope effect parameter is considered as a tuning parameter and its value $\alpha_{BS} = 3.0$ is therefore unchanged with respect to previous modelling studies. The grain sizes of the seabed sediments are regarded uniform as a unimodal grain size distribution adds more (avoidable) complexity and computation time (Damveld et al., 2020b). The grain size diameter $d_g = 3.00$ mm follows from data analysis of the grab samples during the AmSedIS project, see Section 4.2.2. This diameter size roughly corresponds to the gravel collected along the trochoidal sediment waves at the survey areas, whereas lower grain sizes might result in inaccuracies (cf. Figure E.7). The bed is assumed uniformly mixed to simplify the analysis. Subsequently, the Chezy roughness value for a flat topography is calculated with Equations 3.7 up to 3.9 and equals approximately $C = 70$ $m^{0.5}s^{-1}$. The tidal velocity amplitude is set to $U_{S2} = 1.85$ $m.s^{-1}$ to enhance long-term sediment wave growth. Larger amplitudes might cause inaccuracies in suspended load transport or instabilities and are therefore avoided, see Section 5.2.

6.1.2. Case II: 10-9 ka BP, 60 m deep, steep rise in bed stress

Instead of simulating once again from a flat seabed, the equilibrium bed level of Case I is used as initial topography for Case II as the water depth is increased to simulate the reconstructed rise in sea level (Figure 4.3a). Here, the reference water depth $H_0 = 60$ m is adopted since this depth matches reasonably with the average depth at the survey areas around the time period of 9 to 10 ka BP. Thus, twenty metres are subtracted from the equilibrium bed level of Case I to obtain this depth increment and to thereby take a leap in time. Despite the rising water in the Irish Sea during this period, the palaeo-tidal reconstruction of the peak bed shear stresses shows a similar trend, cf. Figure 4.3b. Therefore, it is expected that the sediment waves grew along with a rising water depth. Consequently, it is assumed that the sediment waves are bedforms from an earlier time period.

Short-term calculations with $MF = 1$ are initially executed to determine the effect of the depth increment on the maximum bed shear stresses $\tau_{b,max}$ during one tidal cycle. First, the peak bed shear stresses at equilibrium for Case I are calculated. Subsequently, the depth increment is applied and the small-amplitude stage is again analysed. Note that the numerical model and process parameters other than the water depth and MORFAC value are unchanged. Afterwards, the influence on the maximum bed shear stresses for changes to the Chezy roughness value and tidal velocity amplitude

Table 6.1: Overview of values and dimensions of model and process parameters for three different cases. Each case represents a time period during the post-glacial history of the Irish Sea. Note that the equilibrium bed level of Case I is used as initial topography for Case II. The initial amplitude for Case III is defined by a random function.

Description	Symbol	Value	Dimension
Number of σ layers	-	60	-
Hydrodynamic time step	Δt	3	s
Grid spacing (finer part)	Δx	2	m
Morphological acceleration factor	MF	1,000	-
Uniform grain size diameter (gravel)	d_g	3.0	mm
Slope effect parameter	α_{BS}	3.0	-
Residual current strength	U_{S0}	0	ms^{-1}

Case	I	II	III		
Reference water depth	H_0	40	60	80	m
Number of grid cells (finer part)	-	1,000	1,000	2,500	-
Morphological duration	-	20	10	80	$years$
Chezy roughness	C	70	67.5	65	$m^{0.5}s^{-1}$
Tidal velocity amplitude	U_{S2}	1.85	2.00	2.15	ms^{-1}
Initial wave amplitude	A_0	0.25	-	0 – 0.25	m
Initial wave wavelength	λ_0	250	250	-	m

are determined since these two process parameters affect bed shear stresses along the sediment wave most significantly, see Section 5.3.

Accordingly, these parameter values are adjusted to replicate the trend that follows from the GIA-models, i.e. enhanced maximum bed shear stresses in comparison to the previous time period. Besides, the Chezy roughness value changes due to the increasing water depth and the established topography from Case I which both have adverse effects on its value. An increment of the water depth results theoretically in a higher Chezy roughness value with Eqs. 3.7-3.9 and the aforementioned parameter values. However, the significant presence of the sediment waves with wave height $H = 10.5 m$ and wavelength $\lambda = 250 m$ causes flow alterations.

In addition, a continuing growth of the sediment wave with the depth increment is stimulated, i.e. by lowering the Chezy value and increasing the tidal velocity amplitude. Thereby, the strong increment of the reconstructed peak bed shear stresses is reproduced. The new setting for Case II is associated with a positive growth rate for the wavelength of circa $\lambda = 250 m$, i.e. the initial wavelength and the fastest growing mode for Case I. It is avoided that the bed returns to a stable state (flat bed) which occurs for negative growth rates corresponding to this particular wavelength.

At last, the initial topography is run for multiple years with the altered Chezy roughness value, tidal velocity amplitude and water depth towards a new equilibrium. Here, the number of grid points in the centre of the domain is unchanged due to the non-evolving wavelength. The bed level changes are simulated with a morphological duration of 10 years since the system reaches equilibrium within this time period.

6.1.3. Case III: 7-6 ka BP, 80 m deep, stabilising bed stresses

For the previous case, it is assumed that the sediment waves are bed features from the preceding water depth and thus time period. Likewise, the equilibrium bed level of Case II is initially adopted as topography for Case III. A reference water depth of $H_0 = 80 m$ is selected which corresponds to

the period 6 to 7 ka BP. During this period the palaeo-tidal reconstruction shows that hydrodynamics stabilised towards the current Irish Sea setting, see Figure 4.3.

The process parameters C and U_{S2} are altered with the knowledge obtained from the previous case about the influence of the Chezy roughness value and the tidal velocity amplitude on the maximum bed shear stresses $\tau_{b,max}$. Lowering the first and increasing the latter parameter results in larger maximum bed shear stresses thereby mimicking the palaeo-tidal reconstruction. Here, the parameter values $C = 65 m^{0.5} s^{-1}$ and $U_{S2} = 2.15 m s^{-1}$ are selected. However, the growth rate corresponding to a wavelength of $\lambda = 250 m$ ($k = 0.025 m^{-1}$) is negative for this parameter settings at $H_0 = 80 m$ as can be observed from the FGM results, see Figure 6.2. This resulted in a dampening towards a flat bed of the initial topography which is adopted from Case II.

A random bed level is therefore introduced to simulate the sediment wave development more realistically. This randomness is applied through the initial wave amplitude by a random function, i.e. at each x-point inside the finer part of the domain the initial bed level is randomly assigned to a value $z_{b,0} = H_0 + A_0$ with $H_0 = 80 m$ and $0 < A_0 < 0.25 m$. Random bed perturbations are thereby created with varying wavelengths. Here, the number of x-points is increased to 2,500 as the FGM is significantly larger with respect to the previous cases. Damveld et al. (2020a) used a random distribution of vegetation patches along sand waves to analyse the sand wave development over time for a significant number of simulations. This study showed a convergence of the wavelength distribution towards the (abiotic) FGM over time. In addition, a spread of the crest and trough development was observed by Damveld et al. (2020a). The model simulations of Case III are therefore run several times with different random bed levels for approximately 80 years to demonstrate this convergence and spread. The simulation time requires circa 4.5 days on an external computing device. Due to time limitations the number of simulations is therefore maintained at three.

6.2. Results

This section describes the results of the above mentioned cases. The cases each represent a time period during the post-glacial history of the Irish Sea by means of depth increment and enhanced hydrodynamics.

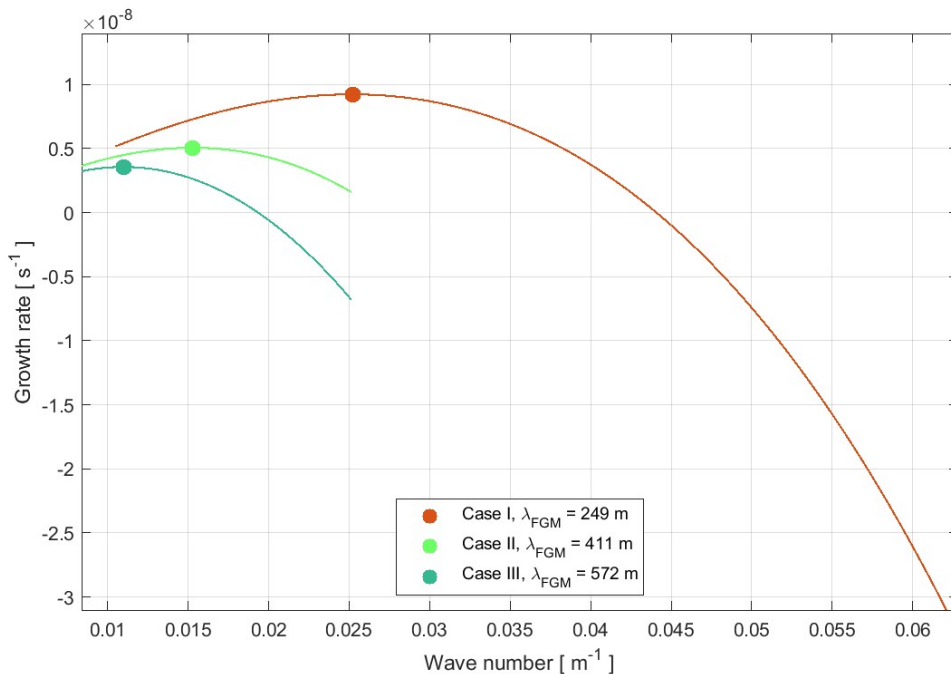


Figure 6.2: Growth rate γ [s^{-1}] against wave number k ($= 2\pi/\lambda$) [m^{-1}] for three cases as described in Section 6.1. The circles indicate the growth rates corresponding to the fastest growing mode λ_{FGM} . The x-axis corresponds to $\lambda = [750, 100] m$. Note that a line is fitted between growth rates that are associated with $\lambda = 100, 250, 400, 600, 750 m$.

6.2.1. Case I: 12-11 ka BP, 40 m deep, low bed stresses

The first case represents the time period 11 to 12 ka BP at which modelled peak bed stresses in the Irish Sea were at their lowest. The fastest growing mode associated with this setting is calculated beforehand and is used as initial wavelength $\lambda_0 = 250 \text{ m}$, see Figure 6.2. Here, a wide range of wavelengths are associated with a positive growth rate.

Figure 6.3 shows the development of the bed level, wave height and the crest and trough towards the finite-amplitude stage. During the simulations the (initial) wavelength remains fixed. It can be seen that the sediment waves grows asymmetrically during the period of fastest growth. This results in a relatively steep right-side slope and is linked to the relatively high MORFAC value, see Section 5.1. However, the reduced computation time is considered more beneficial for this study. The equilibrium wave height of the sediment waves reaches approximately $H = 10.5 \text{ m}$ after a morphological duration of 12 years. Nonetheless, the crest and trough behave differently during this time-scale, i.e. the trough develops more quickly towards its equilibrium position.

6.2.2. Case II: 10-9 ka BP, 60 m deep, steep rise in bed stress

The equilibrium bed level from the previous case is adopted and the water depth is increased with to make a jump in time towards 9 to 10 ka BP and to mimic the corresponding sea level rise. The influence of the two process parameters, the Chezy roughness and the tidal velocity amplitude, is first analysed. The maximum induced bed shear stress, the FGM and the sign of the growth rate for $\lambda = 250 \text{ m}$ are shown in Table 6.2. The last is included to avoid that the bed returns to a stable state thereby stimulating further growth of the sediment wave of Case I. The FGM plots can be found in Figure C.2.

It can be concluded that the tidal velocity amplitude affects the maximum bed shear stresses most in comparison to the Chezy roughness value. This is in line with model results from the sensitivity analysis (cf. Figure E.6 and E.10). These figures also show maximum bed shear stresses of $\tau_{b,\max} = 6.25 \text{ Nm}^{-2}$ near the crest for Case I at $t = 0$. At equilibrium, maximum bed shear stresses of $\tau_{b,\max} = 9.53 \text{ Nm}^{-2}$ are generated for Case I. Therefore, the setting for $U_{S2} = 1.85 \text{ ms}^{-1}$ and $C = 72.5 \text{ m}^{0.5} \text{ s}^{-1}$ is insufficient. Additionally, $U_{S2} = 2.00 \text{ ms}^{-1}$ and $C \geq 70 \text{ m}^{0.5} \text{ s}^{-1}$ show negative growth rates. The setting for $U_{S2} = 2.00 \text{ ms}^{-1}$ and $C = 67.5 \text{ m}^{0.5} \text{ s}^{-1}$ is eventually selected as it seems to follow the trend. Here, an enhanced tidal velocity amplitude shows no inaccuracies for suspended load transport (not shown here)

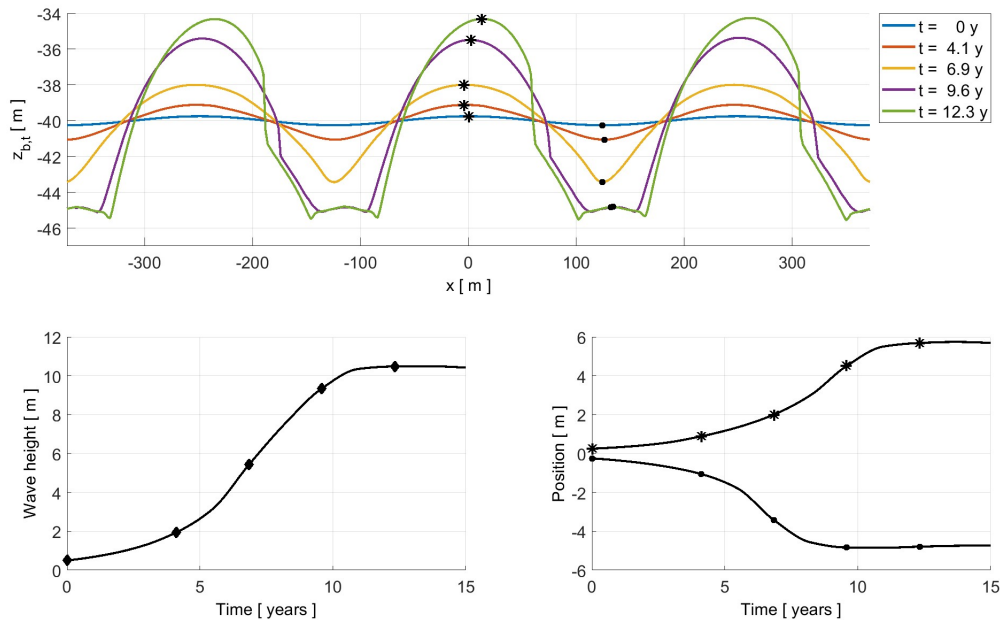


Figure 6.3: Bed level (top), wave height (bottom left) and crest-trough development (bottom right) over time for Case I. The markers indicate the moment in time t in years for the crest and trough.

in contrast to simulations for a smaller water depth ($H_0 = 40 \text{ m}$), see Section 5.2.

Subsequently, the long-term behaviour of the sediment waves is analysed. The bed level, wave height and crest-trough position over time are displayed in Figure 6.4. The results indicate that the sediment waves grows circa $\Delta H = 3.5 \text{ m}$ in height which is mostly due to the deepening of the trough. The right sediment wave flank slightly widens due to sediment deposition. However, the main shape of the sediment waves is preserved.

Table 6.2: Maximum bed shear stress $\tau_{b,\max}$ [Nm^{-2}], the FGM [m] and the growth rate [\pm], denoting positive/negative] for $\lambda = 250 \text{ m}$ for different combinations of Chezy roughness value C and tidal velocity amplitude U_{S2} during the small-amplitude stage of Case II.

$(\tau_{b,\max}, \lambda_{FGM}, \gamma)$		$C [m^{0.5}s^{-1}]$								
		67.5		70.0		72.5				
$U_{S2} [ms^{-1}]$	1.85	10.63	303	+	10.03	340	+	9.46	380	+
	2.00	12.32	411	+	11.63	451	-	10.97	499	-

6.2.3. Case III: 7-6 ka BP, 80 m deep, stabilising bed stresses

A random signal is chosen as initial condition which contains a variety of (unknown) wavelengths. The initial random bed level for one of the three individual runs is shown in Figure 6.5. From the bed level development over time, it can be concluded that the sediment waves inside the area of interest take significantly longer to form and to evolve compared to the fixed cases, cf. Case I and Case II. Eventually, the wavelengths which are included in the random signal and are associated with the largest growth rates prevail.

Nevertheless, due to the deviating sediment waves their characteristics require a new definition. Here, the sediment wave height is defined as the distance between the crest and the deepest adjacent trough, while the wavelength is represented by the average distance between the largest and its two

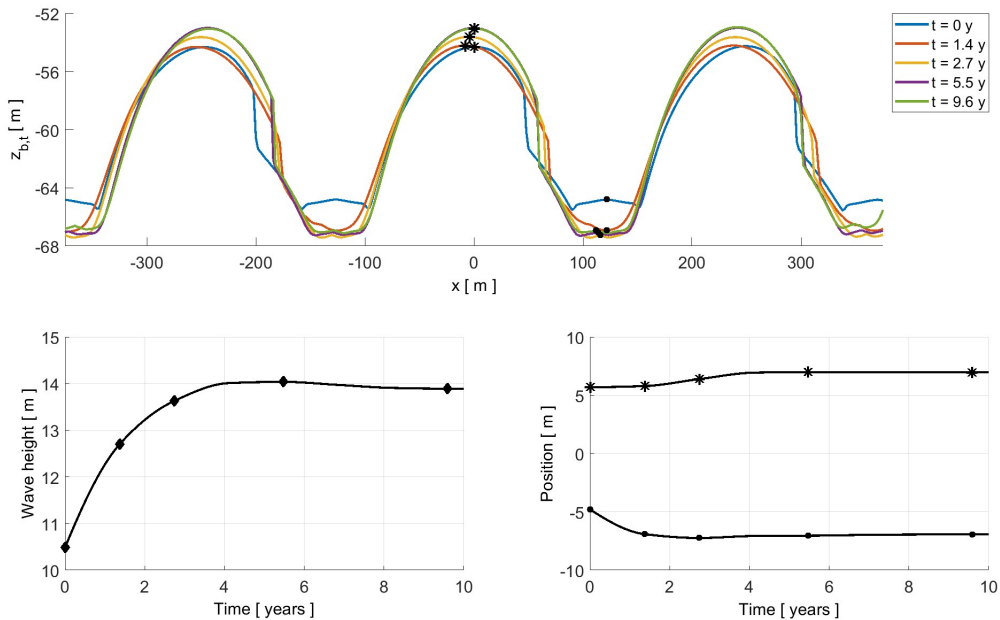


Figure 6.4: Bed level (top), wave height (bottom left) and crest-trough development (bottom right) over time for Case II. The markers indicate the moment in time t in years for the crest and trough. Note that the initial topography is adopted from Case I with a depth increment of twenty metres which represents a jump in time of several thousands of years.

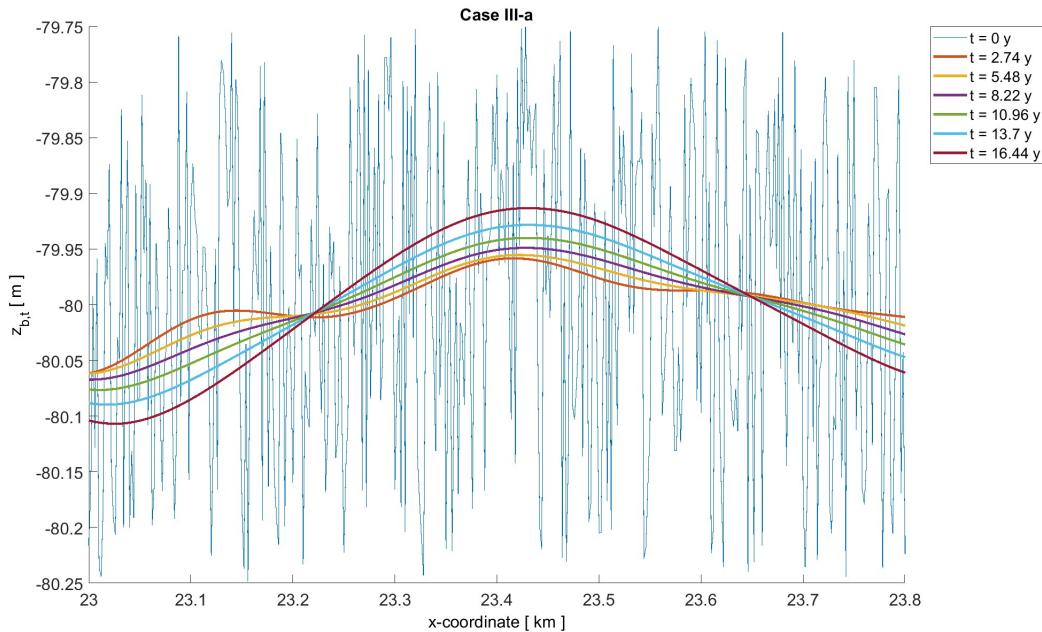
Table 6.3: Sediment wave height and wavelength in metres at approximately 80 simulation years for different runs of Case III with an initially random topography, see Figure 6.6.

Run	Wavelength λ [m]	Wave height H [m]
Case III-a	615	33.4
Case III-b	520	32.1
Case III-c	486	29.6

neighbouring crests. Note that only the largest and fastest growing sediment wave is taken into account. Table 6.3 shows the characteristics of the most dominant sediment wave for the three different model runs. After approximately 80 years the wave height equals roughly $H = 30\text{ m}$. The trough seems to reach its maximum depth at circa 95 m at which the critical bed shear stress is not being exceeded. On the other hand, the crest grows towards $z_b = 60\text{ m}$ depending on the wavelength, i.e. longer sediment waves tend to grow larger in height. The wavelength ranges from $\lambda = 486$ up to 615 m which corresponds relatively well with the fastest growing mode $\lambda_{\text{FGM}} = 572\text{ m}$. This clearly indicates the spread in both wave characteristics. In addition, the bed level development over time shows a convergence towards wavelengths close to the fastest growing mode.

6.3. Conclusions

Through a 2DV case study the model is able to reconstruct the formation and evolution of the coarse core of sediment waves. Here, three cases are each linked to time periods following the trend of significant sea level rise and enhanced hydrodynamics on a millennial scale which characterises the Irish Sea during the post-glacial history. However, this case study also shows that only larger initial wavelengths prevail at larger depths of 80 m. By using a random (almost flat) bed level sediment wave heights and wavelengths are nevertheless simulated which are comparable to those observed during the AmSedIS project.

**Figure 6.5:** Initial bed level development over time for Case III-a. Note that a random function is used as initial topography where $z_{b,0} = H_0 + A_0$ with $H_0 = 80\text{ m}$ and $0 < A_0 < 0.25\text{ m}$.

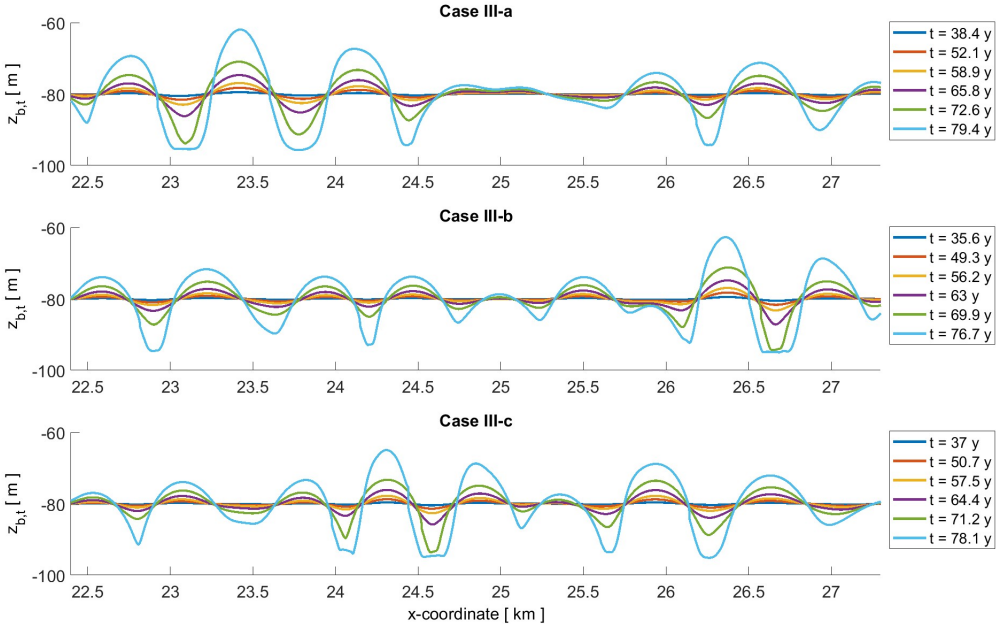


Figure 6.6: Long term bed level development over time for Case III. A random function for three different runs *a*, *b* and *c* is used as initial topography, see Figure 6.5. Note that the sediment waves are not in equilibrium.

7

Present-day modelling

The results of the previous chapter demonstrate that the Delft3D model is able to simulate the formation and evolution of the coarse core of sediment waves over a significant time period in which hydrodynamics enhanced considerably. In this chapter the model is used to analyse the initial effect of a sand veneer. These results will give a first indication of the sorting pattern along the sediment waves using a bimodal sediment mixture of the bed. First, the set-up of the model is discussed. This set-up is partly based on the results from the previous chapter. Subsequently, the results of the model are shown.

7.1. Model set-up

With the continued melting and retreating of the British-Irish Ice Sheet finer sediments are transported by rivers from the surrounding lands into the Irish Sea. In addition, glacial incisions which overlap with trochoidal sediment wave fields and are filled with fine sediments produce a continuous mobile sediment supply. This turns out to be crucial for further growth of the trochoidal sediment waves as is stated by Van Landeghem et al. (2013). Besides, these finer sediments are contemporary observed as a mobile (sand) veneer along the coarse core of the trochoidal sediment waves (Van Landeghem et al., 2009a).

This chapter considers a layered bed stratigraphy which describes multiple sediment layers. A more detailed description of the bed stratification in the Delft3D model can be found in Section 3.5. The equilibrium bed level $z_{b,eq}$ from Case II is chosen as initial topography, see Figure 6.4. Then, a sand layer is added to the system on top of the sediment waves, i.e. $z_b = z_{b,eq} + L_s$. The gravel and sand in the system can be considered as bimodal. The thickness of the sand layer is assumed thin to prevent significant changes in hydrodynamics and initially set to $L_s = 0.3 m$. Subsequently, the thickness of the active transport layer and underlayers are selected such that the sand layer L_s is completely separated from the original gravel, that is, $L_a = 0.2 m$ and $L_{u,max} = 0.1 m$, respectively. The latter represents the initial and maximum thickness of the underlayers, whereas the first remains this identical value throughout the entire simulation. The sand layer is also included outside the area of interest to simulate a more or less unlimited sand supply.

A total number of underlayers $N = 6$ are implemented in the model. This number is limited due to computation time. Accordingly, the initial uppermost underlayer $L_u^{(1)}$ consists of uniform sand, whereas the underlying layers $2 \leq n \leq 6$ contain uniformly distributed gravel with $d_g = 3.0 mm$. For convenience, the thickness of the base layer is set to $L_b = 5 m$ to avoid the unerodible bedrock layer which exists in the model below this base layer. This results in a total (initial) layer thickness of $L_{tot} = 5.8 m$. Both the sand $L_s = 0.3 m$ and gravel layer $L_g = 5.5 m$ are considered to be uniformly distributed to reduce complexity.

The morphodynamics are subsequently simulated for a morphological duration of *250 days*. Here, a MORFAC value of $MF = 100$ is used which follows from a (limited) sensitivity analysis, see Appendix G. Despite the fact that using $MF > 1$ and analysing tidal cycles is not physically correct, the aim of this chapter is to qualitatively determine the spatial and time dependency of the sorting pattern. Here, the Chezy roughness value is unchanged in spite of its relationship with the grain size, i.e. smaller grain size diameter results in a larger Chezy roughness value. An overview of this setting is shown in Table 7.1 and is based on Case II from the previous chapter.

Table 7.1: Overview of values and dimensions of the numerical model and process parameters. Note that the equilibrium bed level from Case II of the previous chapter is used as initial topography.

Description	Symbol	Value	Dimension
Number of σ layers	-	60	-
Hydrodynamic time step	Δt	3	s
Grid spacing (finer part)	Δx	2	m
Number of grid cells (finer part)	-	1,000	-
Morphodynamic duration	t	250	d
Morphological acceleration factor	MF	100	-
Active layer thickness	L_a	0.2	m
Maximum underlayer thickness	$L_{u,max}$	0.1	m
Initial number of underlayers	N	6	-
Initial base layer thickness	L_b	5	m
Initial sand layer thickness	L_s	0.3	m
Initial gravel layer thickness	L_g	5.5	m
Total (initial) layer thickness	L_{tot}	5.8	m
Reference water depth	H_0	60	m
Slope effect parameter	α_{BS}	3.0	-
Chezy roughness	C	67.5	$m^{0.5}s^{-1}$
Uniform grain size diameter (gravel)	d_g	3.0	mm
Uniform grain size diameter (sand)	d_s	0.30	mm
Tidal velocity amplitude	U_{S2}	2.00	ms^{-1}
Residual current strength	U_{S0}	0	ms^{-1}

7.2. Results

The results of the model simulations with the inclusion of a sand layer are described in this section. Thereby, the aim is to analyse its short-term influence on the sediment wave characteristics and the sorting patterns in the upper layer.

From Figure 7.1 it can be concluded that the system moves towards a new equilibrium due to the addition of the sand layer. This figure shows the sand fraction in the active layer and the bed level for different time frames. The time frames show that the sand fraction in the top layer remains relatively constant at these moments in time. The bed level however changes significantly. The crest position remains relatively stable, whereas the troughs are filled thereby decreasing the sediment wave height from circa 14 to 12 m. The large volume of sand that is deposited at the troughs originates mainly from outside the centre of the domain (not shown here). Additionally, the sediment waves regain their initial sinusoidal shape.

To investigate what occurs in between these time frames the sand fraction in the upper layer at the crest and its right-side flank and trough are plotted over time in Figure 7.2. Due to deposition and erosion processes the sediment fraction and thickness of the base layer and underlayers fluctuates continuously throughout the entire simulation. It can be seen that in the beginning the sand fraction at the crest decreases significantly. This fraction in the transport layer reaches an equilibrium relatively quickly ($t = 12.5d$), i.e. small amounts of sands are eroded during the largest flow velocities and deposited at slack water.

The right-side flank of the sediment wave is initially protected from the flow. As the tide turns ($U_1 < 0$), a vast amount of sand is eroded. During the subsequent slack water and tide changing direction, the flanks are replenished with sand again. Even though the flank is positioned at the stoss-side of the sediment wave for $U_1 > 0$, the largest flow velocities result in erosion of the sand, cf. $t = 50 d$. This equilibrium pattern is reached after approximately half a tidal cycle.

On the other hand, the equilibrium time-scale of the sand fraction at the trough is somewhat longer, i.e. two tidal cycles ($t = 100 d$). At first, sand is removed from the troughs and is slowly supplemented again. At equilibrium, the troughs are first eroded by the largest flow velocities directed rightward. Subsequently, sand is deposited during slack water and is shortly eroded again when flow velocities change direction and increase. However, the sand fraction increases significantly to an (almost) uniform layer during the largest flow velocities directed leftward. This is most likely due to transport from sands at the crest and flanks to trough. Additionally, a decrease in sand fraction during and just after slack water can be observed for the troughs, e.g. at $t = 138 d$. This can be explained by (suspended) gravel that is deposited thereby decreasing the sand fraction in the top layer.

7.3. Conclusions

The addition of a thin sand layer at the bed to equilibrium stage sediment waves affects the bed level significantly as the sediment waves act as a sand trap, i.e. the troughs are filled with sand whereas the crest is eroded and remains relatively coarse. This contradicts with the data as the coarsest sediments are found in the troughs. The troughs are supplied with sand during slack water and due to transport from the crest and flanks. This results in a decrease of the sediment wave height of circa 2 metres tending towards a new equilibrium after approximately 250 days. The sorting pattern along the sediment waves is time-dependent as the sand follows the flow direction of the tide which can be translated to the observed mobile sand veneer.

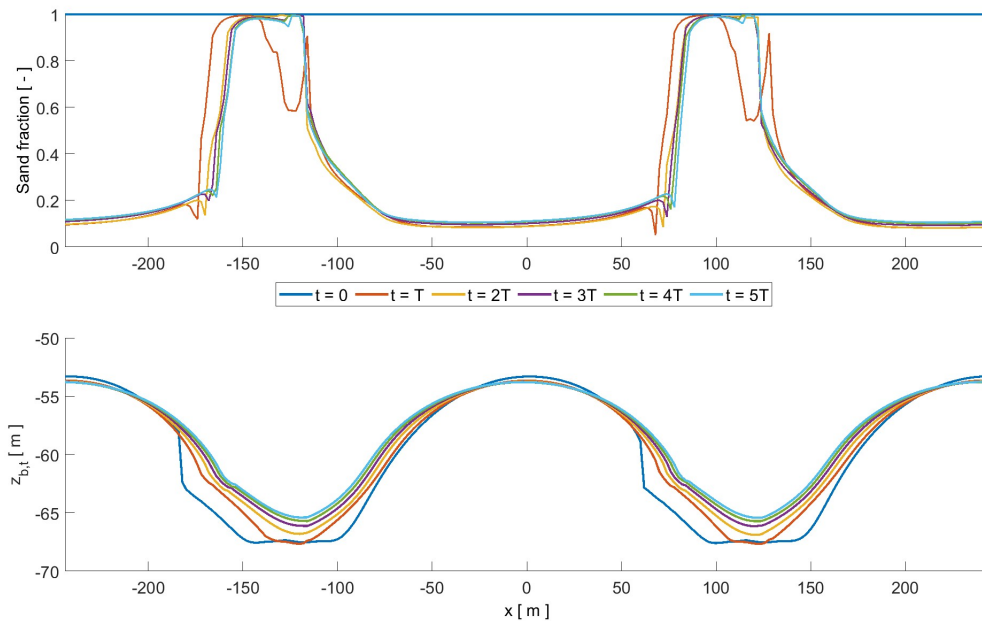


Figure 7.1: Sand fraction in the active transport layer (top) and bed level development $z_{b,t}$ (bottom) along the x-axis for time frames of t where $T = 50 d$. The used parameter values can be found in Table 7.1.

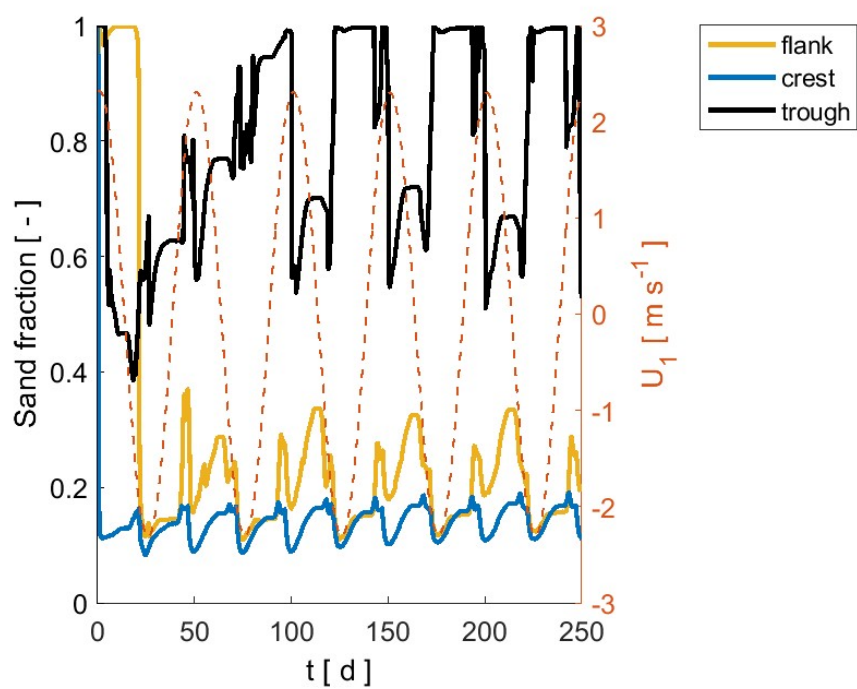


Figure 7.2: Sand fraction in the active transport layer at the crest, (right-side) flank and trough over time t in days. The horizontal velocity U_1 is plotted at the right axis. Note that the flow is directed rightward for $U_1 > 0$ and to the left for $U_1 < 0$. One tidal cycle lasts 50 days as morphodynamics are accelerated with a MORFAC value of $MF = 100$.

8

Discussion

In this chapter the obtained results are interpreted and some of the main limitations of the research are discussed. Naturally, the strengths of this research are highlighted as well.

Supporting the geological hypothesis

Through a 2DV case study the geological hypothesis by Van Landeghem et al. (2009a) is supported which states that the observed coarse core of trochoidal sediment waves in the Irish Sea are relicts from a distant past and are formed and evolved after the marine transgression as present-day hydrodynamics are not capable of generating these enigmatic bed forms. The retreat of the ice after the Last Glacial Maximum resulted between 12 and 6 ka BP in significant sea-level rise and enhanced peak bed shear stresses which is shown in the reconstruction of the palaeo-tidal conditions of the Irish Sea by the GIA model output (Uehara et al., 2006). Using increments of the water depth and enhancing the bottom roughness and tidal velocity amplitude these tidal conditions are simulated on a millennial timescale.

2DV case study model

The method to use a 2DV case study is significantly different from previous sand wave modelling studies which in general assume small-amplitude sand waves and a fixed water depth (e.g. Borsje et al., 2014b; Damveld et al., 2020b). The case study model sheds new light on the modelling of sediment waves since the model results show sediment wave growth with sea-level rise over a millennial time-scale. The depth increments of twenty metres seem relatively large, whereas it would be more optimal to let the water depth increase throughout the model simulation. Nevertheless, it is expected that this does not influence the qualitative results. Due to the substantial timescale and changing tidal conditions this method is believed to more realistically model the trochoidal sediment wave evolution over a significant period of time.

Furthermore, the Irish Sea is not the only shallow sea that has been affected by the glacial periods. For the continental shelf of the Gulf of Valencia Albarracín et al. (2014) discusses the potential formation and evolution of sand waves between 12 and 10 ka BP due to storm waves and longshore littoral drift in contrast to a tidal origin. These sand waves are nowadays found at much larger water depths and are therefore also considered relicts. This method might therefore also be useful for sediment wave modelling studies at other study areas which experienced a similar extreme sea-level rise.

Prevailing of longer sediment waves

The relatively short fixed wavelength $\lambda_0 = 250\text{ m}$ which is used for the first two cases dampens for a larger water depth. Through a random initial topography, the last case however shows that longer wavelengths prevail. With the knowledge obtained from this study additional runs for a longer fixed wavelengths have therefore been completed. An initial wavelength of $\lambda_0 = 500\text{ m}$ is chosen which corresponds to the observed wavelength at Area 13N from the AmSedIS project. Here, a wave height of $\Delta S = 24\text{ m}$ is observed. Again, the case study model is used with depth increments. Nonetheless, the Chezy roughness value and tidal velocity amplitude are kept constant at their initial parameter value of Case I thereby only considering sea-level rise. The initial wave amplitude is set to $A_0 = 2\text{ m}$ to reduce computation time. Figure 8.1 shows for each reference depth the (normalised) equilibrium bed level, the wave height and crest-trough position over time. The modelled wave height of $H = 25\text{ m}$ corresponds relatively well with the observed site-specific height.

However, it should be noted that the sensitivity analysis of this study shows that the equilibrium bed level is sensitive to parameter changes. Additionally, data-analysis indicates significantly differing trochoidal sediment waves at each observed site. Furthermore, the model is not capable of establishing a sharp crest despite the fact that the final equilibrium bed level seems to tend towards a trochoidal shape. This might be an effect of excluding certain processes in the initial model set-up. Nevertheless, using this simplified set-up the model demonstrates along with sea-level rise the formation and evolution over time of longer prevailing coarse cores (in assemblage) which are of comparable size as observed in nature (Van Landeghem et al., 2013).

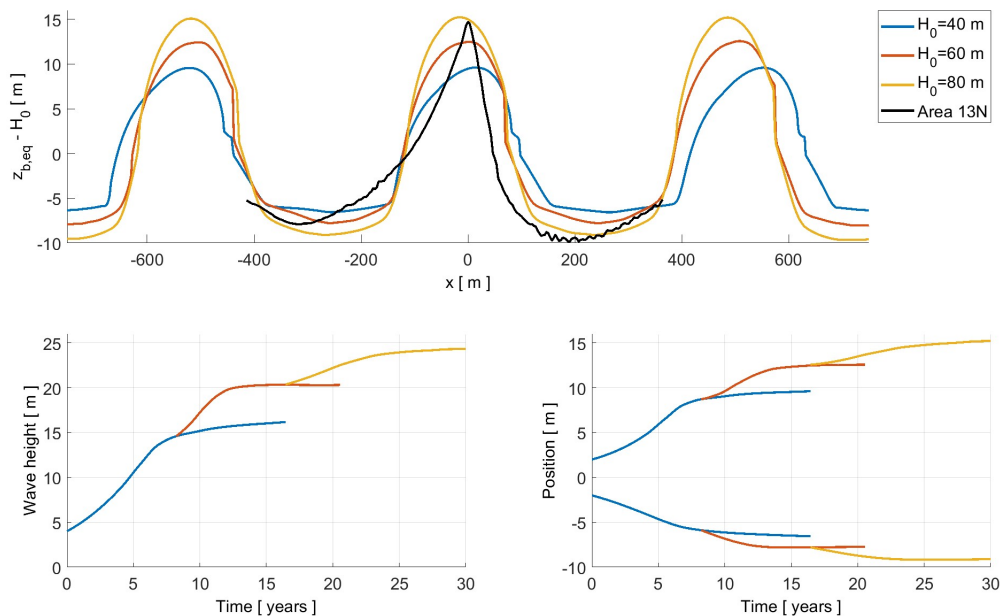


Figure 8.1: The normalised equilibrium bed level ($z_{b,eq} - H_0$) for a fixed initial wavelength of $\lambda_0 = 500$ m, wave height and crest-trough position over time. Note that the equilibrium bed level from the preceding reference water depth is adopted as initial topography. The bed level development over time of the individual runs can be found in Appendix F.7. The bed level at Area 13N is plotted for comparison.

Sorting patterns

The observations and the model output with respect to sorting patterns along trochoidal are somewhat apart. Data-analysis shows that the coarsest sediments are found in the troughs at multiple survey areas which is likely lag exposed in areas of erosion. The simulation with the addition of a sand layer on top of the coarse core however indicates that the sediment waves act as a sand trap. Additionally, the sand layer is observed mainly on the trochoidal sediment wave flanks (Van Landeghem et al., 2009a). Nevertheless, the sand layer on top of the coarse core is mobile which is in line with observations. However, Van Landeghem et al. (2009a) refers to high-energy events such as storms whereas its mobility for this study is dependent on the tide. Therefore, more research is required in both the field and modelling area.

Excluded processes

A residual current is neglected during this study as it initiates asymmetry and migration thereby increasing complexity. This research only considers one symmetrical tidal constituent which results in symmetrical sediment waves, see Figure 8.1. It should be noted that the asymmetry for $H_0 = 40$ m in this figure is induced by the relatively high MORFAC value, cf. Appendix F.1. The observed trochoidal sediment waves in the Irish Sea are however slightly asymmetrical most likely due to the combination of tidal constituents and a residual current. Additionally, this study considers very fine gravel while significantly coarser sediments are found along trochoidal sediment waves. As Van Landeghem et al.

(2009a) stated, the central Irish Sea is associated with bed load convergence and divergence zones. The long-term reversals of the slightly dominant current-induced bed stresses in these zones in combination with a nearly symmetrical tide might have contributed significantly to bi-directionally piling up of even coarser gravels.

The hiding-exposure effect is not included during the model simulations of the initial morphodynamic response due to the addition of a thin sand layer at the bed. The hiding-exposure effect represents the process in which larger and more exposed grains hide the smaller particles from the flow (McCarron et al., 2019) which enhances for poorly sorted mixtures. For example, Area 14E shows a coarse multi modal distribution with a fine skewness which is possible evidence of hiding-exposure. Throughout the model simulations gravel and sand are gradually mixed and sorted. The results show that the sand fraction of the active transport layer is dependent on space and time. Figure 8.2 shows the calculated hiding-exposure along the sediment wave after one tidal cycle following Egiazaroff (1965). Despite the statement by McCarron et al. (2019) that this formulation might overpredict the hiding-exposure factor, this figure gives a clear spatial pattern of its importance. The hiding-exposure factor for sand at the crest and in a lesser extend at the flanks is significantly higher than at the sandy trough. Thus, sand at the trough has more potential to be eroded as gravel at the crest and flanks protects the sand from the flow. In contrast, gravel is at these locations more likely to be eroded. This will most likely result in less sand transported from crest and flanks to trough thereby increasing the fraction of sand in the upper part of the sediment wave.

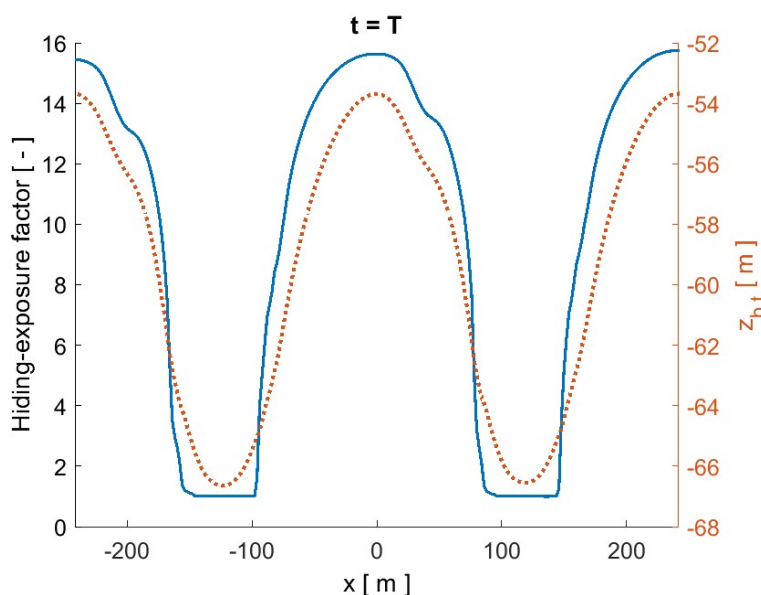


Figure 8.2: The hiding-exposure factor for sand ($d_s = 0.3\text{ mm}$) following Egiazaroff (1965) along the sediment wave after one tidal cycle with $MF = 25$.

Uncertainty GIA model output and AmSedIS data set

In the model of Uehara et al. (2006), a constant and uniform bottom friction coefficient was used. Thereby, the spatial variability of bottom sediment types and the form drag resulting from sub-grid scale bedforms were neglected. The latter was expected to significantly affect the model outcomes of the tidal ellipse and peak induced bed shear stress. Additionally, the wave climate was not considered over the large timescale. It is expected that the peak bed stresses have probably been higher than simulated as is stated by Van Landeghem et al. (2009a). Therefore, the uncertainty regarding the tidal ellipse and thus the peak induced bed stresses was assumed large. It should also be noted that these types of GIA models have been updated in the last decade (e.g. Ward et al., 2016). By comparing the maximum induced bed shear stresses from the GIA model and the 2DV case study model higher peak bed shear stresses are required to generate sediment waves of a comparable size with very fine gravel in Delft3D. However, much coarser sediments were found in the grab samples along trochoidal sediment waves. Therefore, high-energy events which are not considered during this modelling study most-likely have

played a significant role in piling up these coarser gravel grains, especially during earlier periods of lower water depths.

The amount of sediment wave observations during the AmSedIS project is limited. In total, 22 sediment waves were analysed for granulometric variations, of which only 7 with trochoidal shape and a significant wave height. Such a small population size increases uncertainties considerably which complicates finding significant correlations. In addition, Van Landeghem et al. (2013) also mentioned that during the AmSedIS project difficulties emerged during the collection of the vibrocores which could have affected the grab samples and could explain that the amount and locations of the grab samples along the trochoidal sediment waves differ for each survey area. This limited this study to thoroughly investigate a certain trend in the cross-sectional direction of trochoidal sediment waves.

Simplifications

Grab samples show a large variety of gravel found along trochoidal sediment waves in the Irish Sea. A unimodal gravel mixture is however not included to model the formation and evolution of the coarse core. Here, a uniformly mixed bed of very fine gravel is implemented. Very coarse gravel is significantly more difficult to get entrained by the flow. Therefore, it is expected that with these grain sizes even larger tidal velocity amplitudes are needed to model sediment wave growth. Including a unimodal gravel mixture in combination with the hiding-exposure effect however might potentially enhance the initial growth of the coarse core of sediment waves as is stated by Van Landeghem et al. (2013).

Furthermore, the Chezy roughness value is kept constant throughout the simulation of both modelling phases. However, due to its dependency on the grain size and the water depth the roughness should vary in space and time during the long-term sediment wave development and due to the mobile sand layer. This results in a greater roughness at the crests compared to the troughs due to the significant depth difference. In addition, the accumulation of sand at the troughs results in a smoother bed in comparison to the coarser crests. This most likely affects the model results as this study shows that the Chezy roughness value strongly influences the maximum bed shear stresses, the fastest growing mode and the equilibrium wave height.

At last, the model is sensitive to parameter changes as is shown in the sensitivity analysis. However, the model is tested for a certain parameter range and is therefore considered reliable. In addition, the general aims to model the evolution of sediment waves over a significant period of time and to determine the initial morphodynamic response due to the added sand layer are unaffected by this parameter sensitivity and the idealized model setting.

9

Conclusions

In this thesis the formation and evolution of trochoidal sediment waves in the Irish Sea is explored using and by adapting an existing sand wave model in Delft3D-4. With the knowledge gained through data-analysis and simulations the research questions as stated in Section 1.3 are answered in this chapter.

I. What are the palaeo-tidal conditions and present-day morphological characteristics of trochoidal sediment waves in the Irish Sea?

The reconstruction of the palaeo-tidal conditions using the glacial isostatic adjustment model shows a clear trend for the peak bed shear stresses and the water depth in the Irish Sea. After the Last Glacial Maximum, temperatures evolved gradually and the British-Irish Ice Sheet retreated allowing water to enter the Irish Sea increasing the depth over time for several tens of metres. In addition, enhanced ocean tidal dynamics and local configuration changes greatly intensified peak bed shear stresses between 7,000 and 15,000 years before present. Nonetheless, hydrodynamics stabilised around 6,000 years ago. For the locations at which trochoidal sediment waves are observed the output of the model is in line with this theory.

Trochoidal sediment wave characteristics and grab samples of in total seven survey areas from the Amplified Sediment wave Irish Sea project are analysed. Wave heights range between 11 to 35 metres, whereas wavelengths extend from 340 to 560 m. The water depths differ significantly from one location to another, i.e. 80 to 160 m. Along the trochoidal sediment waves, most grab samples consist of multimodal sediment mixtures, i.e. mainly a combination of medium sand with fine gravel. The coarsest sediments are found in the troughs. Furthermore, the trochoidal sediment wave height correlates negatively and positively with the mean and its deviation of the most dominant mode from the combined grain size distributions, respectively. The present-day morphology of trochoidal sediment waves however remains relatively site-specific.

II. In what way can an existing sand wave model be adjusted to reconstruct the formation and evolution of the coarse core of trochoidal sediment waves during the post-glacial period?

Since the model set-up of the existing sand wave model is based on present-day sand waves in the North Sea, the setting is initially adjusted to generate sediment waves with parameter values according to the Irish Sea. Trochoidal sediment wave fields in the Irish Sea are found at considerable greater depths and consist of coarser sediments as follows from the first research question. After a grid refinement study, a sensitivity analysis is conducted to determine the influence of the numerical model and process parameters. Here, it is found that the Chezy roughness value and tidal velocity amplitude most affect the maximum induced bed shear stress and equilibrium wave height.

Through a 2DV case study model the formation and evolution of trochoidal sediment waves during the post-glacial period is subsequently analysed using the adjusted process-based sand wave model. Three cases are linked to a specific time period in which significant sea level rise and enhanced peak bed stresses in the Irish Sea. Although the sediment waves grow along with the water depth after the first jump in time, they dampen for the largest depth due to its fixed and relatively small wavelength. The long-term behaviour for a random initial bed level however shows significant wave heights and wavelengths comparable to those observed.

III. What is the initial morphodynamic response of equilibrium stage sediment waves due to the addition of a thin sand layer at the surface?

Through layered bed stratigraphy a thin sand layer is added to the system on top of sediment waves in equilibrium state. This sand represents the mobile sand veneer that is observed hosting the coarse core of present-day trochoidal sediment waves. Short-term model simulations show the initial morphodynamic behaviour and sorting patterns along sediment waves.

These simulations indicate that the sand layer is mobile as is observed in nature and the sorting pattern of the active transport layer is dependent on time. The sand at the trough and flanks clearly follows the direction of the tide. Over time, sand covers the flanks and the troughs of the coarse core thereby decreasing its original height while moving towards a new equilibrium bed level and acting as a sand trap. At equilibrium the sand fraction at the crest and flank shows a clear pattern in relation to the direction and magnitude of the flow. The equilibrium sand fraction of the top layer at the trough increases during slack water and due to transport from the crest and flanks.

These research questions jointly contribute to the main aim of this study, i.e. to explain the formation and evolution of trochoidal sediment waves in the Irish Sea throughout their post-glacial history using an existing process-based sand wave model. Despite the simplified model set-up, this study shows the growth of the coarse core of sediment waves over a millennial scale which is characterised by a significant sea level rise and enhanced hydrodynamics. In addition, the model is able to reproduce the mobile sand veneer that is observed hosting this coarse core.

10

Recommendations

Further research about trochoidal sediment waves with the Delft3D model will potentially help to better understand these millennia-old bed features. The case study model is considered a starting point for new modelling studies about trochoidal sediment waves. In this chapter some recommendations are discussed for further research.

Model set-up

The model set-up used in this research is unique in comparison to previous sand wave modelling studies which assume a fixed water depth. However, the system changes for each new situation. This makes it difficult to predict how the system will behave and to choose an initial setting. For example, the initially chosen (short) wavelength dampened for larger water depths during this study. It is therefore recommended to conduct test runs for future phases. In addition, the quantitative results should be treated carefully due to this constantly changing system. Nevertheless, this set-up has great potential to model on a large time-scale associated with significant uncertainties and to qualitatively support hypotheses.

Application of the case study model for other study areas

The case study model of this research is linked to the extreme sea-level rise and changing tidal dynamics in the Irish Sea during the post-glacial period. However, other shallow and tide-controlled marine environments have also experienced glaciations and the resulting extreme changes in tidal conditions, e.g. the North Sea. Here, previous sand wave modelling studies generally assume an initial flat bed for contemporary water depths.

Sand waves may nevertheless already exist for a long period of time while sea-levels rose significantly after the glacial period as is shown by Albarracín et al. (2014). On the other hand, present-day sand waves will most likely evolve with the sea-level rise that is expected for the upcoming decades. Therefore, it is recommended to take into account sea-level rise through a case study model (or an implementation of sea-level rise in the Delft3D model) for other study areas.

Collecting more grab sample data

The available data at the survey areas is rather limited, i.e. relatively small amounts of grab samples. Additionally, the location of the grab samples along the observed trochoidal sediment waves differs significantly. This resulted in no trends being found. Therefore, it is recommended to gather more grab samples along the trochoidal sediment waves which could potentially help to find grain size trends over multiple sediment waves. These trends can then be compared to model outputs.

Exploring the influence of other processes

The hiding-exposure factor is dependent on space and time throughout the morphological evolution of sediment waves. By including the hiding-exposure effect in combination with a uni- or bimodal sediment mixture, insight can be gained into the potential increase in initial growth and into the sorting pattern of the coarse core. Additionally, the interaction between the mobile sand layer and the coarse core can be modelled more realistically.

High energy events are expected to contribute to the motion of the coarsest sediments found in the coarse core of trochoidal sediment waves. These events can affect the mobile sand veneer and can even lead to partial or complete erosion of present-day bedforms to leave only lateral scour marks. These high energy events can be included in Delft3D through extreme wind conditions as is done by Cao et al. (2021).

At last, it is recommended to examine the influence of the residual current on the model results. The shifting position of the bed load divergence and convergence zones in the Irish Sea is believed to have contributed significantly to the bi-directional accumulation of coarse sediment. This shifting position can be explored in the model through a constantly reversing residual current in combination with a symmetrical tide.

References

- Albarracín, S., Alcántara-Carrió, J., Montoya-Montes, I., Fontán-Bouzas, , Somoza, L., Amos, C. L., & Salgado, J. R. (2014). Relict sand waves in the continental shelf of the gulf of valencia (western mediterranean). *Journal of Sea Research*, 93, 33–46. <https://doi.org/10.1016/j.seares.2013.12.014>
- Aliotta, S. & Perillo, G. M. E. (1987). A sand wave field in the entrance to bahia blanca estuary, argentina. *Marine Geology*, 76, 1–14. [https://doi.org/10.1016/0025-3227\(87\)90013-2](https://doi.org/10.1016/0025-3227(87)90013-2)
- Anthony, D. & Leth, J. O. (2002). Large-scale bedforms, sediment distribution and sand mobility in the eastern north sea off the danish west coast. *Marine Geology*, 182(3), 247–263. [https://doi.org/10.1016/S0025-3227\(01\)00245-6](https://doi.org/10.1016/S0025-3227(01)00245-6)
- Antia, E. E. (1995). Vertical patterns of grain-size parameters of shoreface-connected ridges in the german bight. *Oceanographic Literature Review*, 6(42), 449.
- Bagnold, R. A. (1966). An approach to the sediment transport problem from general physics. *U.S. Geological Survey Professional Paper*, 104(4), 422–l: v + 37. <https://doi.org/10.1017/S0016756800049074>
- Barnard, P. L., Hanes, D. M., Rubin, D. M., & Kvitek, R. G. (2006). Giant sand waves at the mouth of san francisco bay. *Eos, Transactions American Geophysical Union*, 87(29), 285–289. <https://doi.org/10.1029/2006E0290003>
- Barrie, J. V., Conway, K. W., Picard, K., & Greene, H. G. (2009). Large-scale sedimentary bedforms and sediment dynamics on a glaciated tectonic continental shelf: Examples from the pacific margin of canada. *Continental Shelf Research*, 29(5-6), 796–806. <https://doi.org/10.1016/j.csr.2008.12.007>
- Besio, G., Blondeaux, P., Brocchini, M., Hulscher, S. J. M. H., Idier, D., Knaapen, M. A. F., Németh, A., Roos, P. C., & Vittori, G. (2008). The morphodynamics of tidal sand waves: A model overview. *Coastal engineering*, 55(7-8), 657–670.
- Besio, G., Blondeaux, P., Brocchini, M., & Vittori, G. (2004). On the modeling of sand wave migration. *Journal of Geophysical Research: Oceans*, 109(C4). <https://doi.org/10.1029/2002JC001622>
- Blondeaux, P. & Vittori, G. (2010). Formation of tidal sand waves: Effects of the spring-neap cycle. *Journal of Geophysical Research: Oceans*, 115(C10). <https://doi.org/10.1029/2010JC006400>
- Blott, S. J. & Pye, K. (2001). Gradstat: a grain size distribution and statistics package for the analysis of unconsolidated sediments. *Earth surface processes and Landforms*, 26(11), 1237–1248. <https://doi.org/10.1002/esp.261>
- Bokuniewicz, H. J., Gordon, R. B., & Kastens, K. A. (1977). From and migration of sand waves in a large estuary, long island sound. *Marine Geology*, 24(3), 185–199. [https://doi.org/10.1016/0025-3227\(77\)90027-5](https://doi.org/10.1016/0025-3227(77)90027-5)
- Borsje, B. W., Bouma, T. J., Rabaut, M., Herman, P. M. J., & Hulscher, S. J. M. H. (2014a). Formation and erosion of biogeomorphological structures: A model study on the tube-building polychaete *lanice conchilega*. *Limnology and Oceanography*, 59(4), 1297–1309.
- Borsje, B. W., Kranenburg, J. W. M., Roos, P. C., Matthieu, J., & Hulscher, S. J. M. H. (2014b). The role of suspended load transport in the occurrence of tidal sand waves. *Journal of Geophysical Research: Earth Surface*, 119(4), 701–716. <https://doi.org/10.1002/2013JF002828>

- Borsje, B. W., Roos, P. C., Kranenburg, J. W. M., & Hulscher, S. J. M. H. (2013). Modeling tidal sand wave formation in a numerical shallow water model: The role of turbulence formulation. *Continental Shelf Research*, 60, 17–27. <https://doi.org/10.1016/j.csr.2013.04.023>
- Bradley, R. W. & Venditti, J. G. (2017). Reevaluating dune scaling relations. *Earth-Science Reviews*, 165, 356–376. <https://doi.org/10.1016/j.earscirev.2016.11.004>
- Burchard, H., Craig, P. D., Gemmrich, J. R., van Haren, H., Mathieu, P.-P., Meier, H. E. M., Smith, W. A. M. N., Prandke, H., Rippeth, T. P., Skillingstad, E. D., Smyth, W. D., Welsh, D. J. S., & Wijesekera, H. W. (2008). Observational and numerical modeling methods for quantifying coastal ocean turbulence and mixing. *Progress in Oceanography*, 76(4), 399–442. <https://doi.org/doi.org/10.1016/j.pocean.2007.09.005>
- Campmans, G. H. P. (2018). *Modeling storm effects on sand wave dynamics*. <https://doi.org/10.3990/1.9789036546003>
- Campmans, G. H. P., Roos, P. C., & Hulscher, S. J. M. H. (2019). Storm influences on sand wave dynamics: an idealized modelling approach. *MARID VI*, 33.
- Campmans, G. H. P., Roos, P. C., Van der Sleen, N. R., & Hulscher, S. J. M. H. (2021). Modeling tidal sand wave recovery after dredging: effect of different types of dredging strategies. *Coastal Engineering*, 165, 103862. <https://doi.org/10.1016/j.coastaleng.2021.103862>
- Cao, G., Jiang, W., & Lin, M. (2021). A physically-modified spectral model for prediction of sand wave migration. *Continental Shelf Research*, 230, 104573. <https://doi.org/10.1016/j.csr.2021.104573>
- Cartwright, D. E. (1959). On submarine sand-waves and tidal lee-waves. *Proceedings of the Royal Society of London. Series A. Mathematical and Physical Sciences*, 253(1273), 218–241.
- Cheng, C. H., Soetaert, K., & Borsje, B. W. (2020). Sediment characteristics over asymmetrical tidal sand waves in the dutch north sea. *Journal of Marine Science and Engineering*, 8(6), 409. <https://doi.org/10.3390/jmse8060409>
- Cherlet, J., Besio, G., Blondeaux, P., Van Lancker, V., Verfaillie, E., & Vittori, G. (2007). Modeling sand wave characteristics on the belgian continental shelf and in the calais-dover strait. *Journal of Geophysical Research: Oceans*, 112(C6). <https://doi.org/10.1029/2007JC004089>
- Church, M. & Haschenburger, J. (2017). What is the “active layer”? *Water Resources Research*, 53(1), 5–10.
- Clark, C. D., Ely, J. C., Hindmarsh, R. C., Bradley, S., Ignéczi, A., Fabel, D., Cofaigh, C. Ó., Chiverrell, R. C., Scourse, J., Benetti, S., et al. (2022). Growth and retreat of the last british–irish ice sheet, 31 000 to 15 000 years ago: the britice-chrono reconstruction. *Boreas*, 51(4), 699–758.
- Clark, C. D., Hughes, A. L. C., Greenwood, S. L., Jordan, C., & Sejrup, H. P. (2012). Pattern and timing of retreat of the last british-irish ice sheet. *Quaternary Science Reviews*, 44, 112–146. <https://doi.org/10.1016/j.quascirev.2010.07.019>
- Creane, S., O’Shea, M., Coughlan, M., & Murphy, J. (2021). The irish sea bed load parting zone: Is it a mid-sea hydrodynamic phenomenon or a geological theoretical concept? *Estuarine, Coastal and Shelf Science*, 263, 107651. <https://doi.org/10.1016/j.ecss.2021.107651>
- Cronan, D. S. (1972). Skewness and kurtosis in polymodal sediments from the irish sea. *Journal of Sedimentary Research*, 42(1), 102–106.
- Damen, J. M., van Dijk, T. A. G. P., & Hulscher, S. J. M. H. (2018). Spatially varying environmental properties controlling observed sand wave morphology. *Journal of Geophysical Research: Earth Surface*, 123(2), 262–280.

- Damveld, J., Porcile, G., Blondeaux, P., & Roos, P. (2021). Nonlinear dynamics of sand waves in sediment scarce environments. <https://doi.org/10.5194/egusphere-egu21-16019>. EGU General Assembly 2021 : vEGU21: Gather Online, EGU21 ; Conference date: 19-04-2021 Through 30-04-2021
- Damveld, J. H. (2020). *The feedbacks among tidal sand waves, benthic organisms and sediment sorting processes*. <https://doi.org/10.3990/1.9789036550000>
- Damveld, J. H., Borsje, B. W., Roos, P. C., & Hulscher, S. J. M. H. (2020a). Biogeomorphology in the marine landscape: Modelling the feedbacks between patches of the polychaete worm *lanice conchilega* and tidal sand waves. *Earth surface processes and landforms*, 45(11), 2572–2587.
- Damveld, J. H., Borsje, B. W., Roos, P. C., & Hulscher, S. J. M. H. (2020b). Horizontal and vertical sediment sorting in tidal sand waves: Modeling the finite-amplitude stage. *Journal of Geophysical Research: Earth Surface*, 125. <https://doi.org/10.1029/2019JF005430>
- Deltares (2022). Delft3d-flow, simulation of multi-dimensional hydrodynamic flows and transport phenomena, including sediments. user manual. Report, Deltares.
- Dobson, M. R., Evans, W. E., & James, K. H. (1971). The sediment on the floor of the southern irish sea. *Marine Geology*, 11(1), 27–69. [https://doi.org/10.1016/0025-3227\(71\)90083-1](https://doi.org/10.1016/0025-3227(71)90083-1)
- Egiazaroff, I. V. (1965). Calculation of nonuniform sediment concentrations. *Journal of the Hydraulics Division*, 91(4), 225–247. <https://doi.org/doi:10.1061/JYCEAJ.0001277>
- Field, M. E., Nelson, C. H., Cacchione, D. A., & Drake, D. E. (1981). Sand waves on an epicontinental shelf: Northern bering sea. *Marine Geology*, 42(1), 233–258. [https://doi.org/10.1016/0025-3227\(81\)90165-1](https://doi.org/10.1016/0025-3227(81)90165-1)
- Figueiredo, A. G. D. (1980). Response of water column to strong wind forcing, southern brazilian inner shelf: implications for sand ridge formation. *Marine Geology*, 35(4), 367–376. [https://doi.org/10.1016/0025-3227\(80\)90126-7](https://doi.org/10.1016/0025-3227(80)90126-7)
- Flemming, B. W. (1978). Underwater sand dunes along the southeast african continental margin — observations and implications. *Marine Geology*, 26(3), 177–198. [https://doi.org/10.1016/0025-3227\(78\)90059-2](https://doi.org/10.1016/0025-3227(78)90059-2)
- Flemming, B. W. & Kudrass, H.-R. (2018). Large dunes on the outer shelf off the zambezi delta, mozambique: evidence for the existence of a mozambique current. *Geo-Marine Letters*, 38(1), 95–106. <https://doi.org/doi.org/10.1007/s00367-017-0515-5>
- Folk, R. L. (1954). The distinction between grain size and mineral composition in sedimentary-rock nomenclature. *The Journal of Geology*, 62(4), 344–359.
- Franzetti, M., Le Roy, P., Delacourt, C., Garlan, T., Cancouët, R., Sukhovich, A., & Deschamps, A. (2013). Giant dune morphologies and dynamics in a deep continental shelf environment: Example of the banc du four (western brittany, france). *Marine Geology*, 346, 17–30. <https://doi.org/10.1016/j.margeo.2013.07.014>
- Games, K. & Gordon, D. (2015). Study of sand wave migration over five years as observed in two windfarm development areas, and the implications for building on moving substrates in the north sea. *Earth and Environmental Science Transactions of the Royal Society of Edinburgh*, 105, 1–9. <https://doi.org/10.1017/S1755691015000110>
- Harris, P. T. (1989). Sandwave movement under tidal and wind-driven currents in a shallow marine environment: Adolphus channel, northeastern australia. *Continental Shelf Research*, 9(11), 981–1002. [https://doi.org/10.1016/0278-4343\(89\)90003-4](https://doi.org/10.1016/0278-4343(89)90003-4)
- Hirano, M. (1971). River-bed degradation with armoring. *Proceedings of the Japan society of civil engineers*, volume 1971, 55–65.

- Horrillo-Caraballo, J. M., Yin, Y., Fairley, I., Karunaratna, H., Masters, I., & Reeve, D. E. (2021). A comprehensive study of the tides around the welsh coastal waters. *Estuarine, Coastal and Shelf Science*, 254, 107326. <https://doi.org/10.1016/j.ecss.2021.107326>
- Howarth, M. J. (1984). Currents in the eastern irish sea. *Oceanogr. Mar. Biol. Ann. Rev.*, 22, 11–54.
- Howarth, M. J. (2005). *Hydrography of the Irish Sea*, 30. UK Department of Trade and Industry's offshore energy-Strategic Environmental Assessment programme. <https://doi.org/10.1.1.692.9264>
- Huisman, B., Ruessink, B., De Schipper, M., Luijendijk, A., & Stive, M. (2018). Modelling of bed sediment composition changes at the lower shoreface of the sand motor. *Coastal Engineering*, 132, 33–49.
- Hulscher, S. J. M. H. (1996). Tidal-induced large-scale regular bed form patterns in a three dimensional shallow water model. *Journal of Geophysical Research*, 101, 20727–20744.
- Hulscher, S. J. M. H. & Dohmen-Janssen, C. M. (2005). Introduction to special section on marine sand wave and river dune dynamics. *Journal of Geophysical Research: Earth Surface*, 110(F4). <https://doi.org/10.1029/2005JF000404>
- Jackson, D. I., Jackson, A. A., Evans, D., Wingfield, R. T. R., Barnes, R. P., & Arthur, M. J. (1995). The geology of the irish sea.
- Katoh, K., Kume, H., Kuroki, K., & Hasegawa, J. (1999). The development of sand waves and the maintenance of navigation channels in the bisanseto sea. *Coastal engineering 1998*, 3490–3502.
- Krumbein, W. C. (1934). Size frequency distributions of sediments. *Journal of Sedimentary Research*, 4(2), 65–77. <https://doi.org/10.1306/d4268eb9-2b26-11d7-8648000102c1865d>
- Lambeck, K. (1995). Late devensian and holocene shorelines of the british isles and north sea from models of glacio-hydro-isostatic rebound. *Journal of the Geological Society*, 152(3), 437–448. <https://doi.org/10.1144/gsjgs.152.3.0437>
- Leenders, S., Damveld, J. H., Schouten, J., Hoekstra, R., Roetert, T. J., & Borsje, B. W. (2021). Numerical modelling of the migration direction of tidal sand waves over sand banks. *Coastal Engineering*, 163, 103790. <https://doi.org/10.1016/j.coastaleng.2020.103790>
- Lesser, G. R., Roelvink, J. A., van Kester, J. A. T. M., & Stelling, G. S. (2004). Development and validation of a three-dimensional morphological model. *Coastal Engineering*, 51(8), 883–915. <https://doi.org/10.1016/j.coastaleng.2004.07.014>
- Lykousis, V. (2001). Subaqueous bedforms on the cyclades plateau (ne mediterranean) — evidence of cretan deep water formation? *Continental Shelf Research*, 21(5), 495–507. [https://doi.org/10.1016/S0278-4343\(00\)00104-7](https://doi.org/10.1016/S0278-4343(00)00104-7)
- Ma, X. (2021). Exploring the evolution of seafloor sand dunes. *Earth and Environment*.
- McCarron, C. J., Van Landeghem, K. J. J., Baas, J. H., Amoudry, L. O., & Malarkey, J. (2019). The hiding-exposure effect revisited: A method to calculate the mobility of bimodal sediment mixtures. *Marine Geology*, 410, 22–31. <https://doi.org/10.1016/j.margeo.2018.12.001>
- Mellet, C. L., Long, D., Carter, G., Chiverell, R. C., & van Landeghem, K. J. J. (2015). Geology of the seabed and shallow subsurface: the irish sea. british geological survey commissioned report. Report, CR/15/057. 52pp.
- Neto, A. R. X., de Morais, J. O., & Ciarlini, C. (2018). Modern and relict sedimentary systems of the semi-arid continental shelf in ne brazil. *Journal of South American Earth Sciences*, 84, 56–68.
- Németh, A. A., Hulscher, S. J. M. H., & de Vriend, H. (2003). Offshore sand wave dynamics, engineering problems and future solutions. *Applied Physics Letters - APPL PHYS LETT*, 230, 67–69.

- Németh, A. A., Hulscher, S. J. M. H., & de Vriend, H. J. (2002). Modelling sand wave migration in shallow shelf seas. *Continental Shelf Research*, 22(18-19), 2795–2806. [https://doi.org/10.1016/S0278-4343\(02\)00127-9](https://doi.org/10.1016/S0278-4343(02)00127-9)
- Park, S.-C., Han, H.-S., & Yoo, D.-G. (2003). Transgressive sand ridges on the mid-shelf of the southern sea of korea (korea strait): formation and development in high-energy environments. *Marine Geology*, 193(1), 1–18. [https://doi.org/10.1016/S0025-3227\(02\)00611-4](https://doi.org/10.1016/S0025-3227(02)00611-4)
- Parker, G., Klingeman, P. C., & McLean, D. G. (1982). Bedload and size distribution in paved gravel-bed streams. *Journal of the Hydraulics Division*, 108(4), 544–571. <https://doi.org/doi:10.1061/JYCEAJ.0005854>
- Peltier, W. R. (1994). Ice age paleotopography. *Science*, 265(5169), 195–201. <https://doi.org/10.1126/science.265.5169.195>
- Perillo, M. M., Best, J. L., & García, M. H. (2014). A new phase diagram for combined-flow bedforms. *Journal of Sedimentary Research*, 84, 301–313. <https://doi.org/10.2110/jsr.2014.25>
- Pugh, D. T. (1981). Tidal amphidrome movement and energy dissipation in the irish sea. *Geophysical Journal International*, 67(2), 515–527. <https://doi.org/10.1111/j.1365-246X.1981.tb02763.x>
- Ranasinghe, R., Swinkels, C., Luijendijk, A., Roelvink, D., Bosboom, J., Stive, M., & Walstra, D. (2011). Morphodynamic upscaling with the morfac approach: Dependencies and sensitivities. *Coastal Engineering*, 58(8), 806–811. <https://doi.org/10.1016/j.coastaleng.2011.03.010>
- Reniers, A., Gallagher, E., MacMahan, J., Brown, J., Van Rooijen, A., Van Thiel de Vries, J., & Van Prooijen, B. (2013). Observations and modeling of steep-beach grain-size variability. *Journal of Geophysical Research: Oceans*, 118(2), 577–591.
- Ribberink, J. S. (1987). Mathematical modelling of one-dimensional morphological changes in rivers with non-uniform sediment.
- Robinson, I. S. (1979). The tidal dynamics of the irish and celtic seas. *Geophysical Journal International*, 56(1), 159–197. <https://doi.org/10.1111/j.1365-246X.1979.tb04774.x>
- Rodi, W. (1984). Turbulence models and their application in hydrodynamics—a state of the art review. *Univ. of Karlsruhe, Karlsruhe, Germany*.
- Roetert, T., Raaijmakers, T., & Borsje, B. W. (2017). Cable route optimization for offshore wind farms in morphodynamic areas. *The 27th international ocean and polar engineering conference*, 595–606.
- Roos, P. C., Hulscher, S., Van Der Meer, F., Van Dijk, T., Wientjes, I. G., & van den Berg, J. (2007). Grain size sorting over offshore sandwaves: Observations and modelling. *Proceedings of the 5th IAHR Symposium on River, Coastal and Estuarine Morphodynamics, Enschede, The Netherlands*, 17–21. <https://doi.org/10.1201/NOE0415453639-c84>
- Santoro, V. C., Amore, E., Cavallaro, L., & De Lauro, M. (2004). Evolution of sand waves in the messina strait, italy. *Ocean Dynamics*, 54(3-4), 392–398.
- Singh, A. (2021). The effect of wind and waves on the hydrodynamic and morphodynamic properties of sand waves. <http://essay.utwente.nl/89146/>
- Sterlini, F. (2009). *Modelling sand wave variation*. <https://doi.org/10.3990/1.9789036528511>
- Sun, D., Bloemendal, J., Rea, D. K., Vandenberghe, J., Jiang, F., An, Z., & Su, R. (2002). Grain-size distribution function of polymodal sediments in hydraulic and aeolian environments, and numerical partitioning of the sedimentary components. *Sedimentary Geology*, 152, 263–277. [https://doi.org/10.1016/S0037-0738\(02\)00082-9](https://doi.org/10.1016/S0037-0738(02)00082-9)
- Tappin, D. R., Chadwick, R. A., Jackson, A. A., Wingfield, R. T. R., & Smith, N. J. P. (1994). The geology of cardigan bay and the bristol channel. british geological survey, uk offshore regional report.

- Tonnon, P. K., Van Rijn, L. C., & Walstra, D. J. R. (2007). The morphodynamic modelling of tidal sand waves on the shoreface. *Coastal Engineering*, 54(4), 279–296. <https://doi.org/10.1016/j.coastaleng.2006.08.005>
- Uehara, K., Scourse, J. D., Horsburgh, K. J., Lambeck, K., & Purcell, A. P. (2006). Tidal evolution of the northwest european shelf seas from the last glacial maximum to the present. *Journal of Geophysical Research: Oceans*, 111(C9). <https://doi.org/10.1029/2006JC003531>
- Valentine, P. C., Malczyk, J., & Middleton, T. (2002). *Maps Showing Sea Floor Topography, Sun-Illuminated Sea Floor Topography, and Backscatter Intensity of Quadrangles 1 and 2 in the Great South Channel Region, Western Georges Bank*. US Geological Survey. <https://doi.org/10.3133/i2698>
- Van der Sande, W. M., Roos, P. C., Gerkema, T., & Hulscher, S. J. M. H. (2021). Gravitational circulation as driver of upstream migration of estuarine sand dunes. *Geophysical Research Letters*, 48(14), e2021GL093337. <https://doi.org/10.1029/2021GL093337>
- Van der Wegen, M., Jaffe, B., & Roelvink, J. (2011). Process-based, morphodynamic hindcast of decadal deposition patterns in san pablo bay, california, 1856–1887. *Journal of Geophysical Research: Earth Surface*, 116(F2).
- Van Gerwen, W. (2016). Modelling the equilibrium height of offshore sand waves. <http://essay.utwente.nl/71148/>
- Van Gerwen, W., Borsje, B. W., Damveld, J. H., & Hulscher, S. J. M. H. (2018). Modelling the effect of suspended load transport and tidal asymmetry on the equilibrium tidal sand wave height. *Coastal Engineering*, 136, 56–64. <https://doi.org/10.1016/j.coastaleng.2018.01.006>
- Van Landeghem, K. J. J., Baas, J. H., Mitchell, N. C., Wilcockson, D., & Wheeler, A. J. (2012). Reversed sediment wave migration in the irish sea, nw europe: A reappraisal of the validity of geometry-based predictive modelling and assumptions. *Marine Geology*, 295–298, 95–112. <https://doi.org/10.1016/j.margeo.2011.12.004>
- Van Landeghem, K. J. J., Besio, G., Niemann, H., Mellett, C., Huws, D., Steinle, L., O'Reilly, S., Croker, P., Hodgson, D., & Williams, D. (2013). Amplified sediment waves in the irish sea (amsedis). *Hydro International*, 18, 14–17.
- Van Landeghem, K. J. J., Uehara, K., Wheeler, A. J., Mitchell, N. C., & Scourse, J. D. (2009a). Post-glacial sediment dynamics in the irish sea and sediment wave morphology: Data–model comparisons. *Continental Shelf Research*, 29(14), 1723–1736. <https://doi.org/10.1016/j.csr.2009.05.014>
- Van Landeghem, K. J. J., Wheeler, A. J., Mitchell, N. C., & Sutton, G. (2009b). Variations in sediment wave dimensions across the tidally dominated irish sea, nw europe. *Marine Geology*, 263, 108–119. <https://doi.org/10.1016/j.margeo.2009.04.003>
- Van Oyen, T. & Blondeaux, P. (2009a). Grain sorting effects on the formation of tidal sand waves. *Journal of Fluid Mechanics*, 629, 311–342. <https://doi.org/10.1017/S0022112009006387>
- Van Oyen, T. & Blondeaux, P. (2009b). Tidal sand wave formation: Influence of graded suspended sediment transport. *Journal of Geophysical Research*, 114. <https://doi.org/10.1029/2008JC005136>
- Van Oyen, T., Blondeaux, P., & Van den Eynde, D. (2013). Sediment sorting along tidal sand waves: A comparison between field observations and theoretical predictions. *Continental Shelf Research*, 63, 23–33. <https://doi.org/10.1016/j.csr.2013.04.005>
- Van Rijn, L. C. (1993). *Principles of sediment transport in rivers, estuaries and coastal seas*, volume 1006. Aqua publications Amsterdam.
- Van Rijn, L. C. (2007). Unified view of sediment transport by currents and waves. i: Initiation of motion, bed roughness, and bed-load transport. *Journal of Hydraulic engineering*, 133(6), 649–667.
- Van Santen, P., Augustinus, P., Janssen-Stelder, B., Quartel, S., & Tri, N. (2007). Sedimentation in an estuarine mangrove system. *Journal of Asian Earth Sciences*, 29(4), 566–575.

- Velenturf, A. P. M., Emery, A. R., Hodgson, D. M., Barlow, N. L. M., Mohtaj Khorasani, A. M., Van Alstine, J., Peterson, E. L., Piazzolo, S., & Thorp, M. (2021). Geoscience solutions for sustainable offshore wind development. *Earth Sci. Syst. Soc.*, 1:10042. <https://doi.org/10.3389/esss.2021.10042>
- Verboom, G. K. & Slob, A. (1984). Weakly-reflective boundary conditions for two-dimensional shallow water flow problems. *Advances in Water Resources*, 7(4), 192–197. [https://doi.org/https://doi.org/10.1016/0309-1708\(84\)90018-6](https://doi.org/https://doi.org/10.1016/0309-1708(84)90018-6)
- Wagle, B. G. & Veerayya, M. (1996). Submerged sand ridges on the western continental shelf off bombay, india: evidence for late pleistocene-holocene sea-level changes. *Marine Geology*, 136(1), 79–95. [https://doi.org/10.1016/S0025-3227\(96\)00053-9](https://doi.org/10.1016/S0025-3227(96)00053-9)
- Wang, Y., Zhang, Y., Zou, X., Zhu, D., & Piper, D. (2012). The sand ridge field of the south yellow sea: Origin by river–sea interaction. *Marine Geology*, 291-294, 132–146. <https://doi.org/10.1016/j.margeo.2011.01.001>
- Wang, Z., Liang, B., Wu, G., & Borsje, B. W. (2019). Modeling the formation and migration of sand waves: The role of tidal forcing, sediment size and bed slope effects. *Continental shelf research*, 190, 103986. <https://doi.org/10.1016/j.coastaleng.2006.08.005>
- Ward, S. L., Neill, S. P., Scourse, J. D., Bradley, S. L., & Uehara, K. (2016). Sensitivity of palaeotidal models of the northwest european shelf seas to glacial isostatic adjustment since the last glacial maximum. *Quaternary Science Reviews*, 151, 198–211. <https://doi.org/10.1016/j.quascirev.2016.08.034>
- Ward, S. L., Neill, S. P., Van Landeghem, K. J. J., & Scourse, J. D. (2015). Classifying seabed sediment type using simulated tidal-induced bed shear stress. *Marine Geology*, 367, 94–104. <https://doi.org/10.1016/j.margeo.2015.05.010>
- Ward, S. L., Robins, P. E., Lewis, M. J., Iglesias, G., Hashemi, M. R., & Neill, S. P. (2018). Tidal stream resource characterisation in progressive versus standing wave systems. *Applied energy*, 220, 274–285.
- Wentworth, C. K. (1922). A scale of grade and class terms for clastic sediments. *The journal of geology*, 30(5), 377–392.
- Williams, R., Measures, R., Hicks, D., & Brasington, J. (2016). Assessment of a numerical model to reproduce event-scale erosion and deposition distributions in a braided river. *Water resources research*, 52(8), 6621–6642.
- Zhou, J., Wu, Z., Jin, X., Zhao, D., Cao, Z., & Guan, W. (2018). Observations and analysis of giant sand wave fields on the taiwan banks, northern south china sea. *Marine Geology*, 406, 132–141. <https://doi.org/10.1016/j.margeo.2018.09.015>

A

Irish Sea

A.1. Quaternary

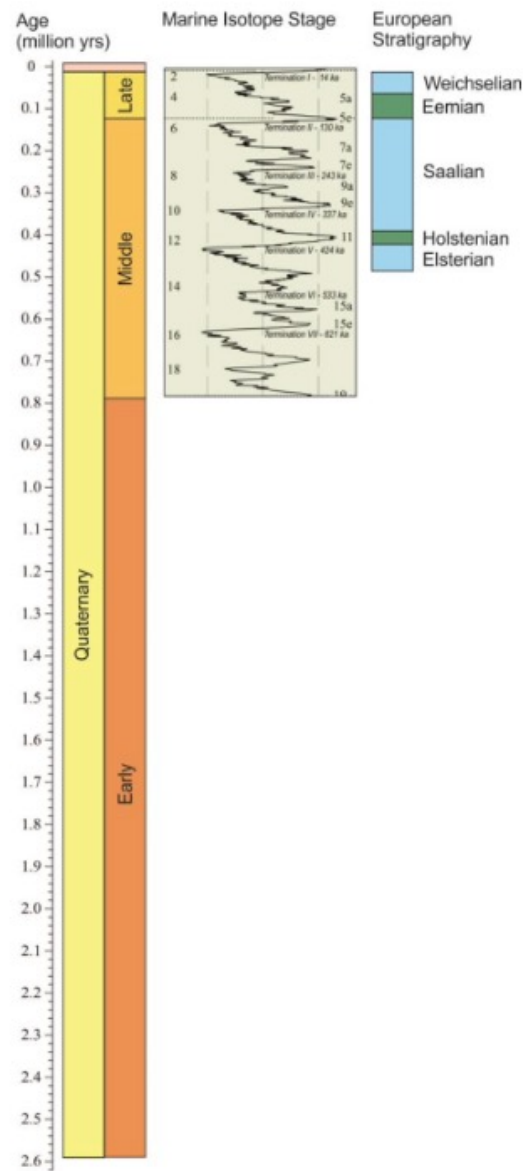


Figure A.1: Stratigraphic subdivision of geological time of the Quaternary (Mellet et al., 2015).

A.2. Map of the present-day Irish Sea

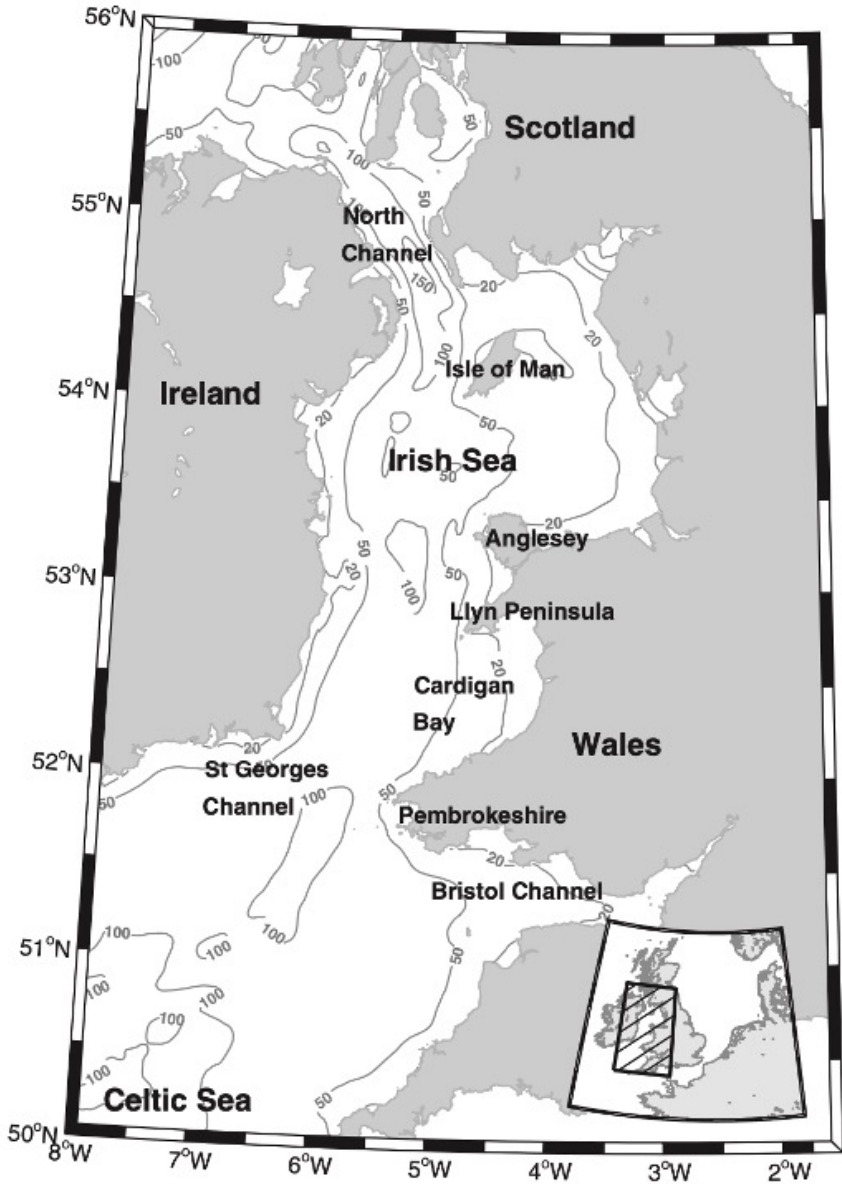


Figure A.2: Present-day Irish Sea with water depth (mean sea level) contours in metres (Ward et al., 2015).

A.3. Amphidromic systems

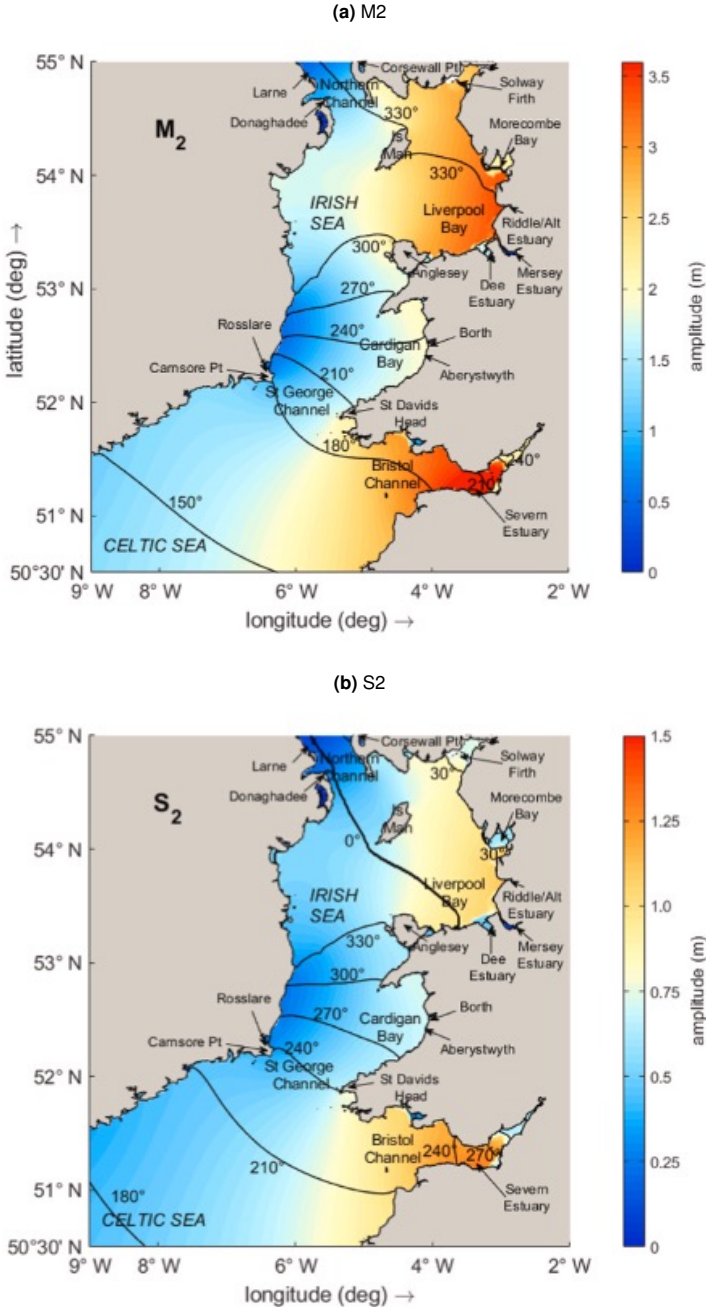


Figure A.3: Amphidromic system of the dominant constituents, (a) M₂ and (b) S₂, in the Irish Sea averaged over the year 2015. The black solid lines represent the phases of the constituents (Horrillo-Caraballo et al., 2021).

A.4. Sediment distribution

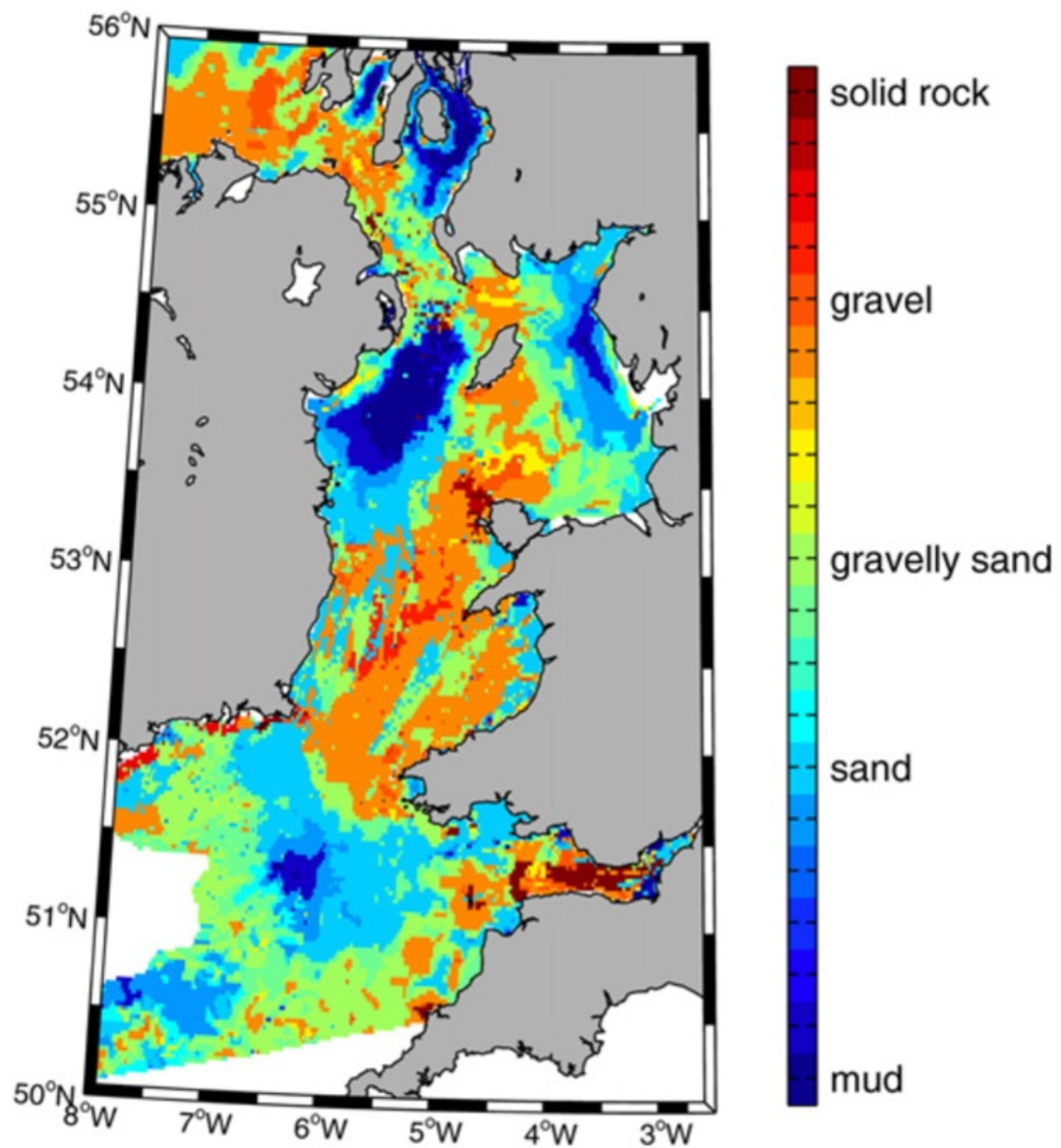


Figure A.4: Seabed sediment distribution using the Folk (1954) triangle (Ward et al., 2015).

A.5. Peak bed shear stresses

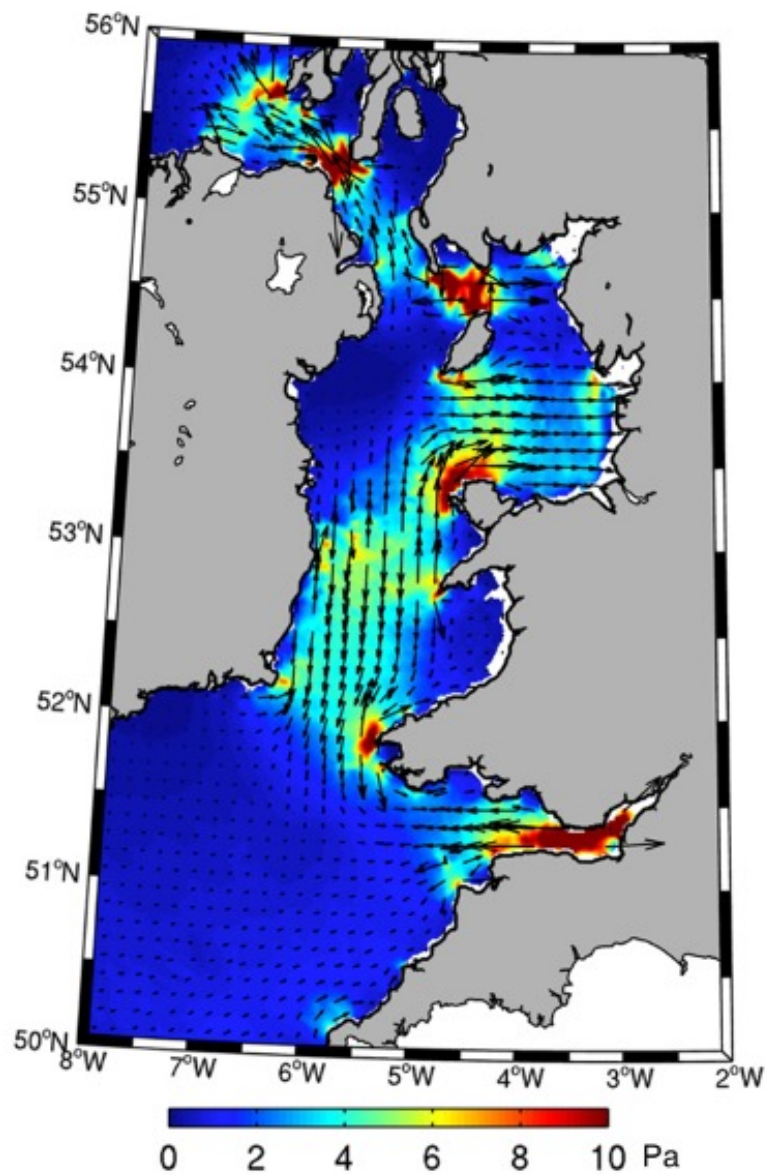


Figure A.5: Modelled (M2 + S2) tidally-induced peak bed shear stress in the Irish Sea with direction and magnitude (Ward et al., 2015).

B

AmSedIS data

B.1. Area 3-3

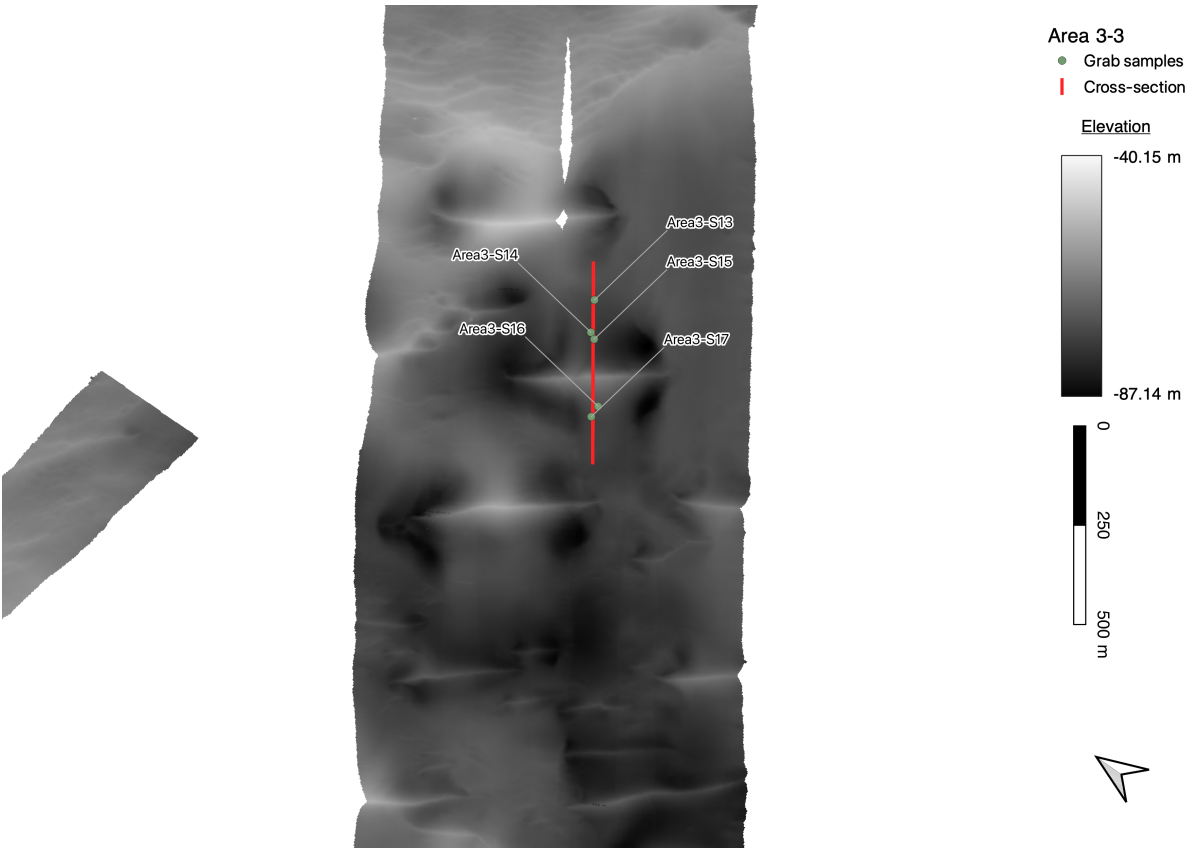


Figure B.1: Plan view of the bathymetry at area 3 with the locations at which grab samples were taken during the AmSedIS project, April 2012. Red line indicates a cross-section of the bathymetry shown on the next page.

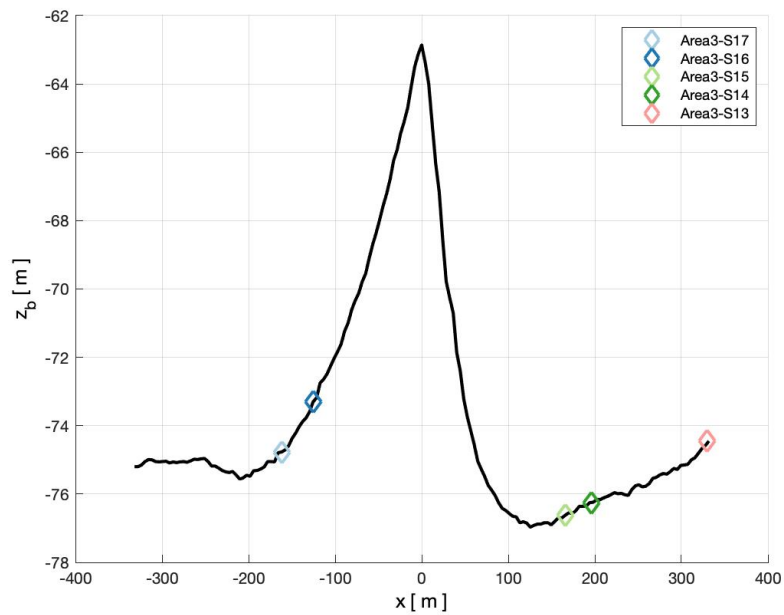


Figure B.2: Cross-section of a trochoidal sediment wave bathymetry at area 3 with grab sample locations during the AmSedIS project, April 2012. Note that the location of the grab samples are variable in y -direction.

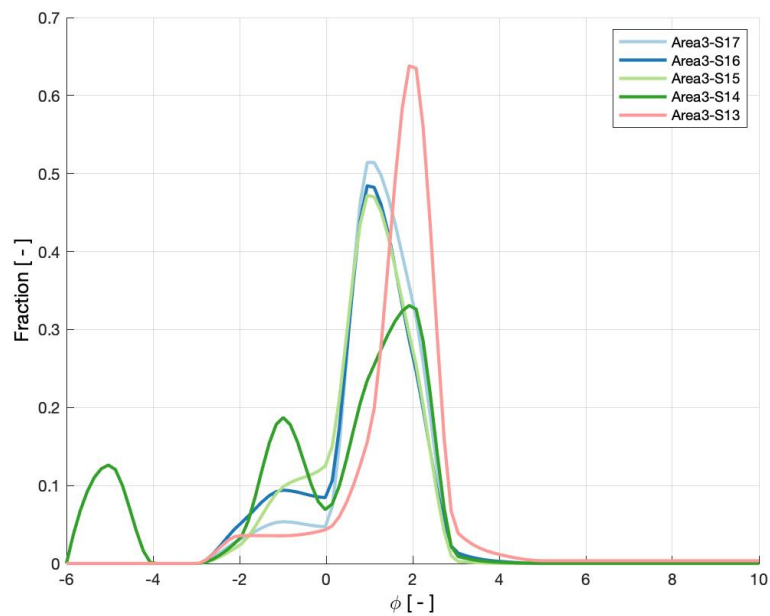


Figure B.3: Grain size distributions of multiple grab samples; mass fraction against the logarithmic phi scale (Krumbein, 1934). Grab sample locations were taken along a trochoidal sediment wave at area 3 during the AmSedIS project, April 2012. Note that the grain size fractions for each sediment type (Wentworth, 1922) are determined through sieving or laser granulometer of the sample particles. A line is fitted between these measurements.

B.2. Area 4N

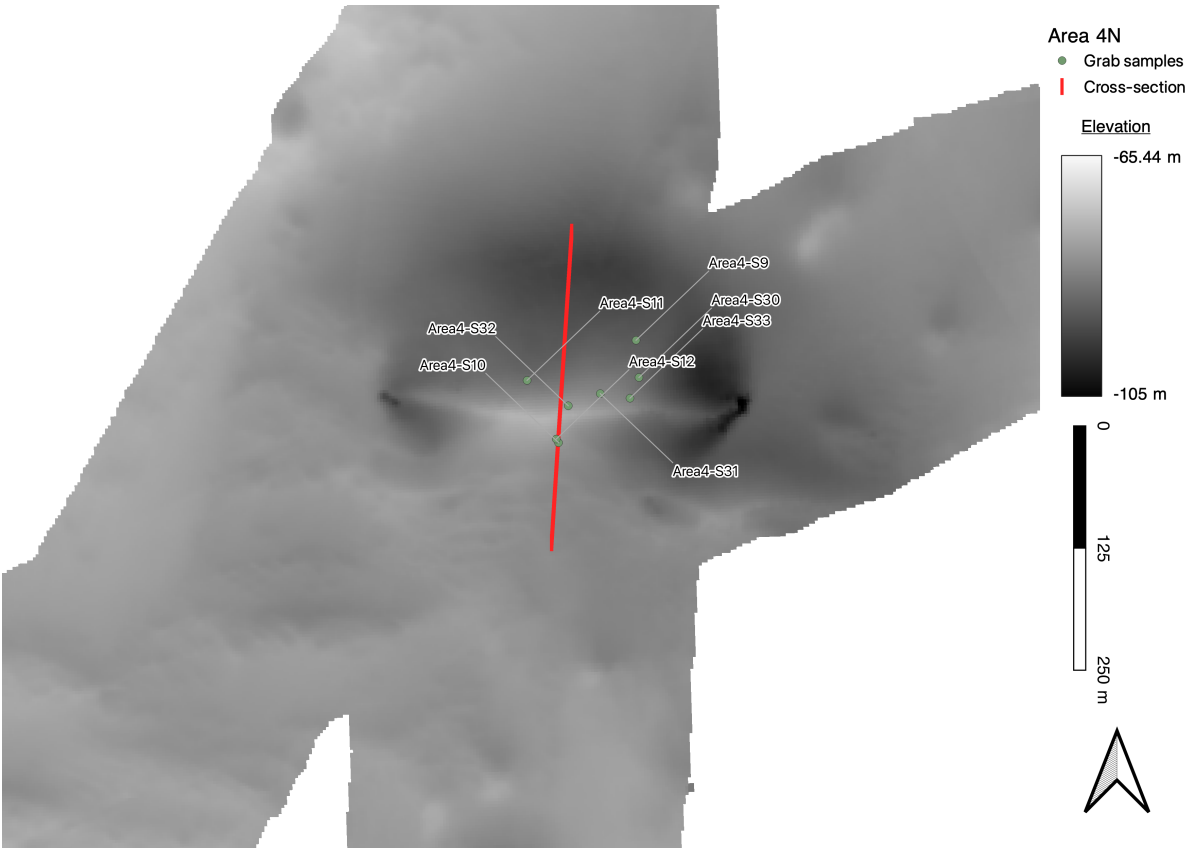


Figure B.4: Plan view of the bathymetry in the north of area 4 with the locations at which grab samples were taken during the AmSedIS project, April 2012. Red line indicates a cross-section of the bathymetry shown on the next page.

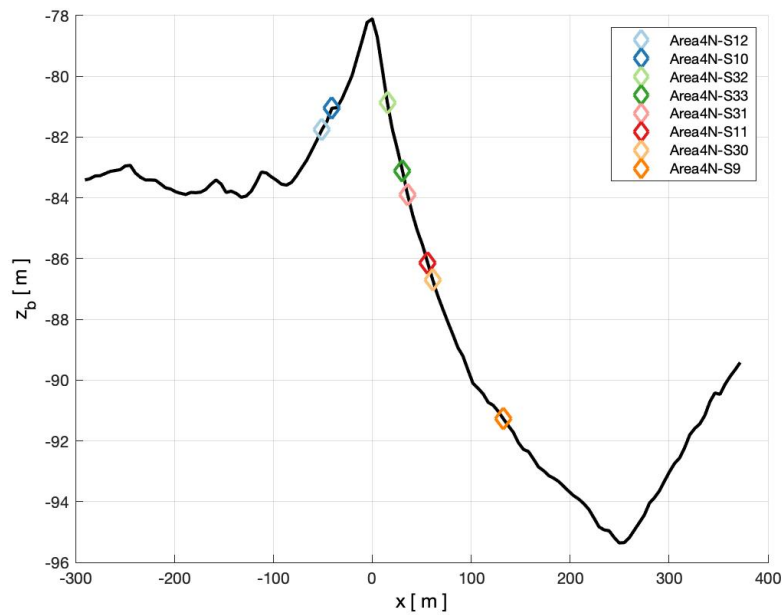


Figure B.5: Cross-section of a trochoidal sediment wave bathymetry in the north of area 4 with grab sample locations during the AmSedIS project, April 2012. Note that the location of the grab samples are variable in y -direction.

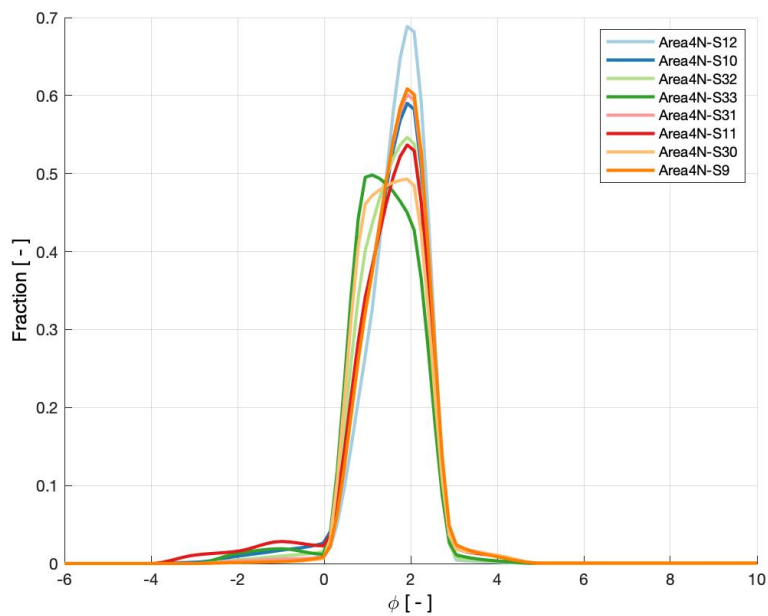


Figure B.6: Grain size distributions of multiple grab samples; mass fraction against the logarithmic phi scale (Krumbein, 1934). Grab sample locations were taken along a trochoidal sediment wave in the north of area 4 during the AmSedIS project, April 2012. Note that the grain size fractions for each sediment type (Wentworth, 1922) are determined through sieving or laser granulometer of the sample particles. A line is fitted between these measurements.

B.3. Area 9

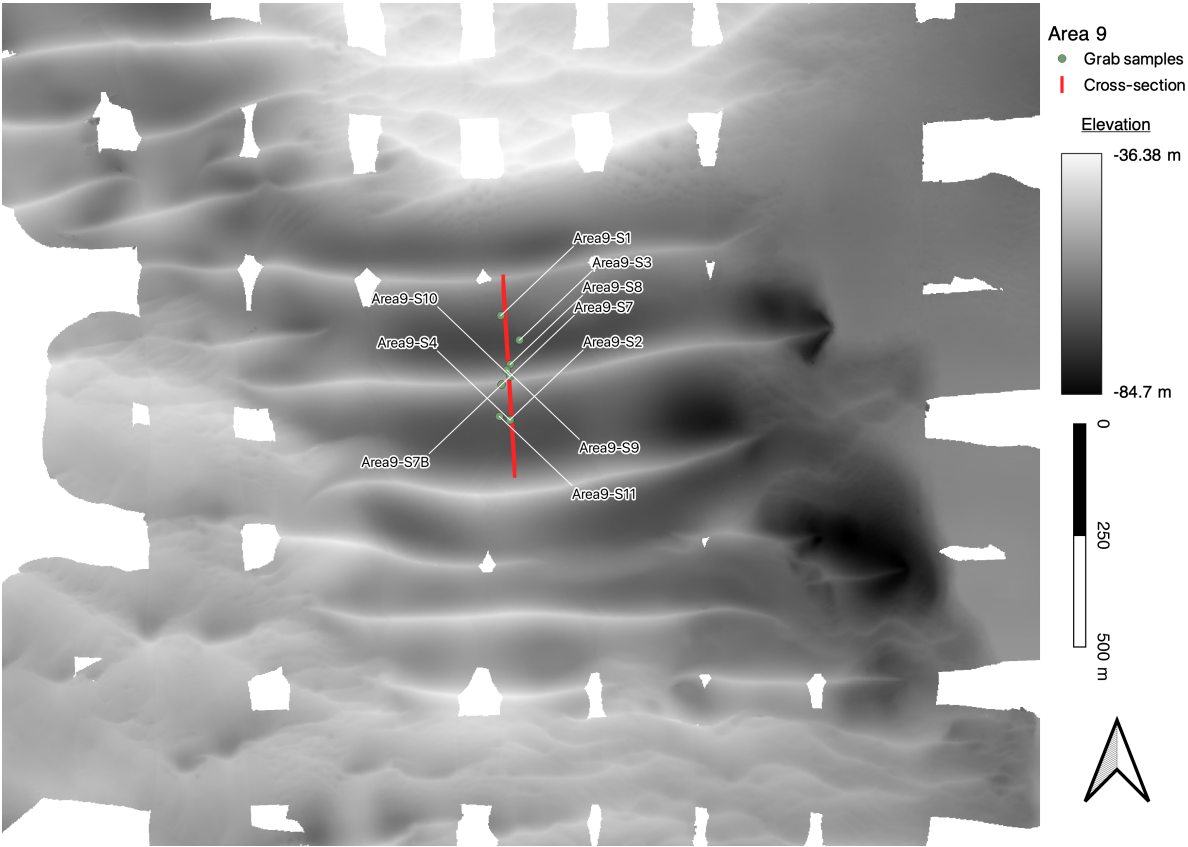


Figure B.7: Plan view of the bathymetry at area 9 with the locations at which grab samples were taken during the AmSedIS project, April 2012. Red line indicates a cross-section of the bathymetry shown on the next page.

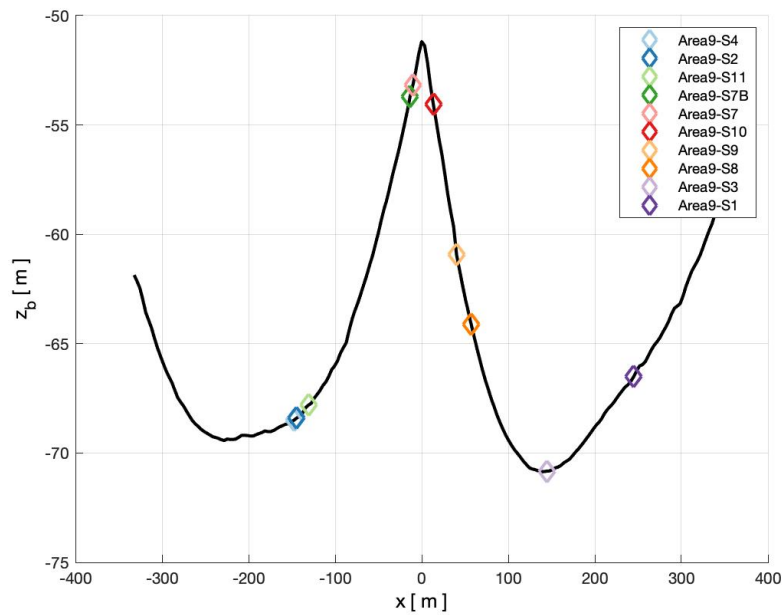


Figure B.8: Cross-section of a trochoidal sediment wave bathymetry at area 9 with grab sample locations during the AmSedIS project, April 2012. Note that the location of the grab samples are variable in y -direction.

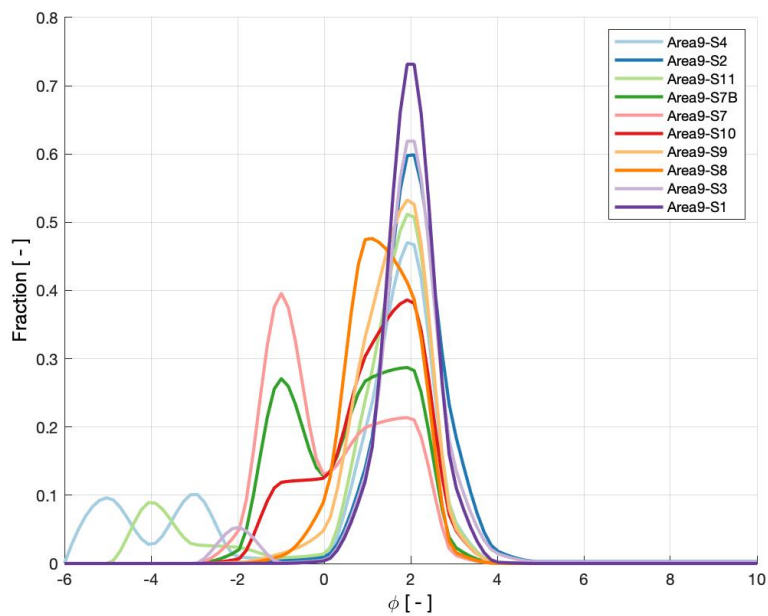


Figure B.9: Grain size distributions of multiple grab samples; mass fraction against the logarithmic phi scale (Krumbein, 1934). Grab sample locations were taken along a trochoidal sediment wave in area 9 during the AmSedIS project, April 2012. Note that the grain size fractions for each sediment type (Wentworth, 1922) are determined through sieving or laser granulometer of the sample particles. A line is fitted between these measurements.

B.4. Area 12M

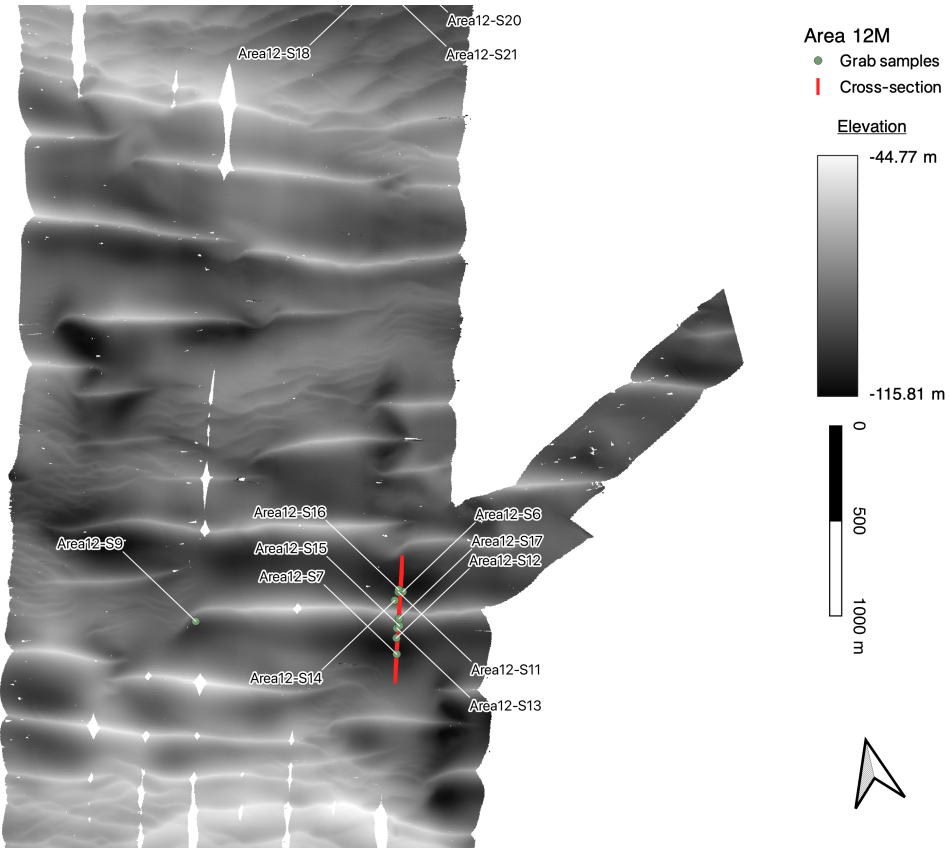


Figure B.10: Plan view of the bathymetry in the center of area 12 with the locations at which grab samples were taken during the AmSedIS project, April 2012. Red line indicates a cross-section of the bathymetry shown on the next page.

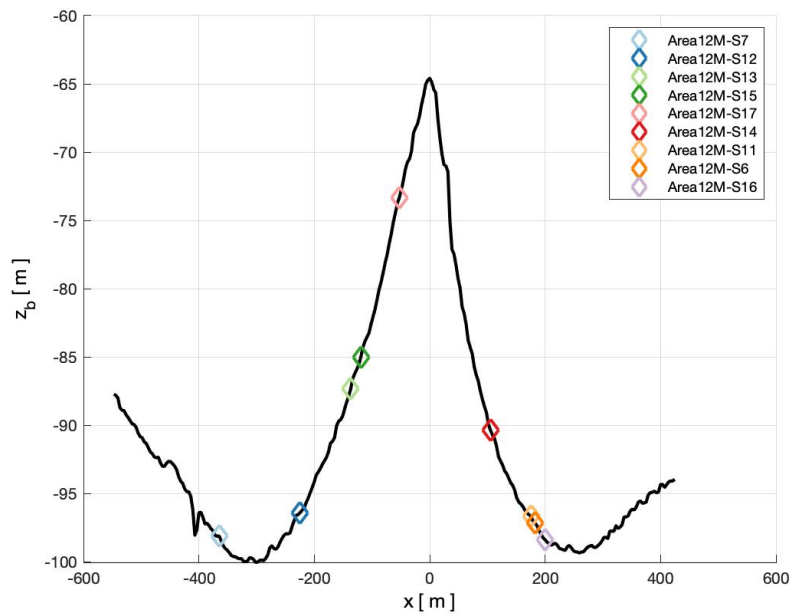


Figure B.11: Cross-section of a trochoidal sediment wave bathymetry in the center of area 12 with grab sample locations during the AmSediS project, April 2012. Note that the location of the grab samples are variable in y -direction.

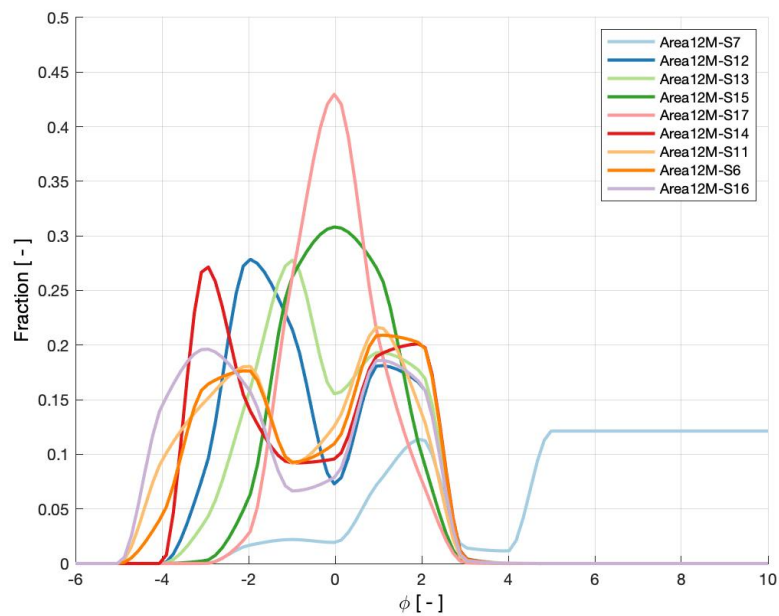


Figure B.12: Grain size distributions of multiple grab samples; mass fraction against the logarithmic phi scale (Krumbein, 1934). Grab sample locations were taken along a trochoidal sediment wave in the center of area 12 during the AmSediS project, April 2012. Note that the grain size fractions for each sediment type (Wentworth, 1922) are determined through sieving or laser granulometer of the sample particles. A line is fitted between these measurements.

B.5. Area 13N

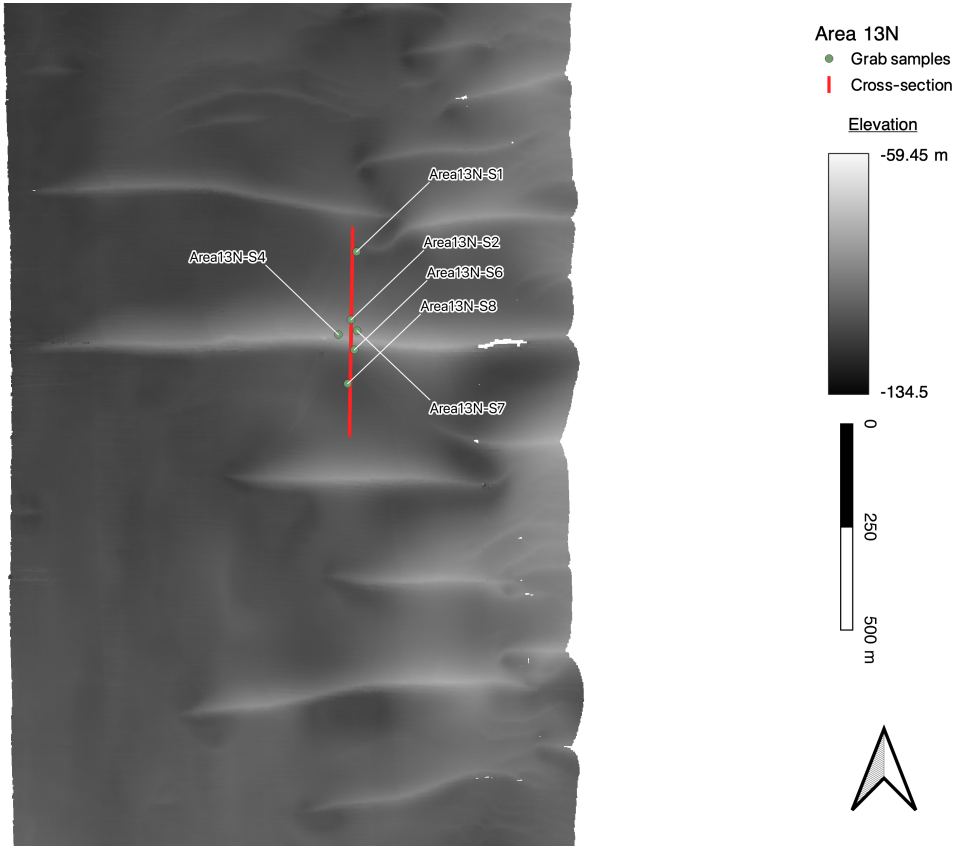


Figure B.13: Plan view of the bathymetry in the north of area 13 with the locations at which grab samples were taken during the AmSedIS project, April 2012. Red line indicates a cross-section of the bathymetry shown on the next page.

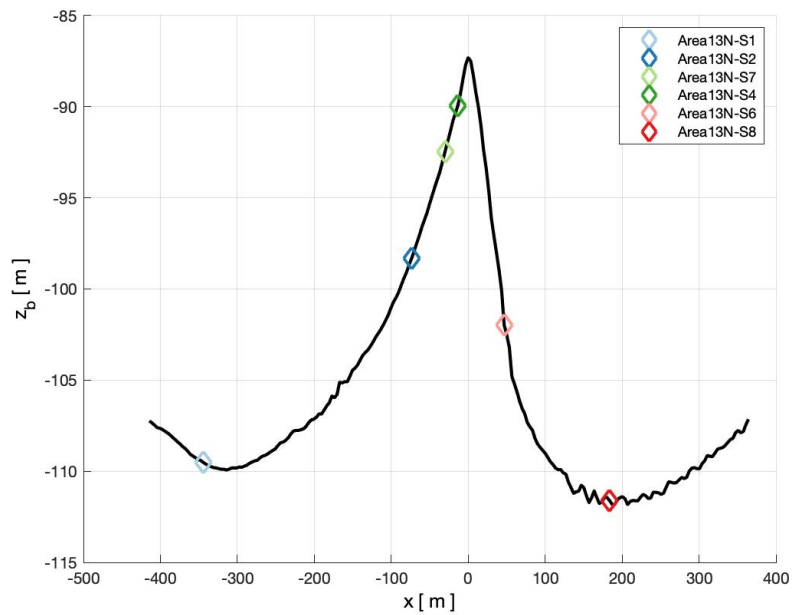


Figure B.14: Cross-section of a trochoidal sediment wave bathymetry in the north of area 13 with grab sample locations during the AmSediS project, April 2012. Note that the location of the grab samples are variable in y -direction.

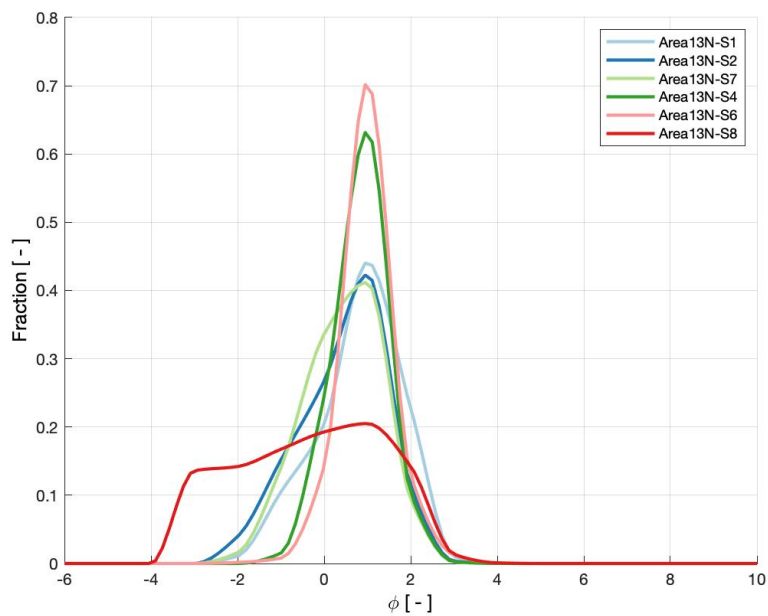


Figure B.15: Grain size distributions of multiple grab samples; mass fraction against the logarithmic phi scale (Krumbein, 1934). Grab sample locations were taken along a trochoidal sediment wave in the north of area 13 during the AmSediS project, April 2012. Note that the grain size fractions for each sediment type (Wentworth, 1922) are determined through sieving or laser granulometer of the sample particles. A line is fitted between these measurements.

B.6. Area 14E

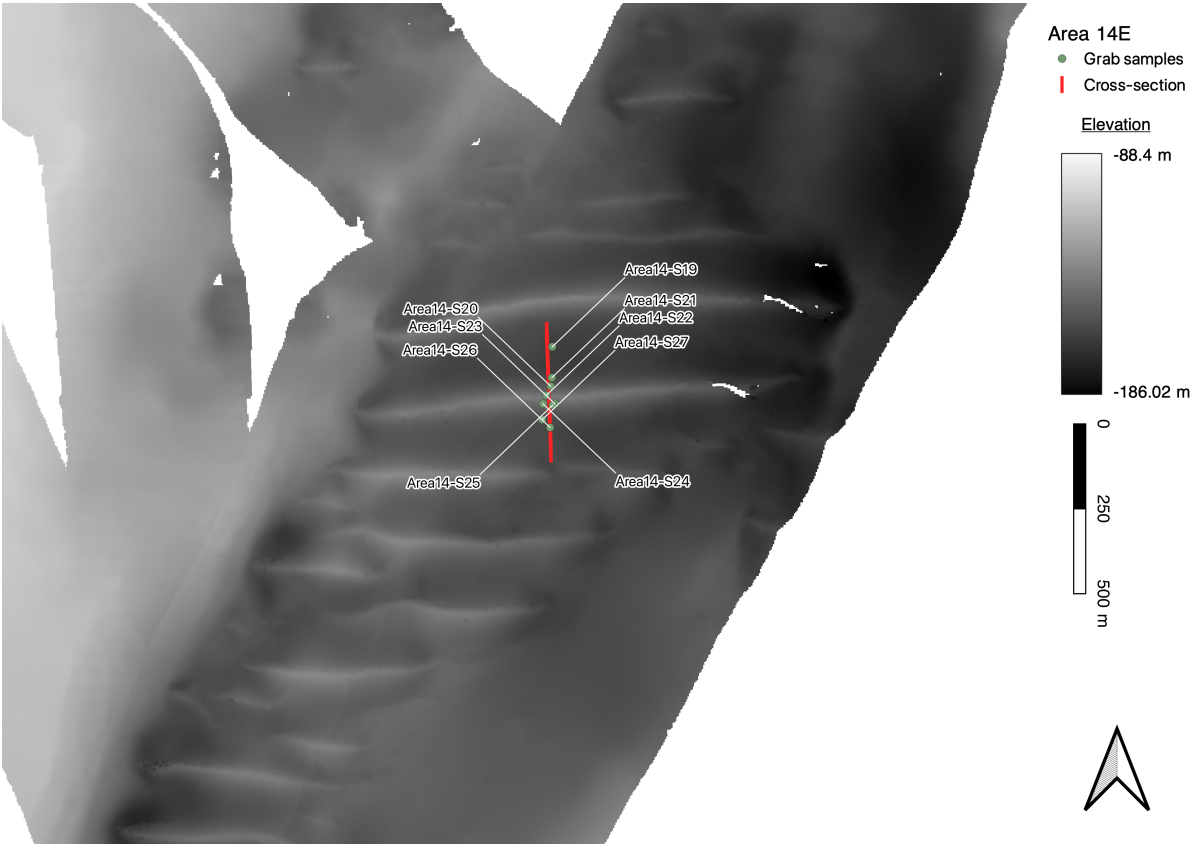


Figure B.16: Plan view of the bathymetry in the east of area 14 with the locations at which grab samples were taken during the AmSedIS project, April 2012. Red line indicates a cross-section of the bathymetry shown on the next page.

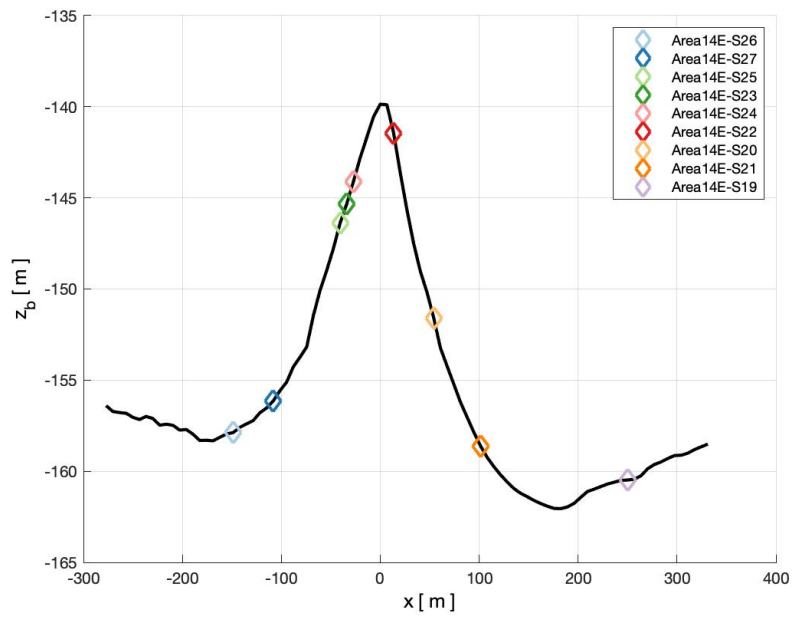


Figure B.17: Cross-section of a trochoidal sediment wave bathymetry in the east of area 14 with grab sample locations during the AmSedIS project, April 2012. Note that the location of the grab samples are variable in y -direction.

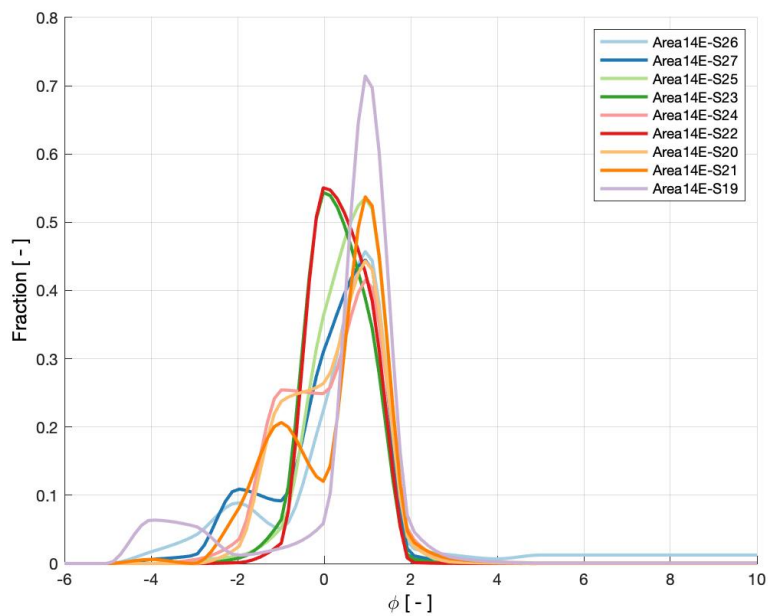


Figure B.18: Grain size distributions of multiple grab samples; mass fraction against the logarithmic phi scale (Krumbein, 1934). Grab sample locations were taken along a trochoidal sediment wave in the east of area 14 during the AmSedIS project, April 2012. Note that the grain size fractions for each sediment type (Wentworth, 1922) are determined through sieving or laser granulometer of the sample particles. A line is fitted between these measurements.

B.7. Area 14W

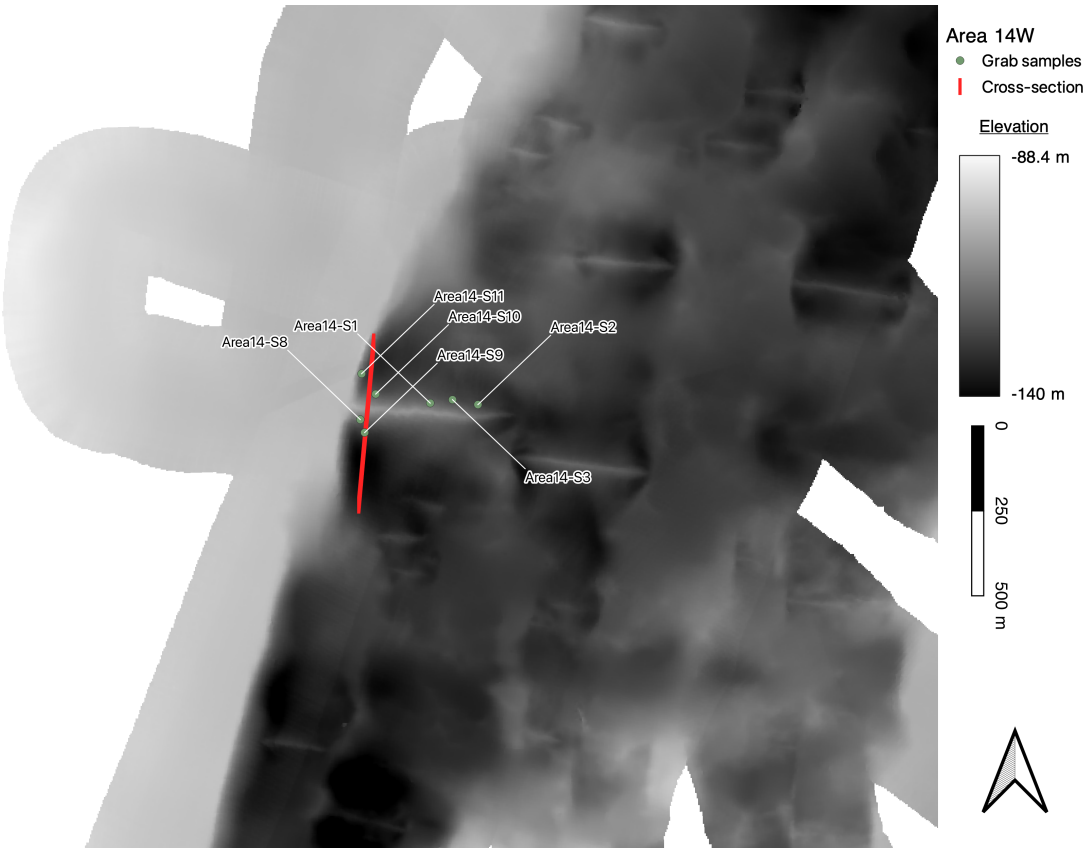


Figure B.19: Plan view of the bathymetry in the west of area 14 with the locations at which grab samples were taken during the AmSedIS project, April 2012. Red line indicates a cross-section of the bathymetry shown on the next page.

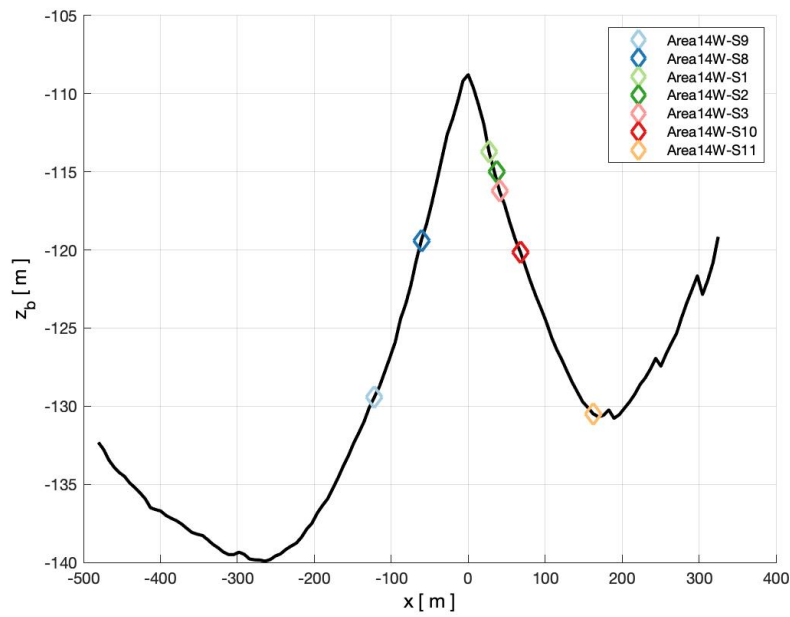


Figure B.20: Cross-section of a trochoidal sediment wave bathymetry in the west of area 14 with grab sample locations during the AmSedIS project, April 2012. Note that the location of the grab samples are variable in y -direction.

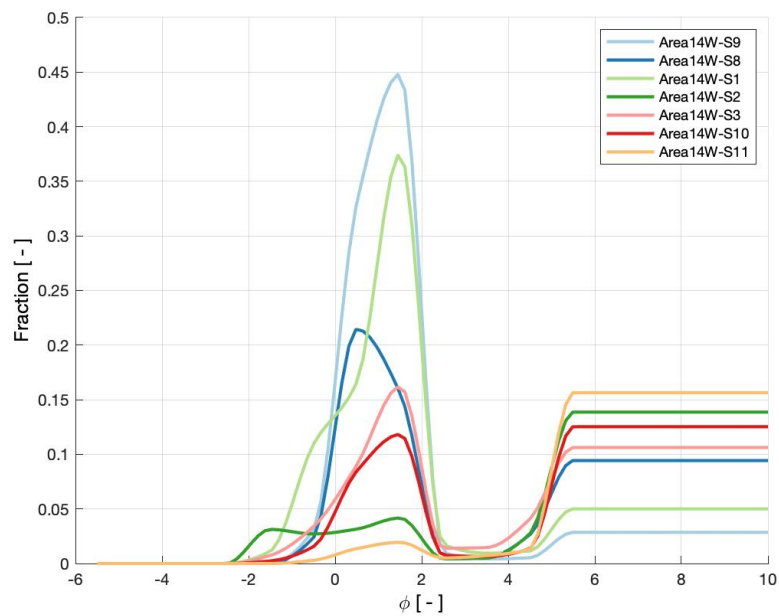


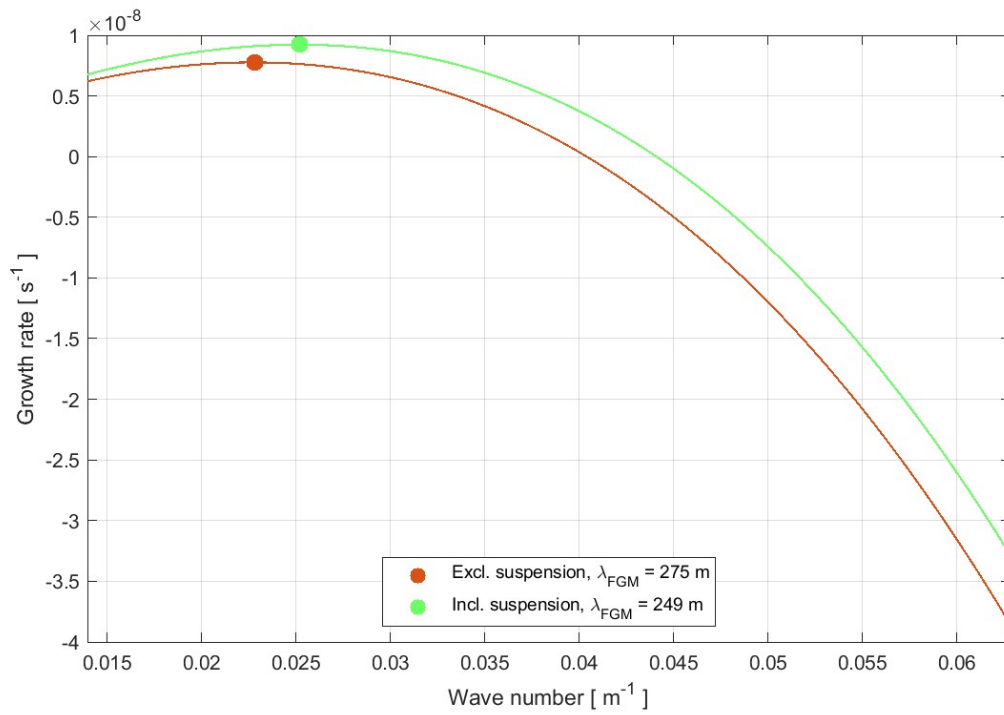
Figure B.21: Grain size distributions of multiple grab samples; mass fraction against the logarithmic phi scale (Krumbein, 1934). Grab sample locations were taken along a trochoidal sediment wave in the west of area 14 during the AmSedIS project, April 2012. Note that the grain size fractions for each sediment type (Wentworth, 1922) are determined through sieving or laser granulometer of the sample particles. A line is fitted between these measurements.

C

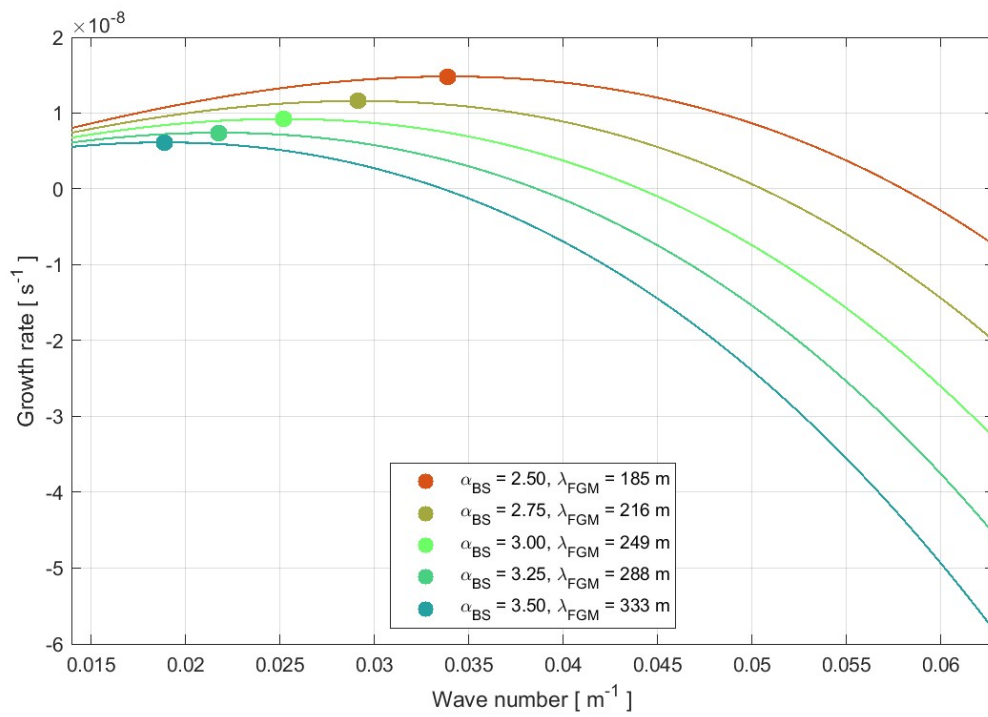
Fastest growing mode

C.1. Case I

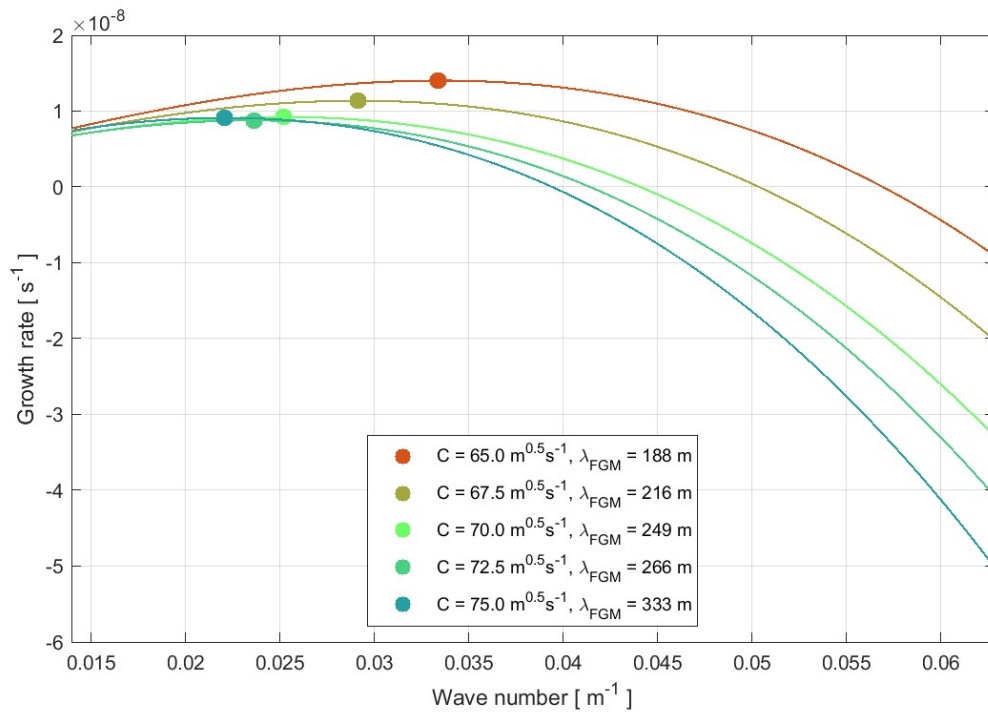
(a) Suspended load transport



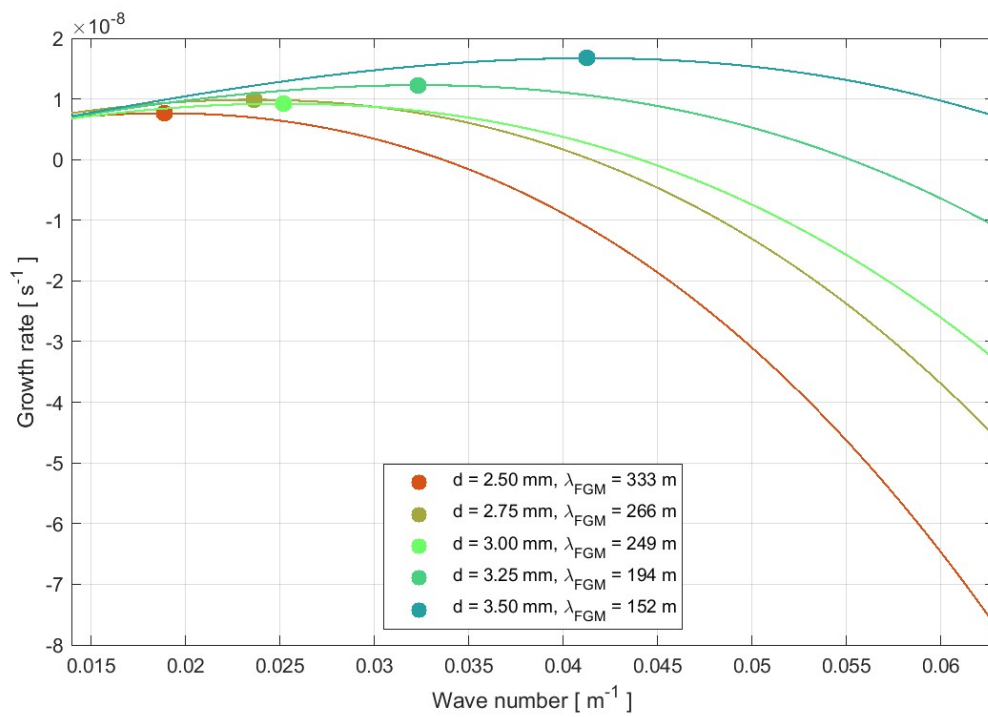
(b) Slope effect tuning parameter



(c) Chezy roughness



(d) Grain size



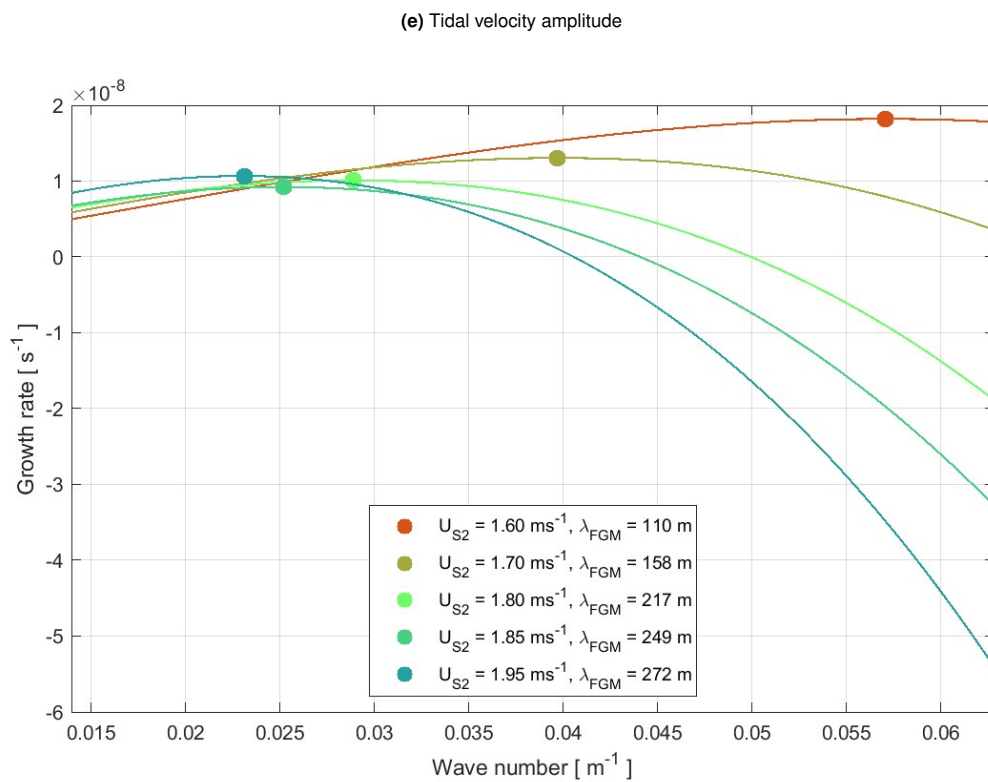


Figure C.1: Growth rate γ (s^{-1}) against wave number k ($= 2\pi/\lambda$) (m^{-1}) for variable model parameters, i.e. (a) ex- and including suspended load transport, (b) slope effect tuning parameter, (c) Chezy roughness, (d) grain size and (e) tidal velocity amplitude. The circles indicate the growth rates corresponding to the fastest growing mode λ_{FGM} . The x-axis corresponds to $\lambda = [600, 100]$. Note that a line is fitted between growth rates that belong to $\lambda = 100, 250, 400, 600$ m.

C.2. Case II

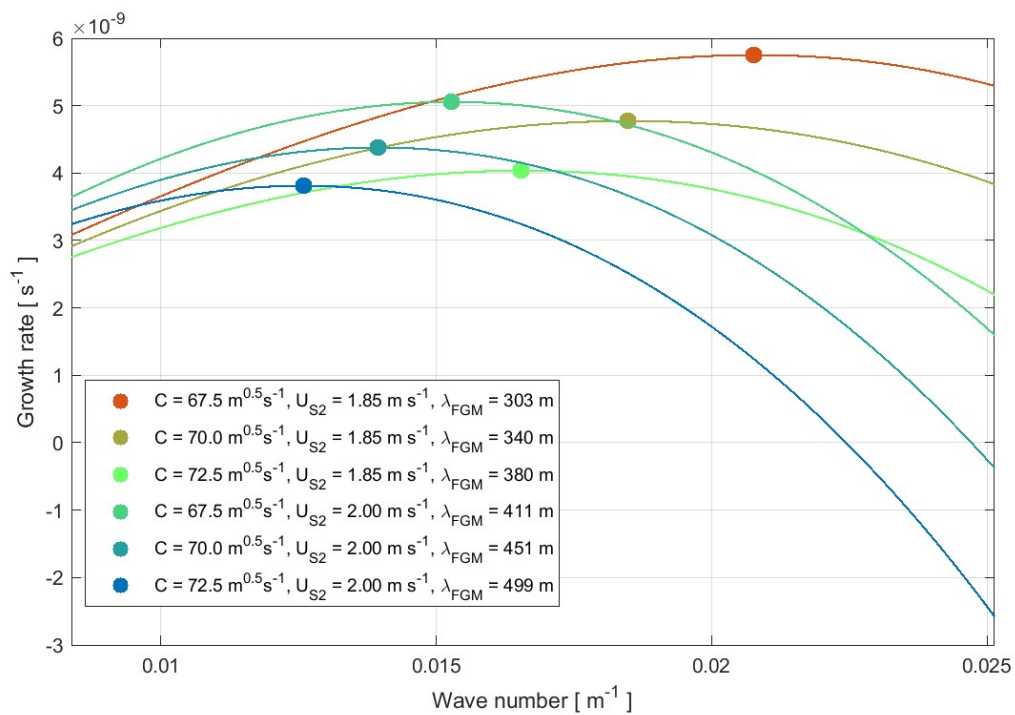


Figure C.2: Growth rate γ (s^{-1}) against wave number k ($= 2\pi/\lambda$) (m^{-1}) for different combinations of the process parameters Chezy roughness value C and tidal velocity amplitude U_{S2} . The circles indicate the growth rates corresponding to the fastest growing mode λ_{FGM} . The x-axis corresponds to $\lambda = [750, 250]$. Note that a line is fitted between growth rates that belong to $\lambda = 250, 400, 600, 750$ m.

D

Circulation cells

D.1. Suspended load transport

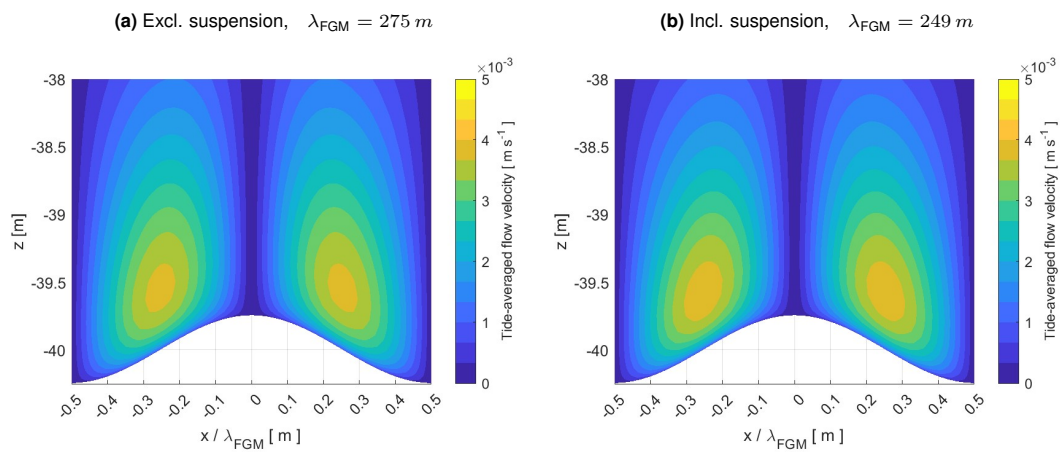


Figure D.1: Normalised circulation cells excluding and including suspended load transport with its corresponding fastest growing mode λ_{FGM}

D.2. Slope effect tuning parameter

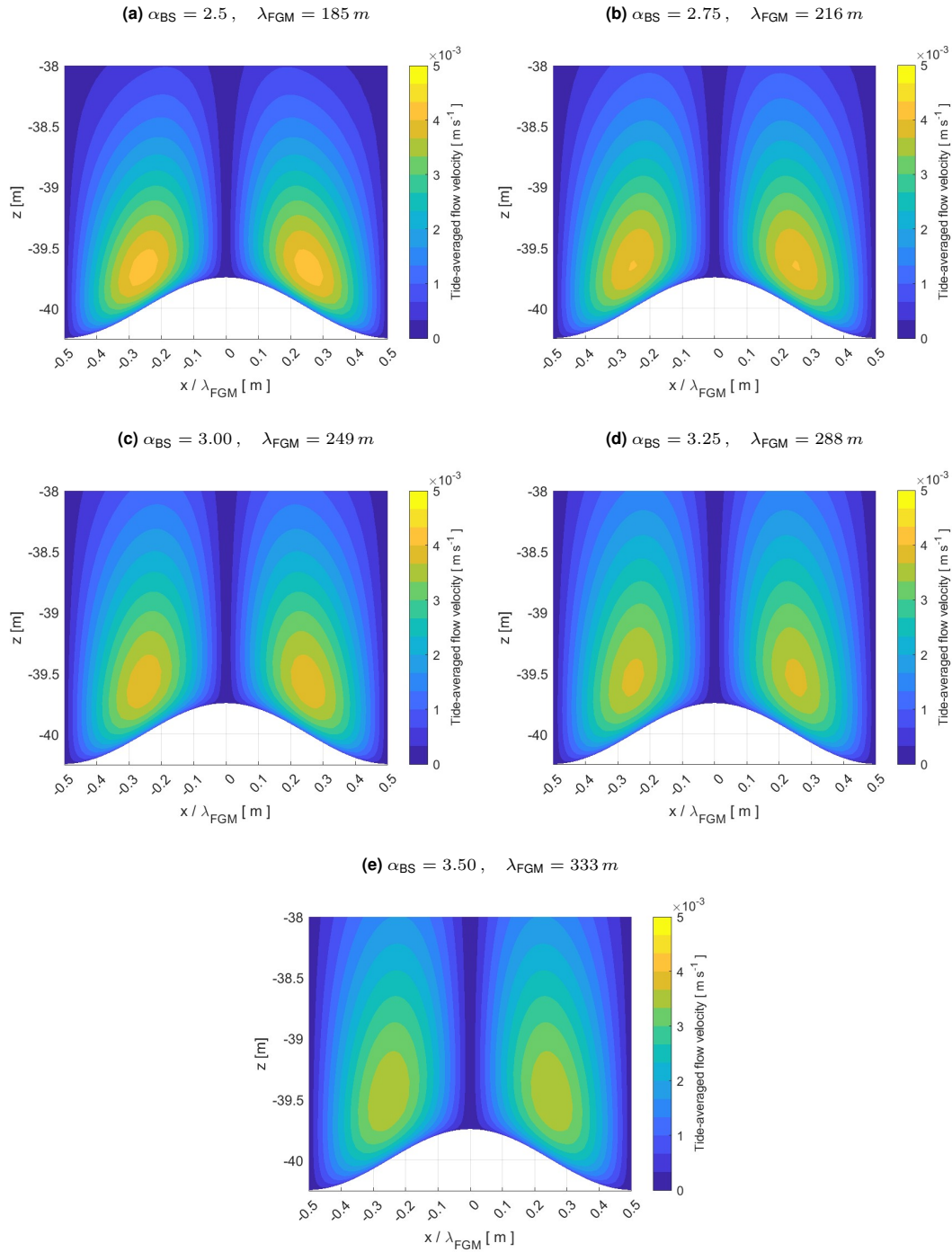


Figure D.2: Normalised circulation cells for a varying slope effect tuning parameter α_{BS} with its corresponding fastest growing mode λ_{FGM}

D.3. Chezy roughness

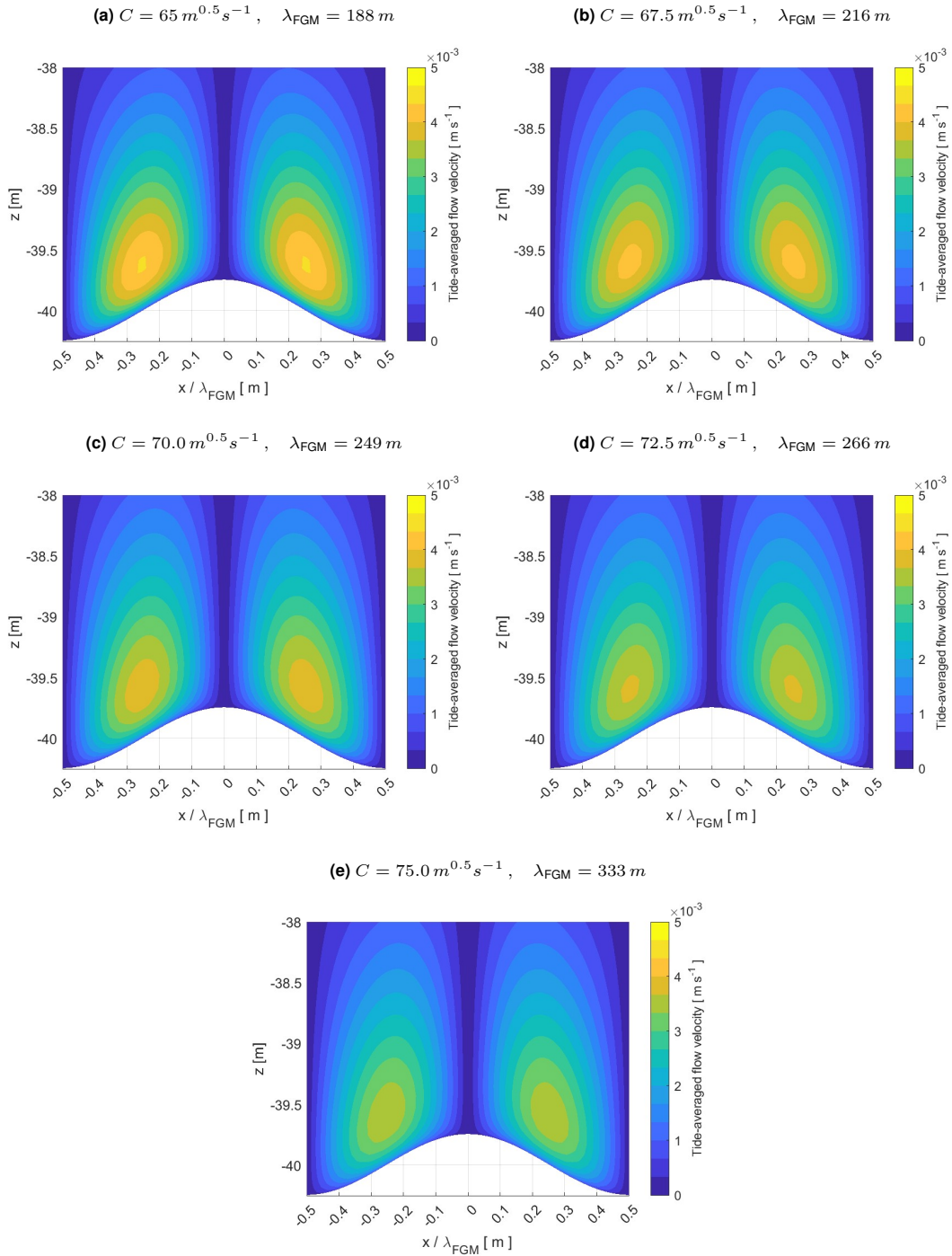


Figure D.3: Normalised circulation cells for a varying Chezy roughness C with its corresponding fastest growing mode λ_{FGM}

D.4. Grain size

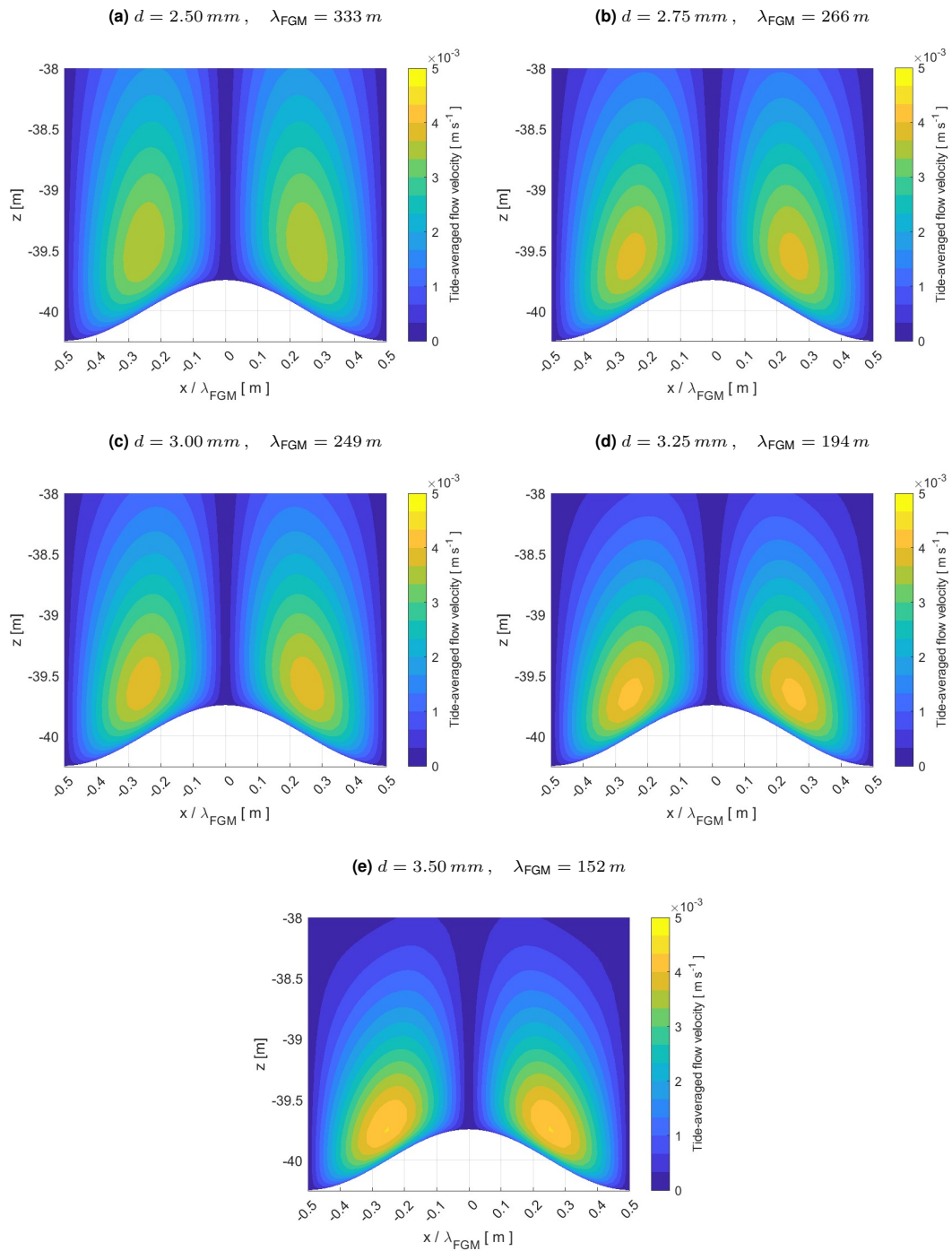


Figure D.4: Normalised circulation cells for a varying median diameter d with its corresponding fastest growing mode λ_{FGM}

D.5. Tidal velocity amplitude

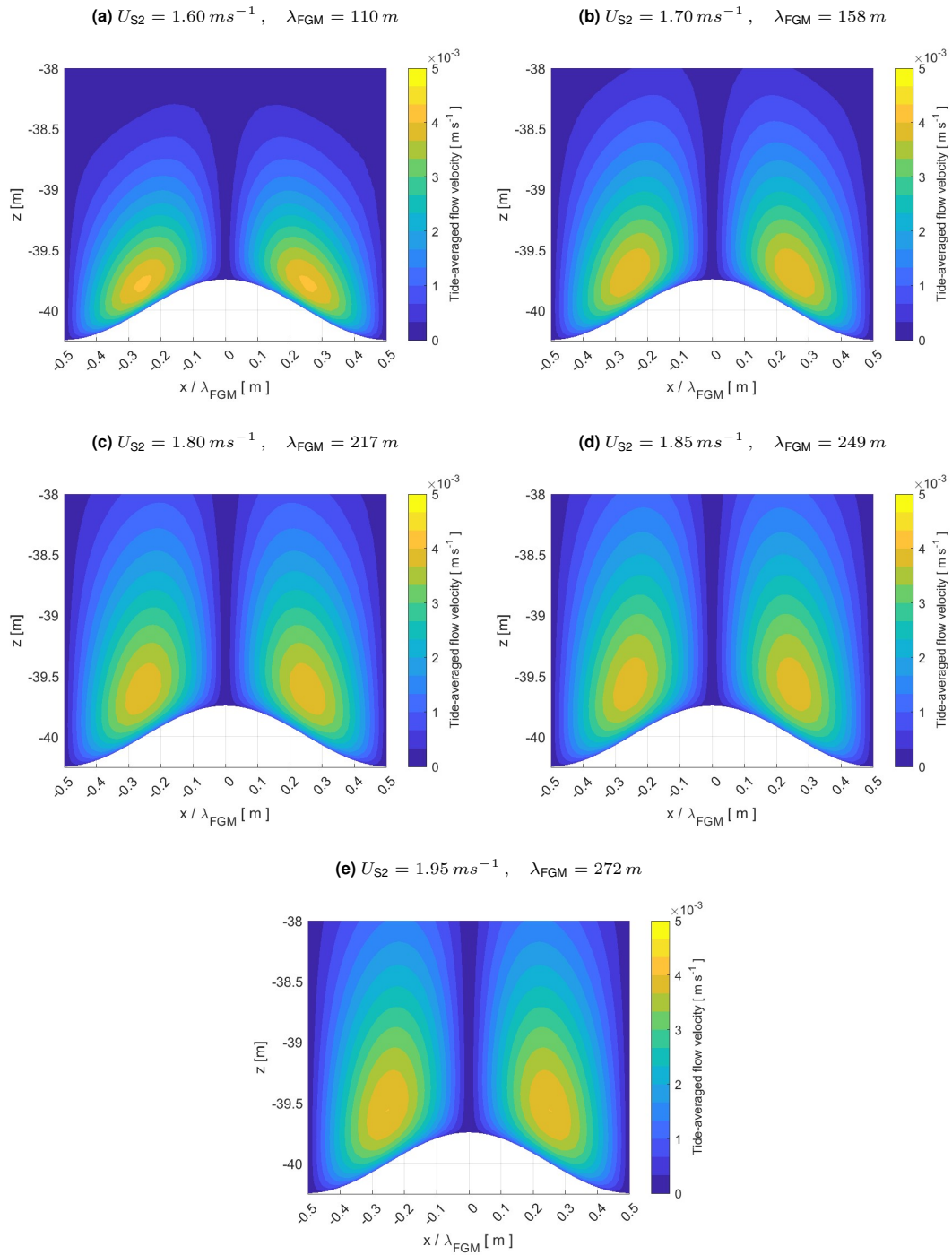


Figure D.5: Normalised circulation cells for a varying tidal velocity amplitude U_{S2} with its corresponding fastest growing mode λ_{FGM}

E

Sediment transport

E.1. Suspended load transport

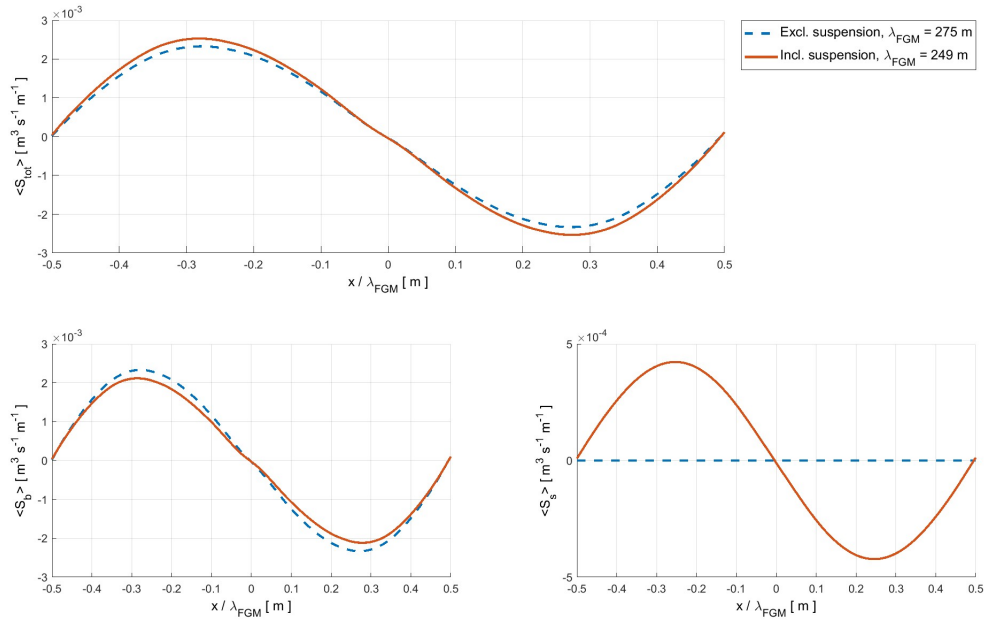


Figure E.1: Normalised tidally-averaged total $\langle S_{tot} \rangle$, bed load $\langle S_b \rangle$ and suspended load $\langle S_s \rangle$ sediment transport ex- and including suspended load transport with its corresponding fastest growing mode λ_{FGM}

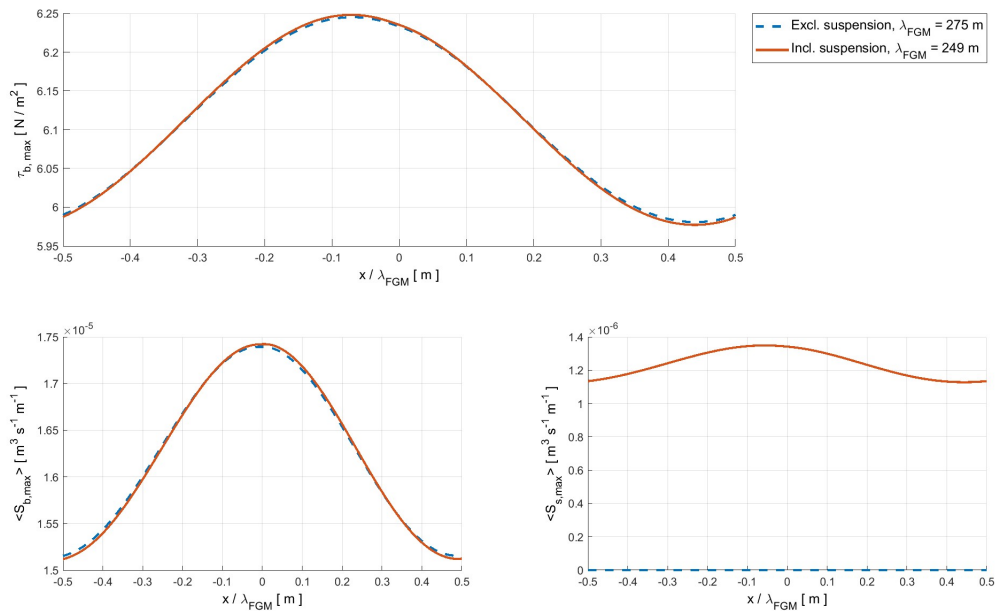


Figure E.2: Normalised maximum bed shear stress $\langle \tau_{b,max} \rangle$, bed load $\langle S_{b,max} \rangle$ and suspended load $\langle S_{s,max} \rangle$ sediment transport ex- and including suspended load transport with its corresponding fastest growing mode λ_{FGM}

E.2. Slope effect tuning parameter

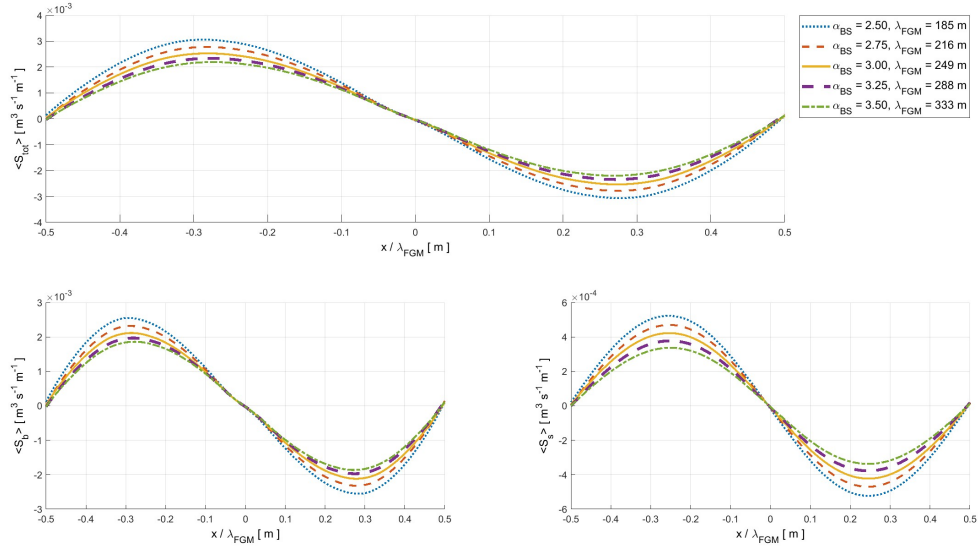


Figure E.3: Normalised tidally-averaged total $\langle S_{tot} \rangle$, bed load $\langle S_b \rangle$ and suspended load $\langle S_s \rangle$ sediment transport for a variable slope effect tuning parameter α_{BS} with its corresponding fastest growing mode λ_{FGM}

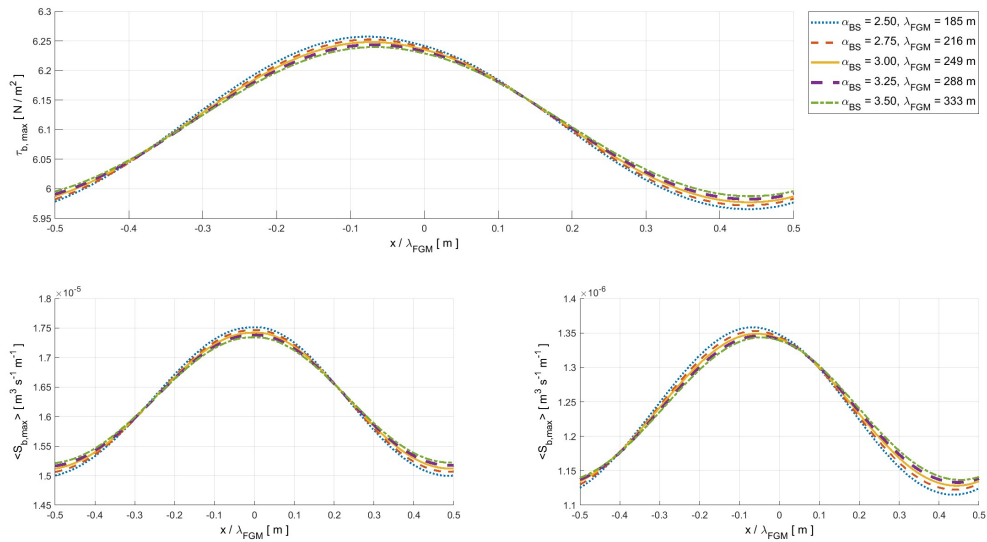


Figure E.4: Normalised maximum bed shear stress $\langle \tau_{b,max} \rangle$, bed load $\langle S_{b,max} \rangle$ and suspended load $\langle S_{s,max} \rangle$ sediment transport for a variable slope effect tuning parameter α_{BS} with its corresponding fastest growing mode λ_{FGM}

E.3. Chezy roughness

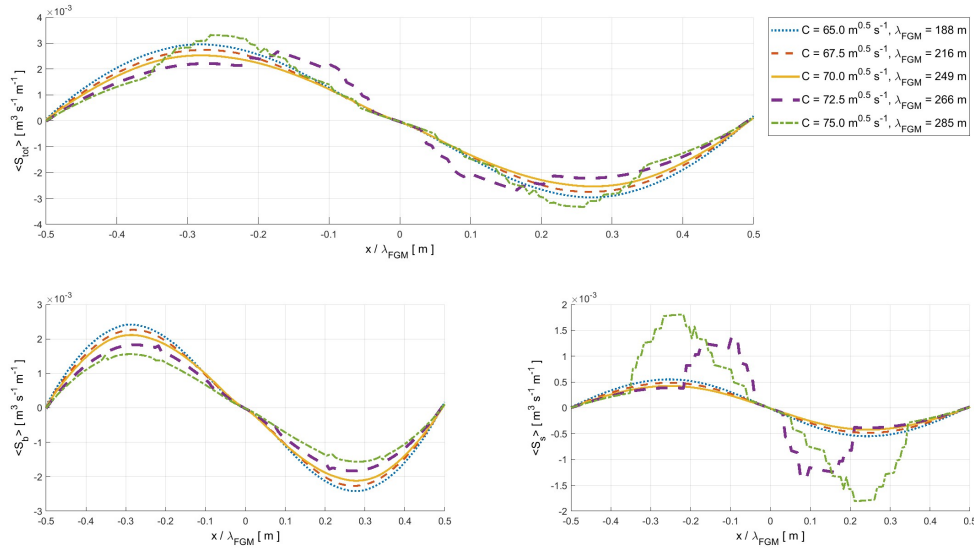


Figure E.5: Normalised tidally-averaged total $\langle S_{tot} \rangle$, bed load $\langle S_b \rangle$ and suspended load $\langle S_s \rangle$ sediment transport for a variable Chezy roughness C with its corresponding fastest growing mode λ_{FGM}

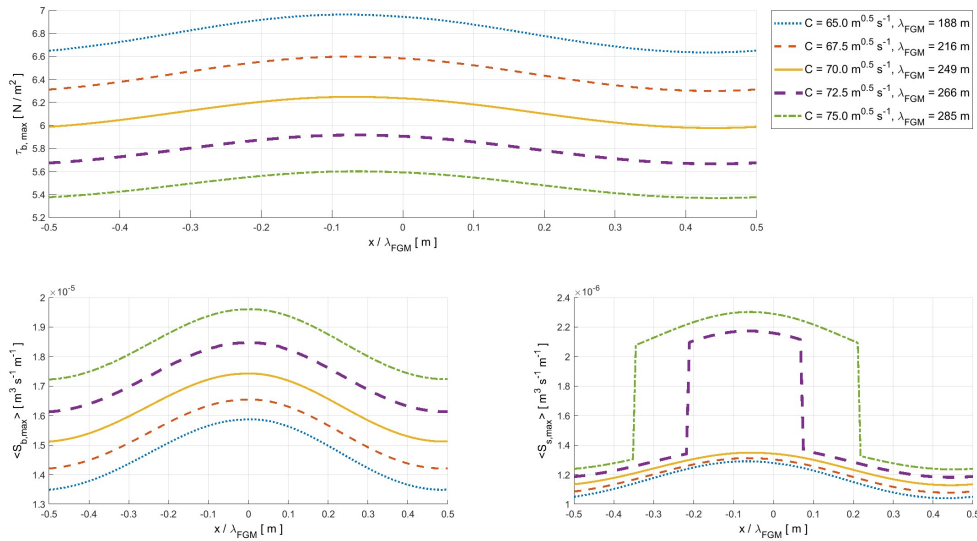


Figure E.6: Normalised maximum bed shear stress $\langle \tau_{b,max} \rangle$, bed load $\langle S_{b,max} \rangle$ and suspended load $\langle S_{s,max} \rangle$ sediment transport for a variable Chezy roughness C with its corresponding fastest growing mode λ_{FGM}

E.4. Grain size

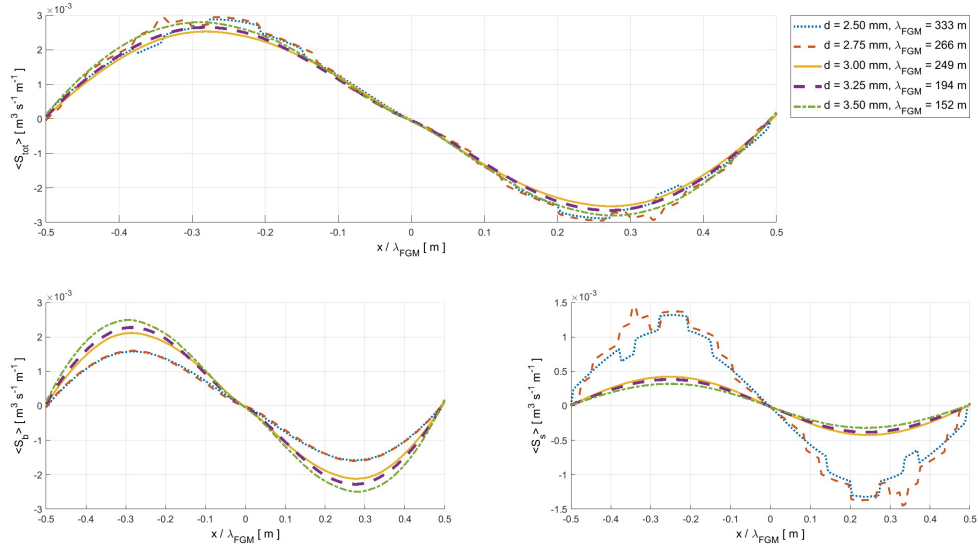


Figure E.7: Normalised tidally-averaged total $\langle S_{tot} \rangle$, bed load $\langle S_b \rangle$ and suspended load $\langle S_s \rangle$ sediment transport for a variable median diameter d with its corresponding fastest growing mode λ_{FGM}

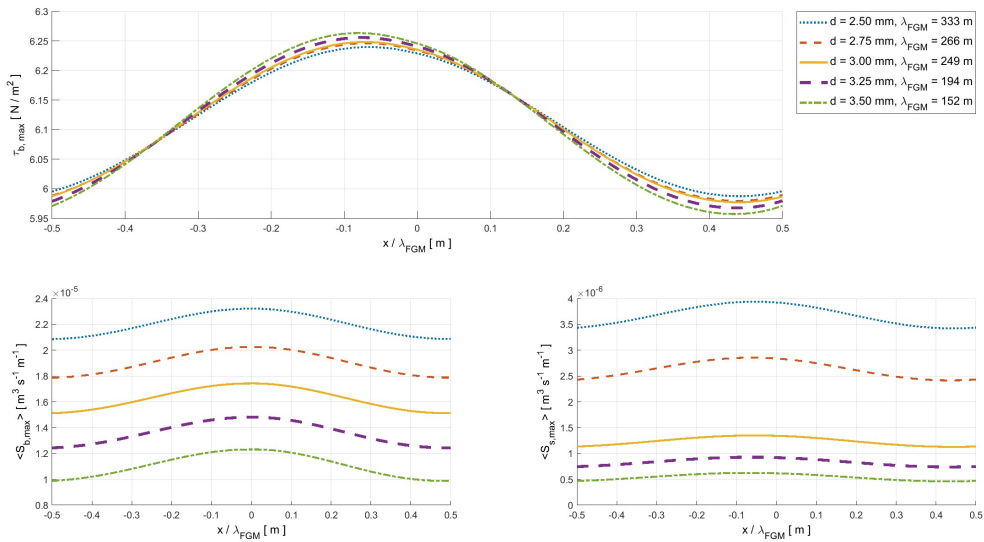


Figure E.8: Normalised maximum bed shear stress $\langle \tau_{b,max} \rangle$, bed load $\langle S_{b,max} \rangle$ and suspended load $\langle S_{s,max} \rangle$ sediment transport for a variable median diameter d with its corresponding fastest growing mode λ_{FGM}

E.5. Tidal velocity amplitude

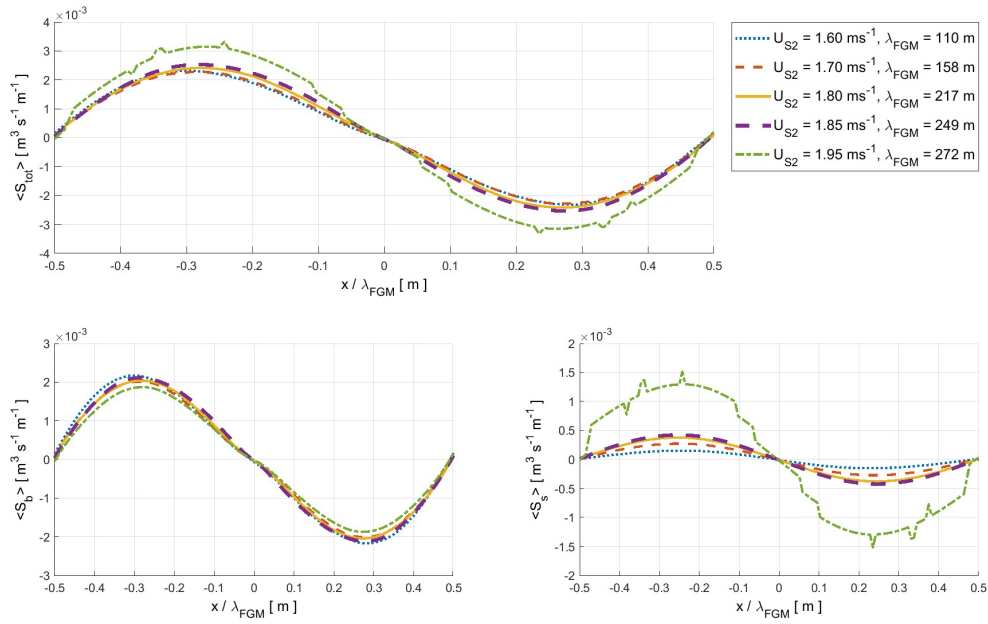


Figure E.9: Normalised tidally-averaged total $\langle S_{tot} \rangle$, bed load $\langle S_b \rangle$ and suspended load $\langle S_s \rangle$ sediment transport for a variable tidal velocity amplitude U_{S2} with its corresponding fastest growing mode λ_{FGM}

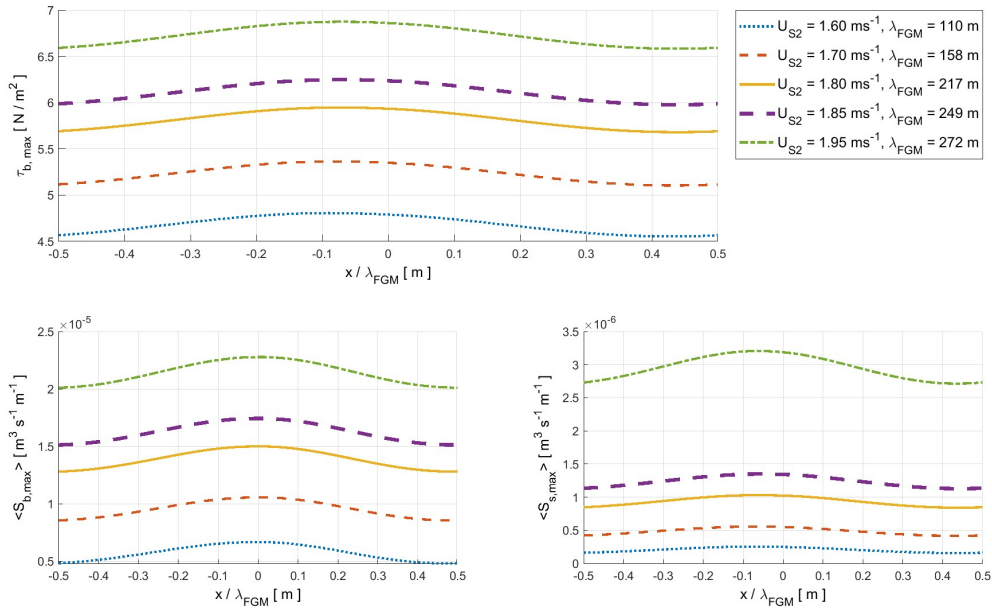


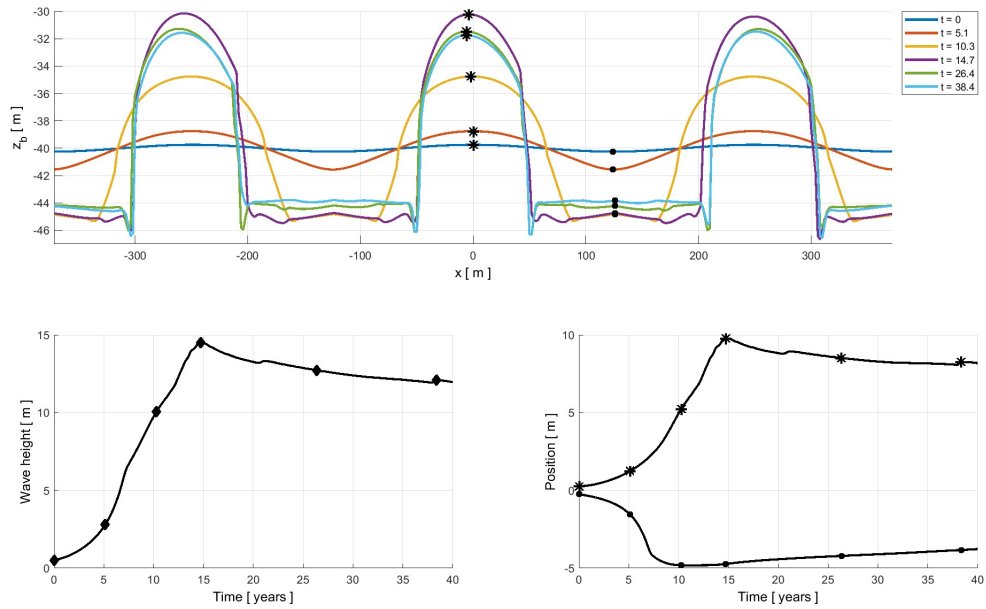
Figure E.10: Normalised maximum bed shear stress $\langle \tau_{b,max} \rangle$, bed load $\langle S_{b,max} \rangle$ and suspended load $\langle S_{s,max} \rangle$ sediment transport for a variable tidal velocity amplitude U_{S2} with its corresponding fastest growing mode λ_{FGM}

F

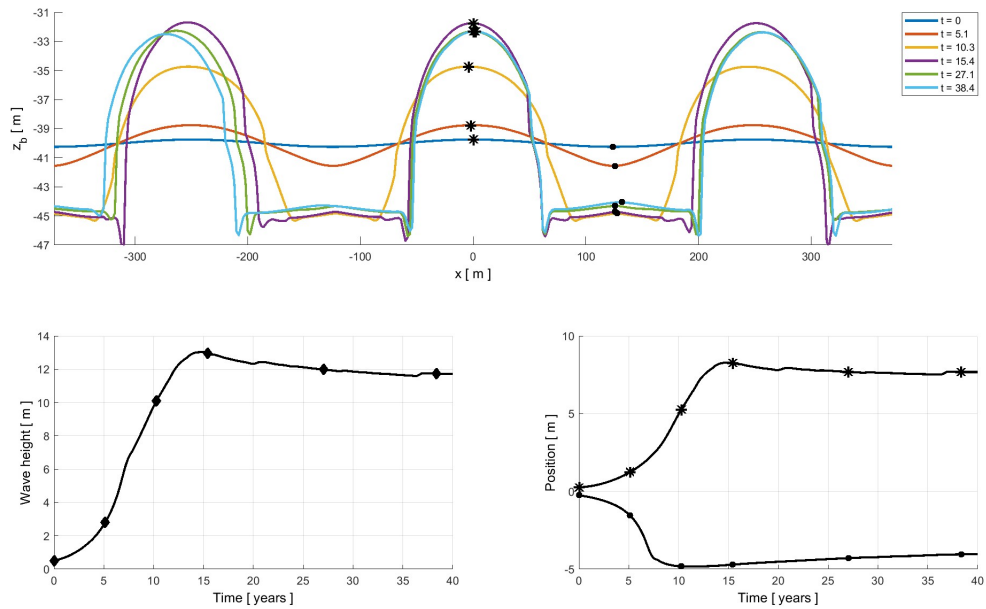
Bed development

F.1. Morphological acceleration factor

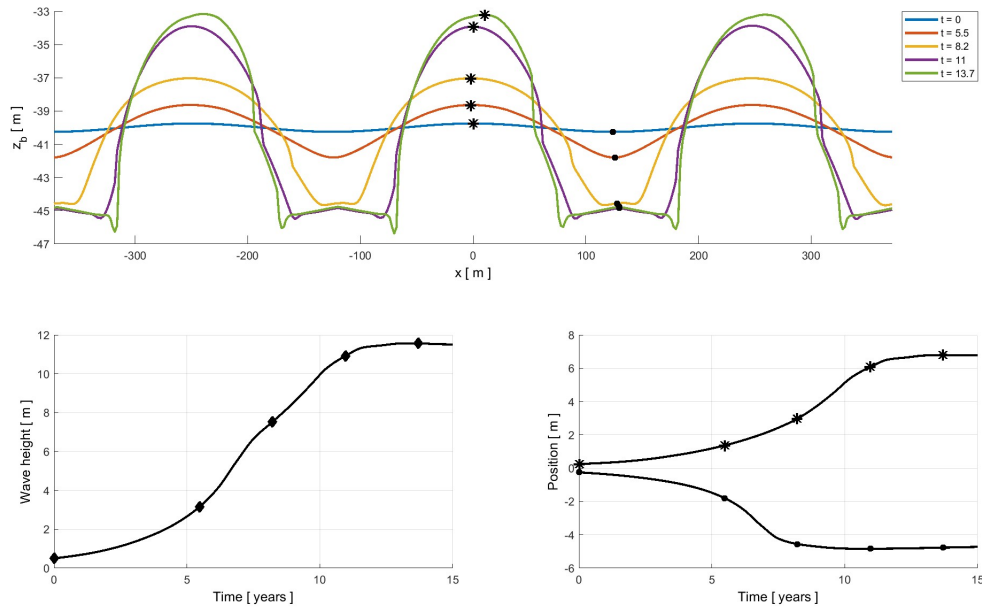
(a) $MF = 125$, $\lambda_{FGM} = 249\text{ m}$



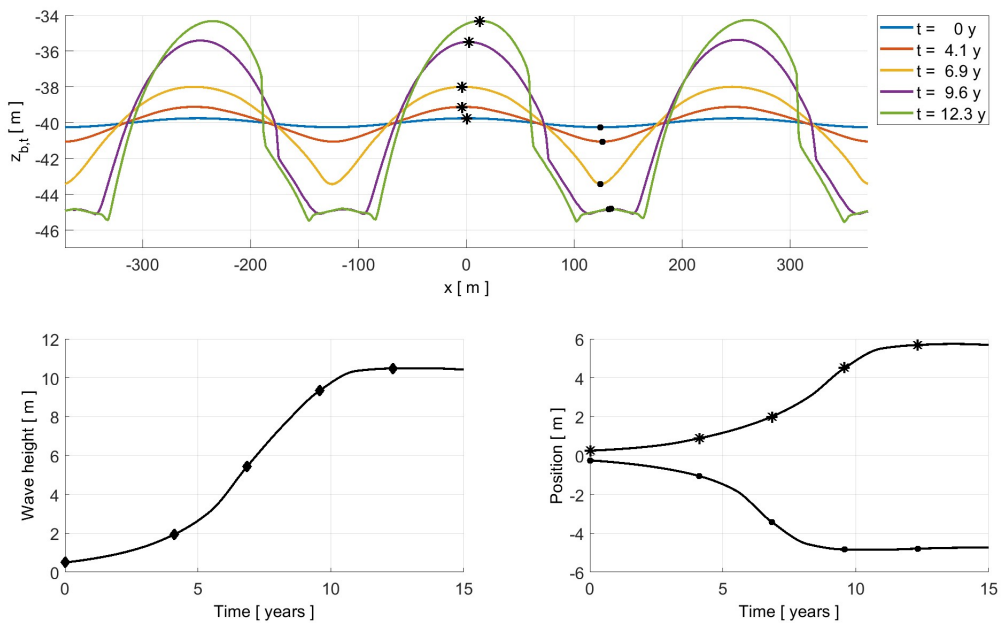
(b) $MF = 250$, $\lambda_{FGM} = 249\text{ m}$



(c) $MF = 500$, $\lambda_{FGM} = 249\text{ m}$



(d) $MF = 1000$, $\lambda_{FGM} = 249\text{ m}$



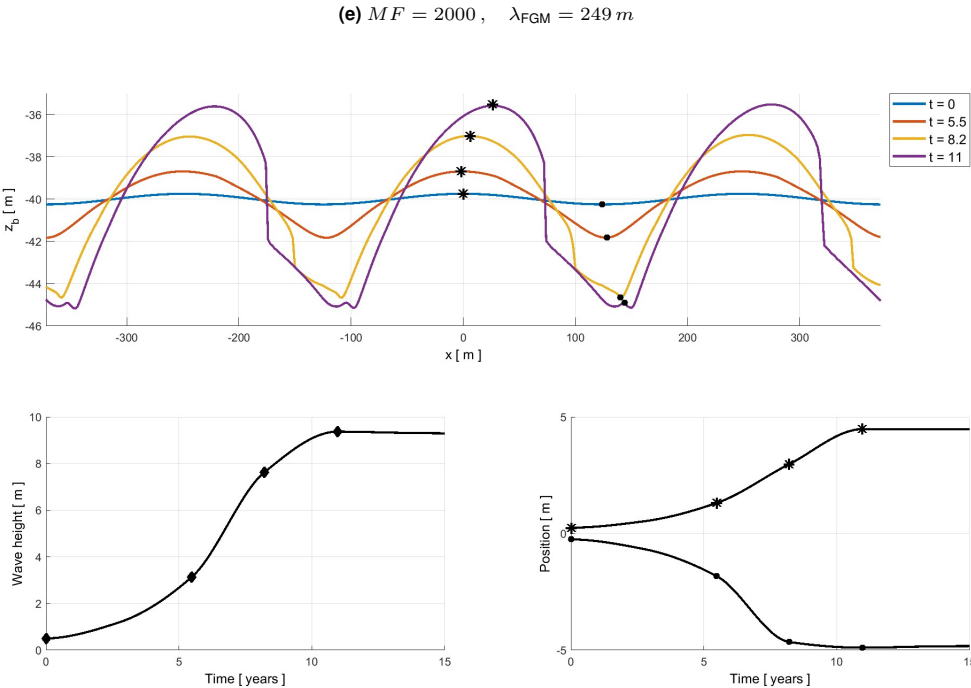
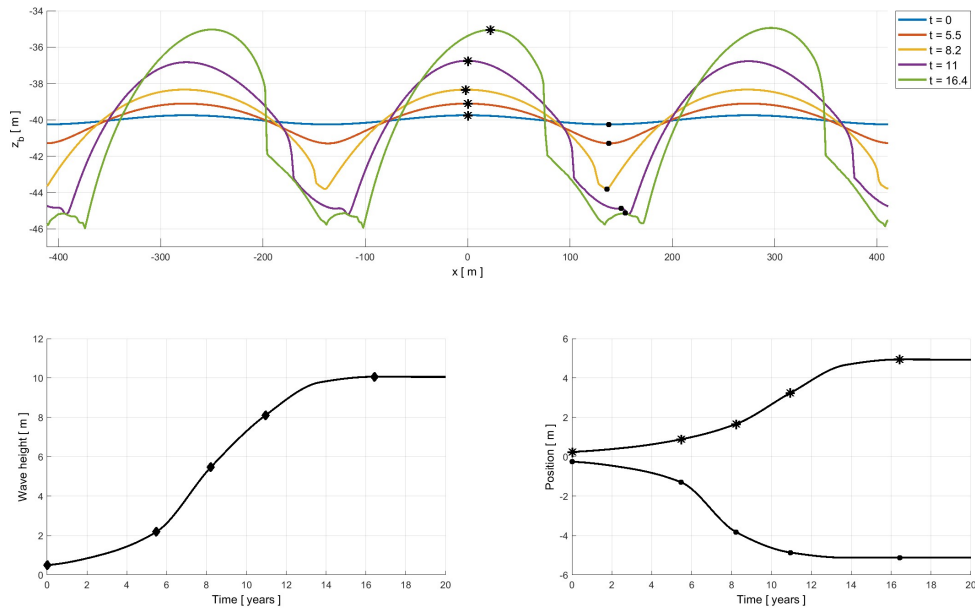


Figure F.1: Long term bed, wave height and crest-trough development for a variable morphological acceleration factor MF

F.2. Suspended load transport

(a) Excluding suspended load transport



(b) Including suspended load transport

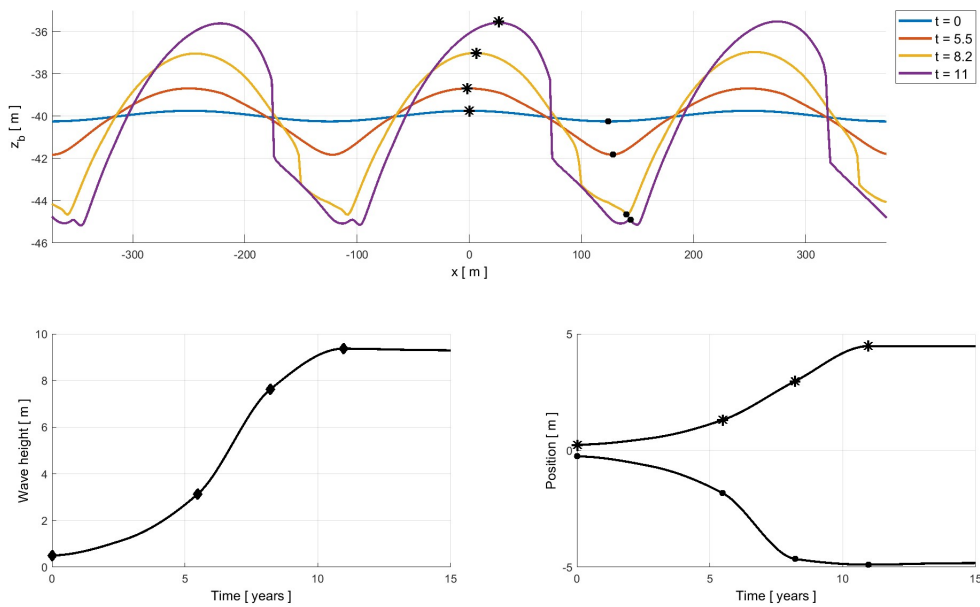
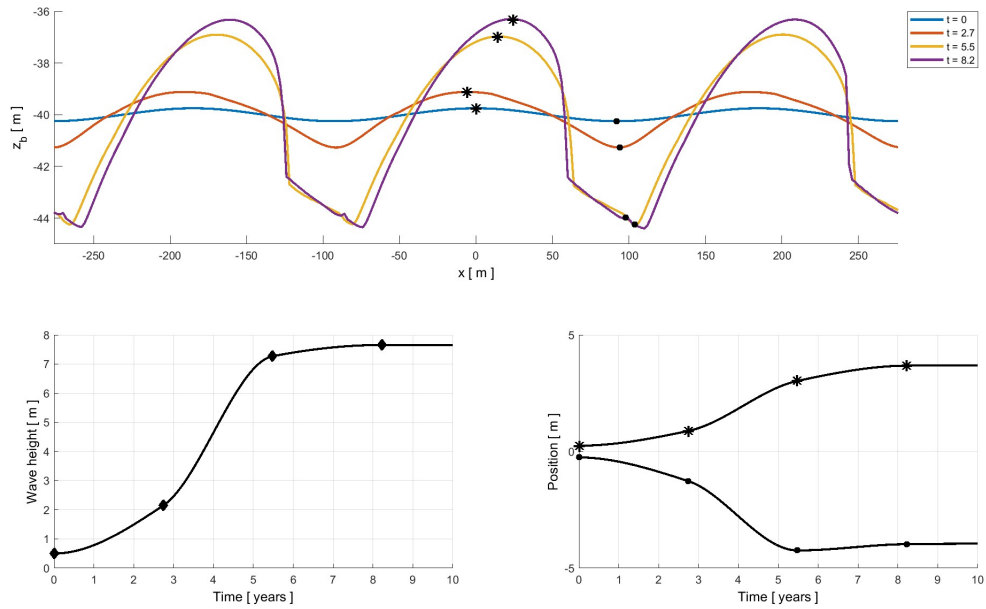


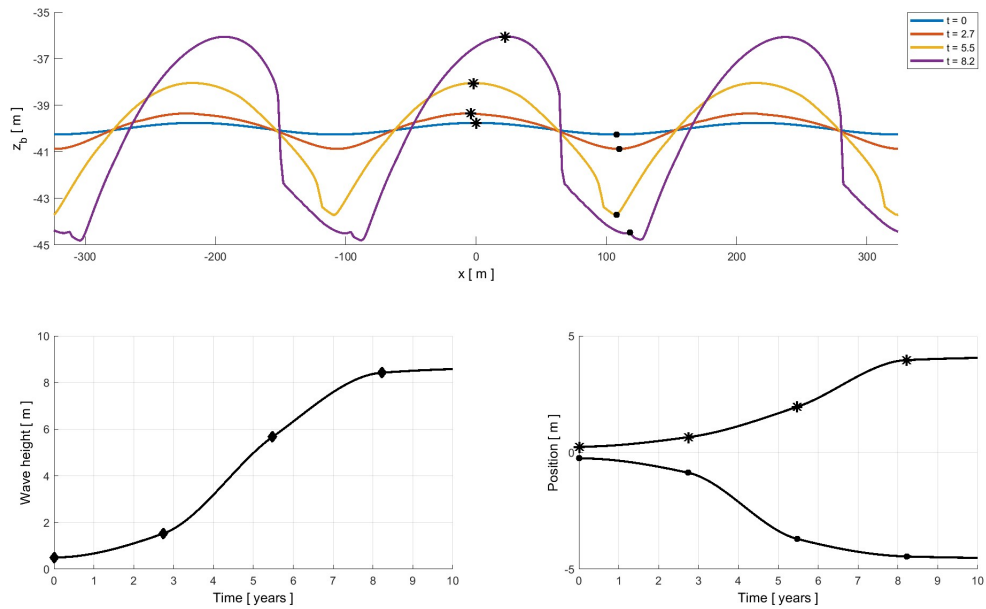
Figure F.2: Long term bed, wave height and crest-trough development ex- and including suspended load transport

F.3. Slope effect tuning parameter

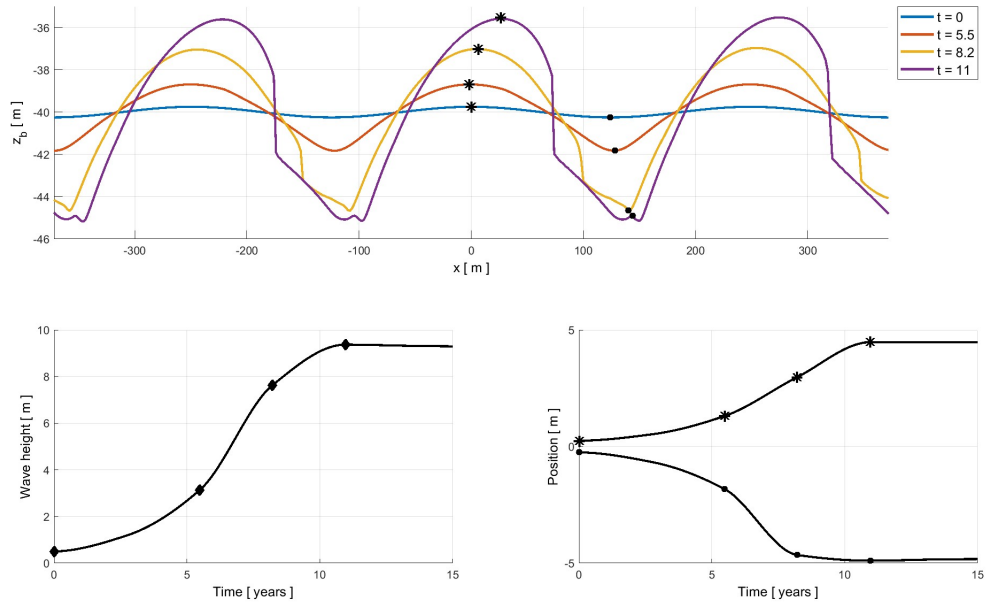
(a) $\alpha_{BS} = 2.50$, $\lambda_{FGM} = 185 \text{ m}$



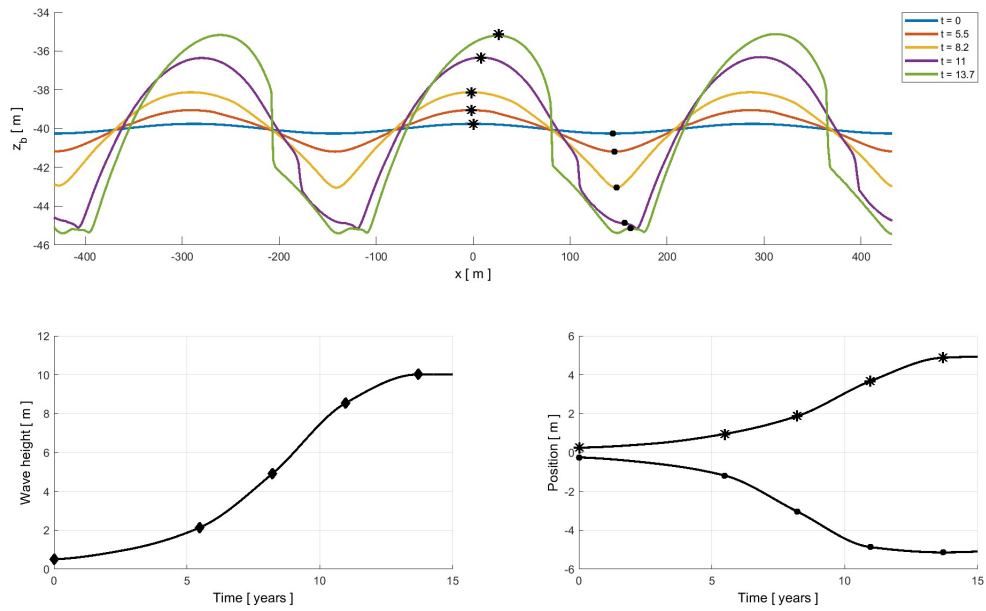
(b) $\alpha_{BS} = 2.75$, $\lambda_{FGM} = 216 \text{ m}$



(c) $\alpha_{BS} = 3.00$, $\lambda_{FGM} = 249 \text{ m}$



(d) $\alpha_{BS} = 3.25$, $\lambda_{FGM} = 288 \text{ m}$



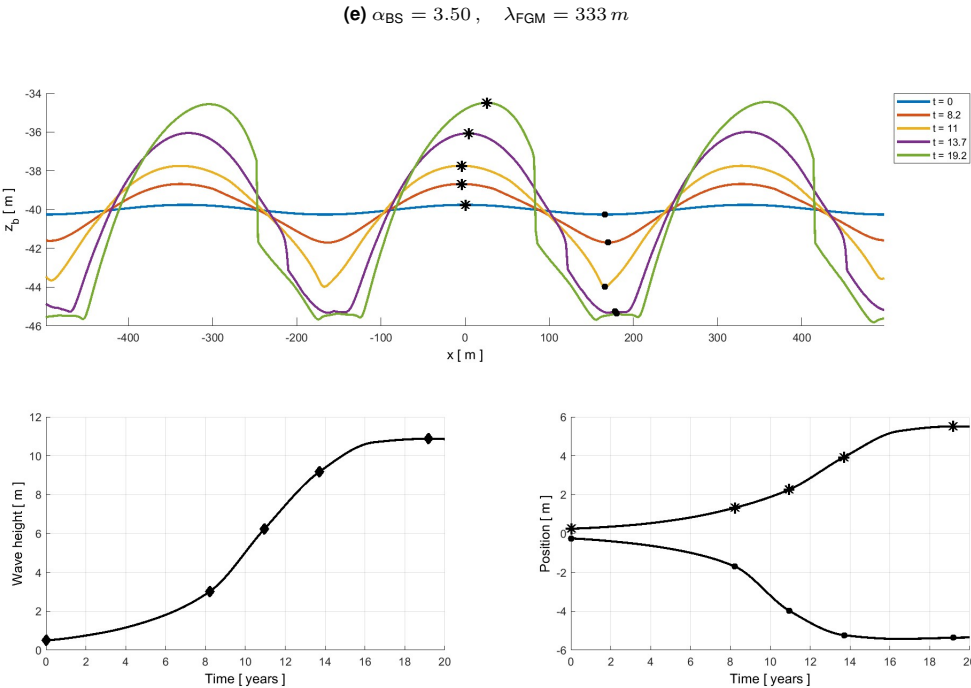
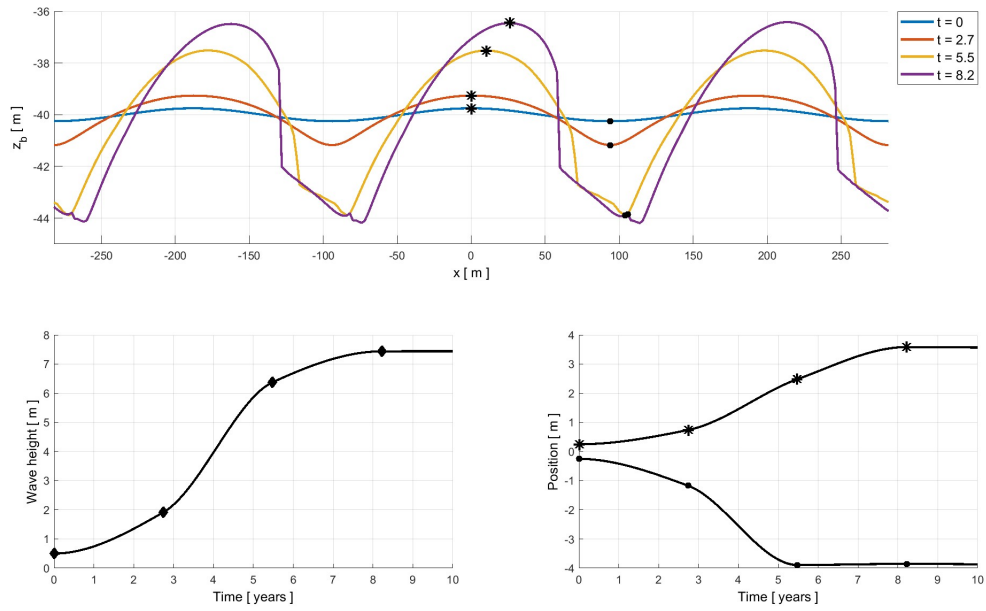


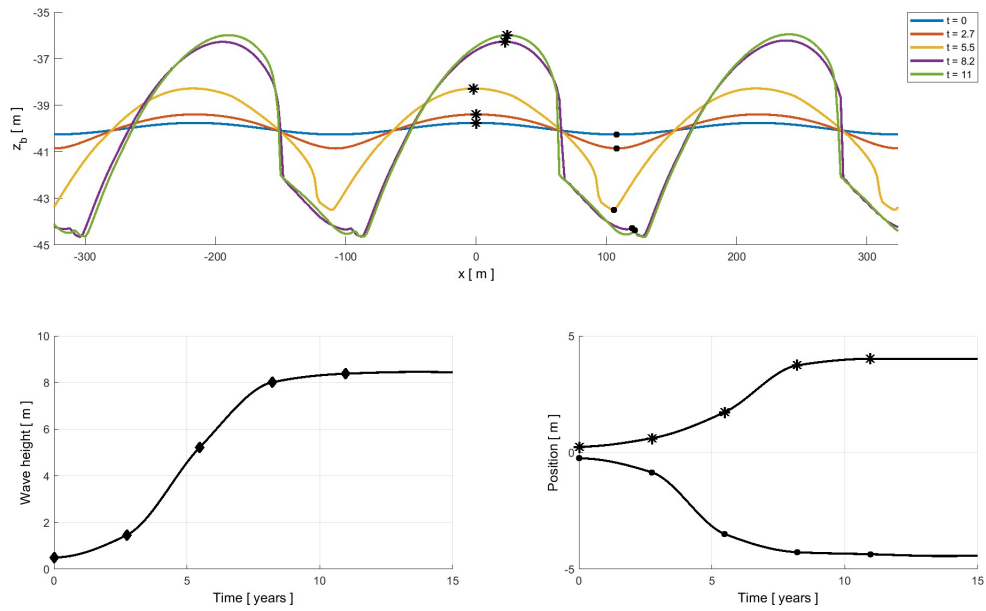
Figure F.3: Long term bed, wave height and crest-trough development for a variable slope effect tuning parameter α_{BS}

F.4. Chezy roughness

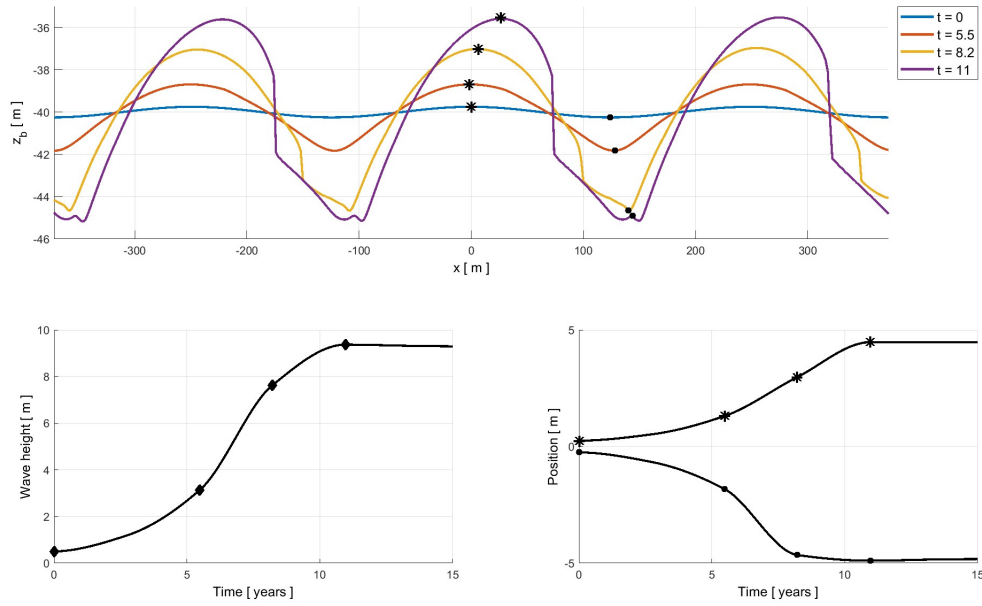
(a) $C = 65.0 \text{ m}^{0.5} \text{ s}^{-1}$, $\lambda_{\text{FGM}} = 188 \text{ m}$



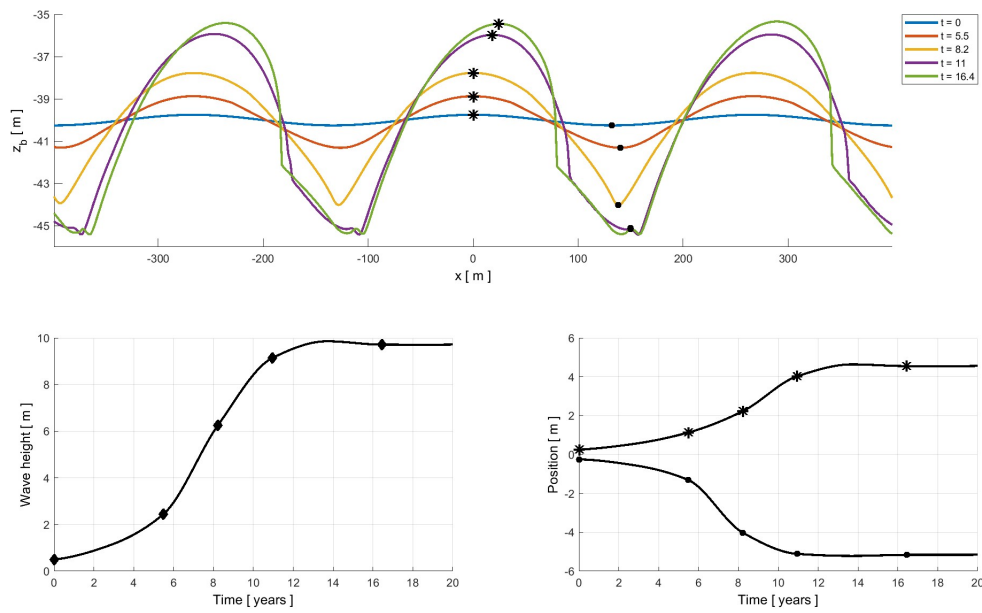
(b) $C = 67.5 \text{ m}^{0.5} \text{ s}^{-1}$, $\lambda_{\text{FGM}} = 216 \text{ m}$



(c) $C = 70.0 m^{0.5} s^{-1}$, $\lambda_{FGM} = 249 m$



(d) $C = 72.5 m^{0.5} s^{-1}$, $\lambda_{FGM} = 266 m$



(e) $C = 75.0 m^{0.5} s^{-1}$, $\lambda_{FGM} = 333 m$

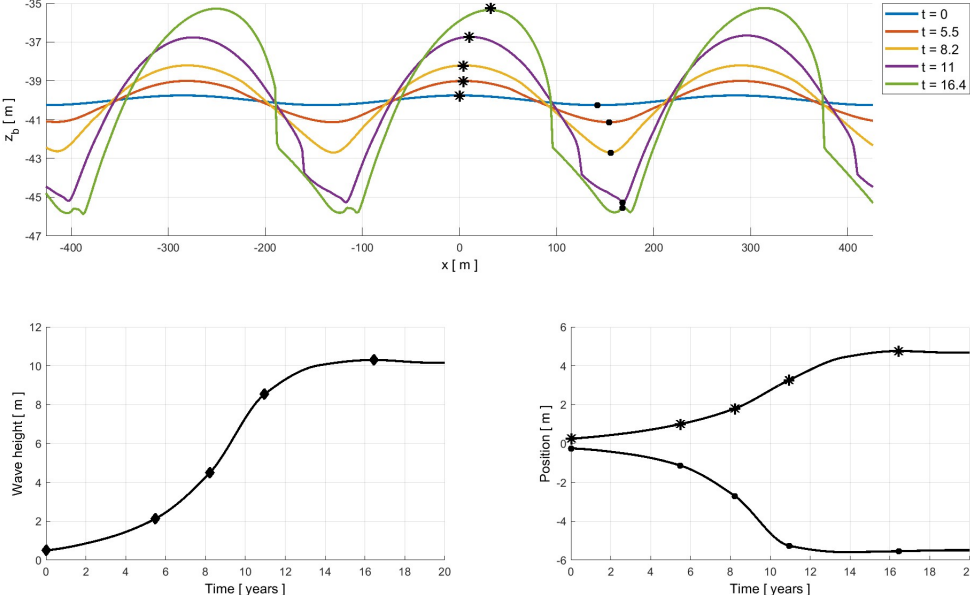
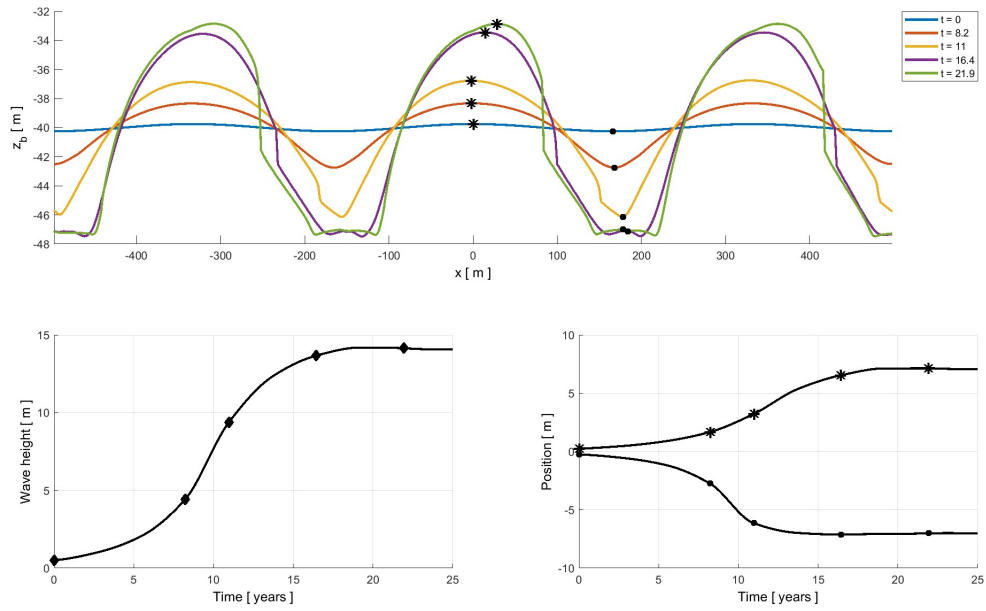


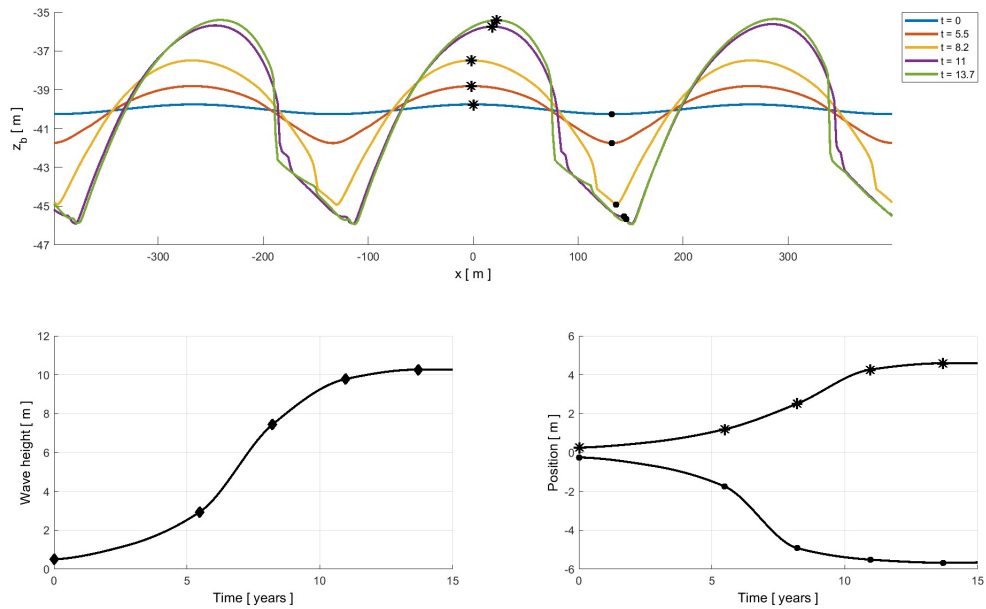
Figure F.4: Long term bed, wave height and crest-trough development for a variable Chezy roughness C

F.5. Grain size

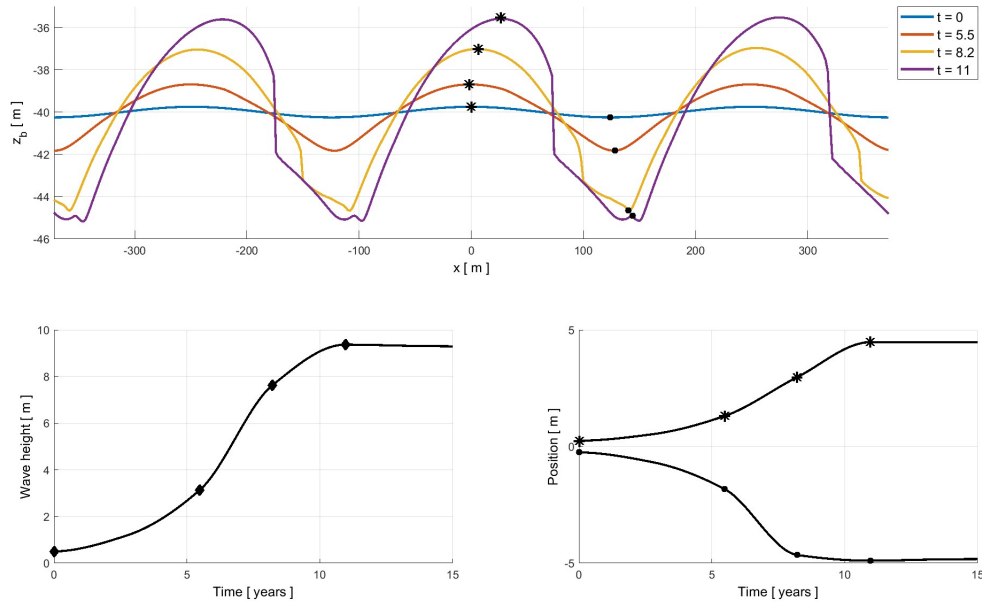
(a) $d = 2.50 \text{ mm}$, $\lambda_{\text{FGM}} = 333 \text{ m}$



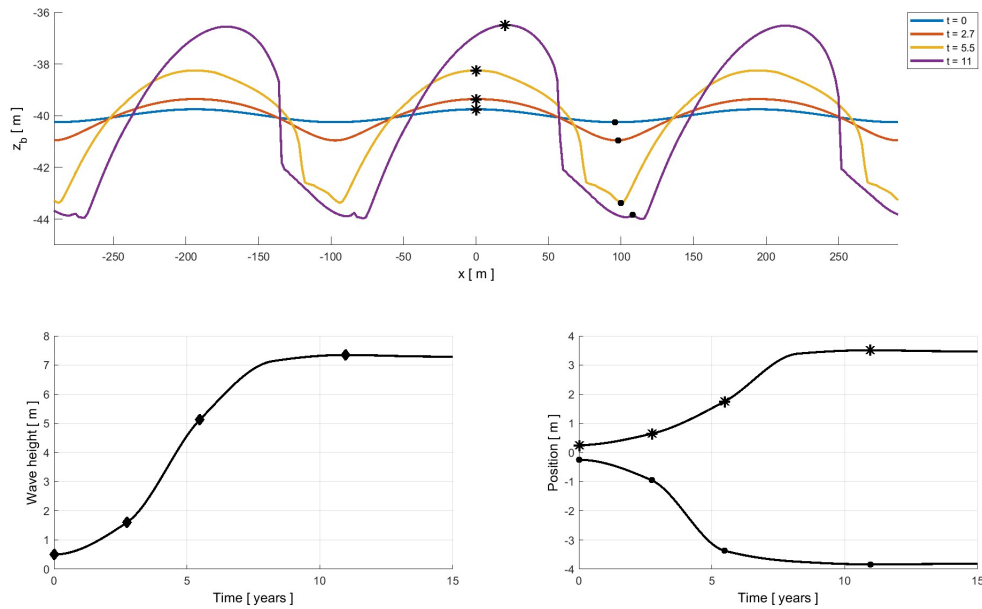
(b) $d = 2.75 \text{ mm}$, $\lambda_{\text{FGM}} = 266 \text{ m}$



(c) $d = 3.00 \text{ mm}$, $\lambda_{\text{FGM}} = 249 \text{ m}$



(d) $d = 3.25 \text{ mm}$, $\lambda_{\text{FGM}} = 194 \text{ m}$



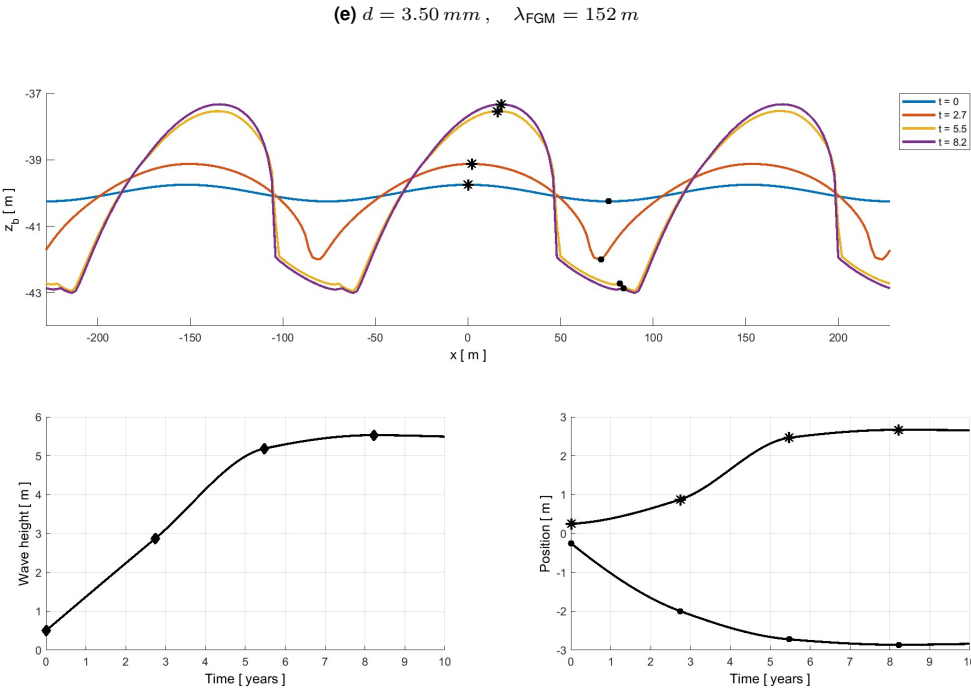
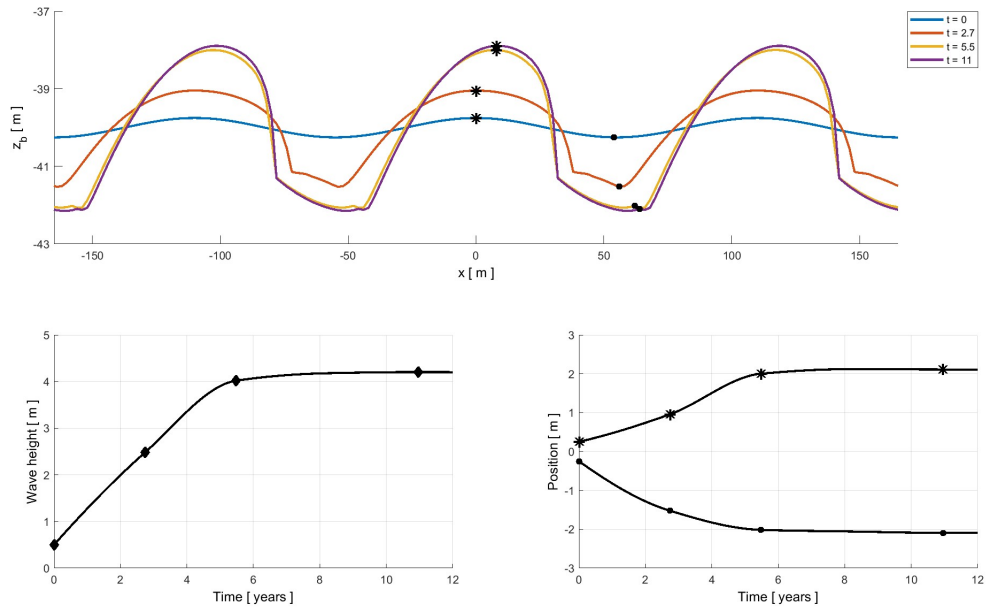


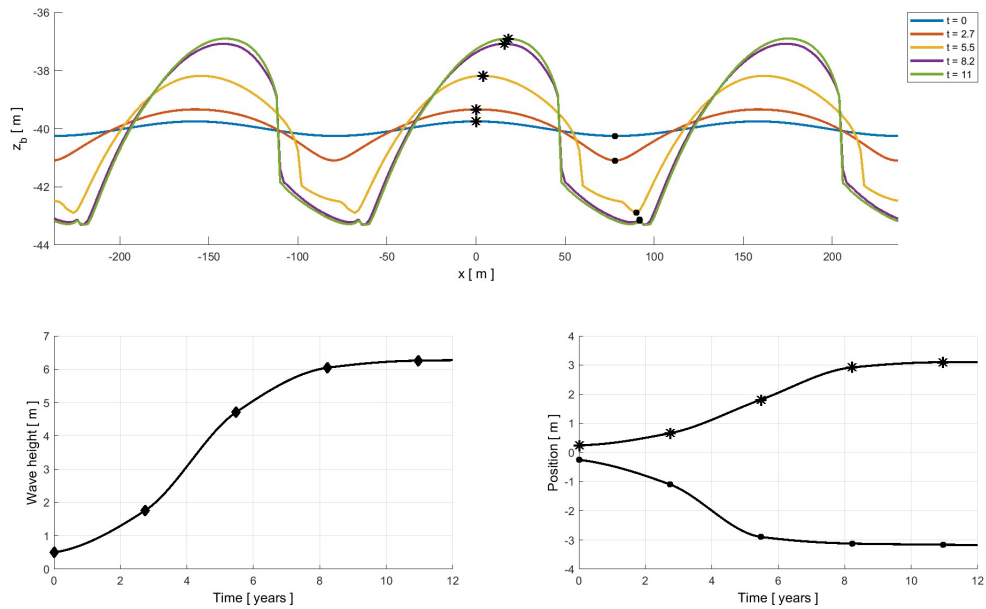
Figure F.5: Long term bed, wave height and crest-trough development for a variable median diameter d

F.6. Tidal velocity amplitude

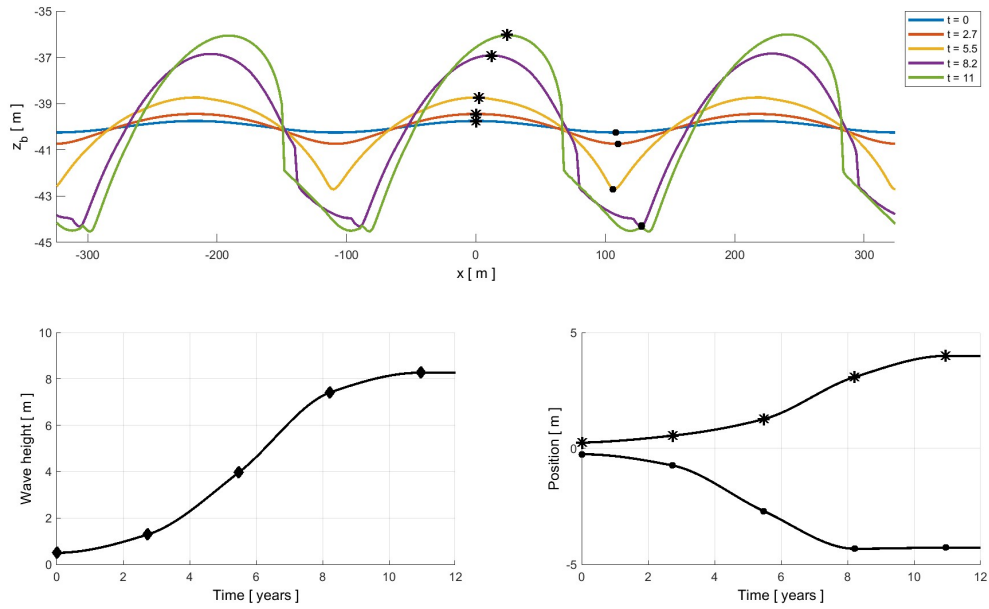
(a) $U_{S2} = 1.60 \text{ m.s}^{-1}$, $\lambda_{FGM} = 110 \text{ m}$



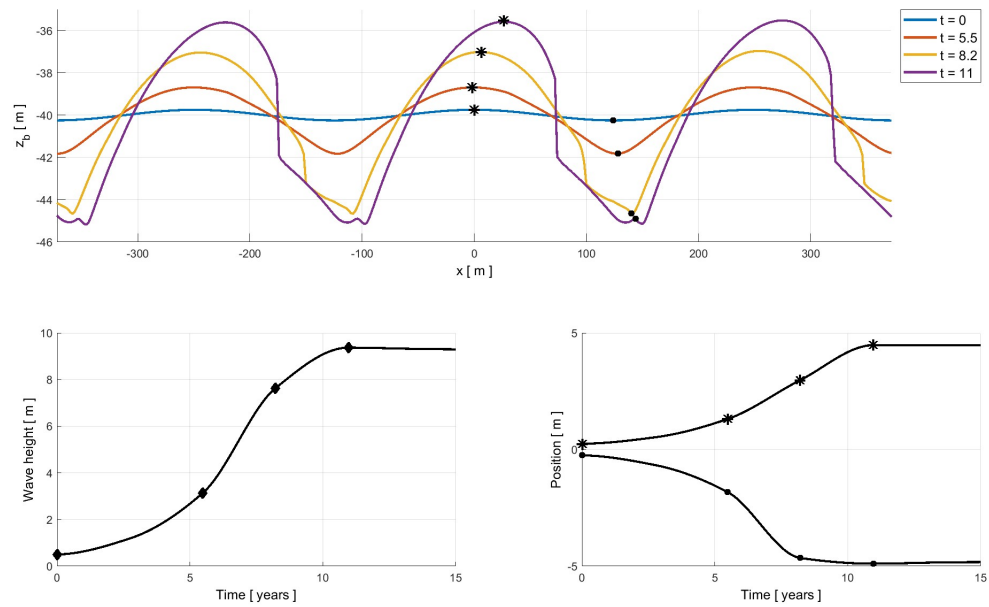
(b) $U_{S2} = 1.70 \text{ m.s}^{-1}$, $\lambda_{FGM} = 158 \text{ m}$



(c) $U_{S2} = 1.80 \text{ m s}^{-1}$, $\lambda_{FGM} = 217 \text{ m}$



(d) $U_{S2} = 1.85 \text{ m s}^{-1}$, $\lambda_{FGM} = 249 \text{ m}$



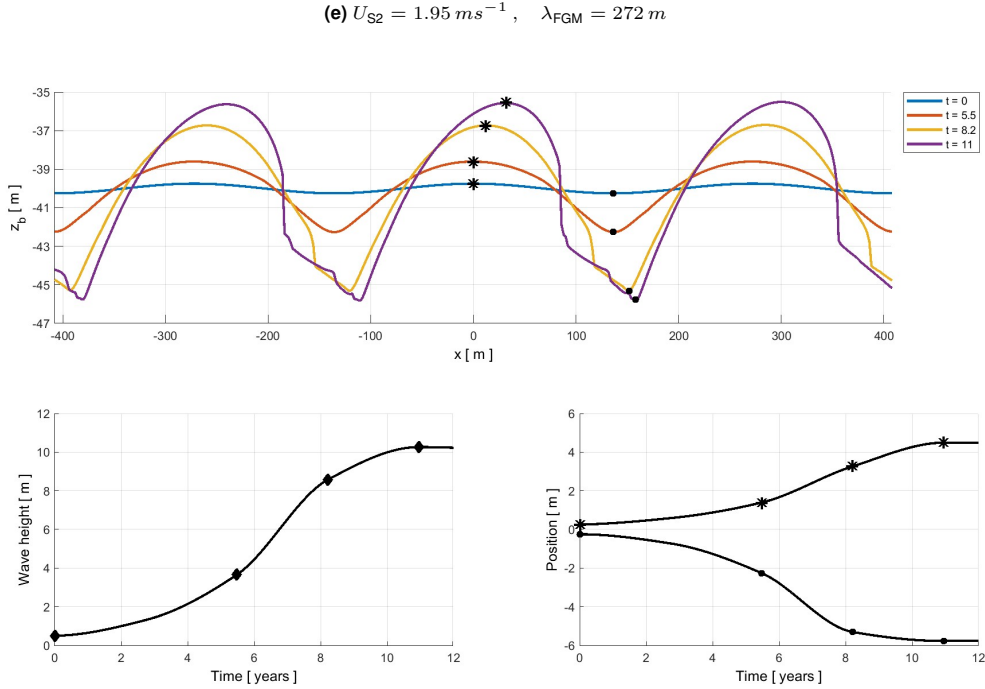
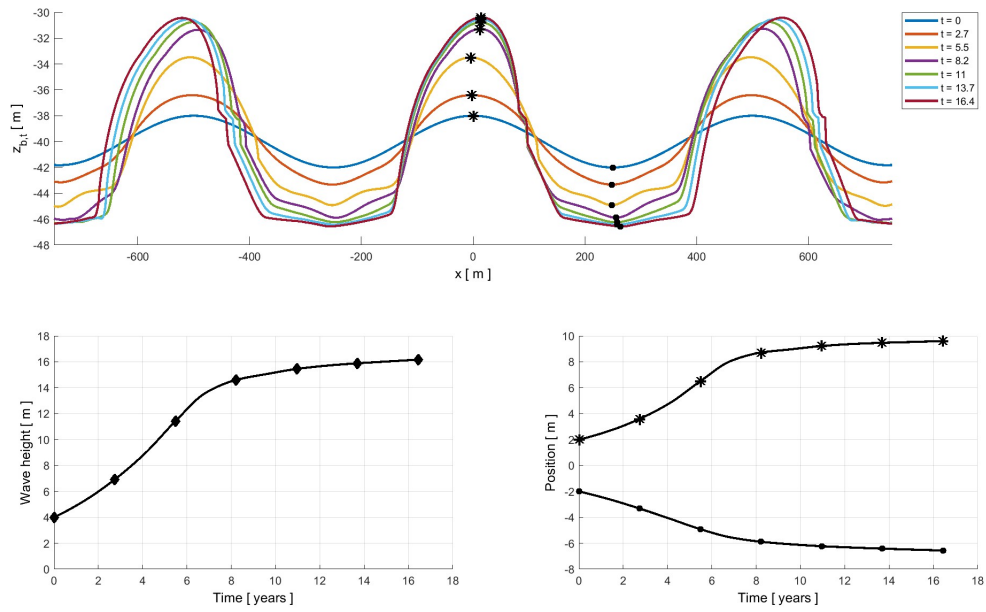


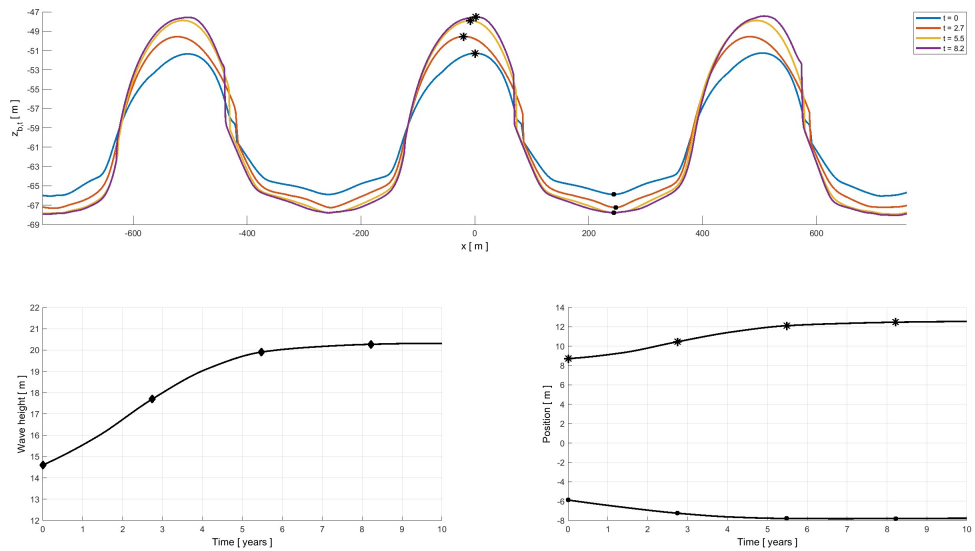
Figure F.6: Long term bed, wave height and crest-trough development for a variable tidal velocity amplitude U_{S2}

F.7. Longer initial wavelength

(a) $H_0 = 40\text{ m}$



(b) $H_0 = 60\text{ m}$



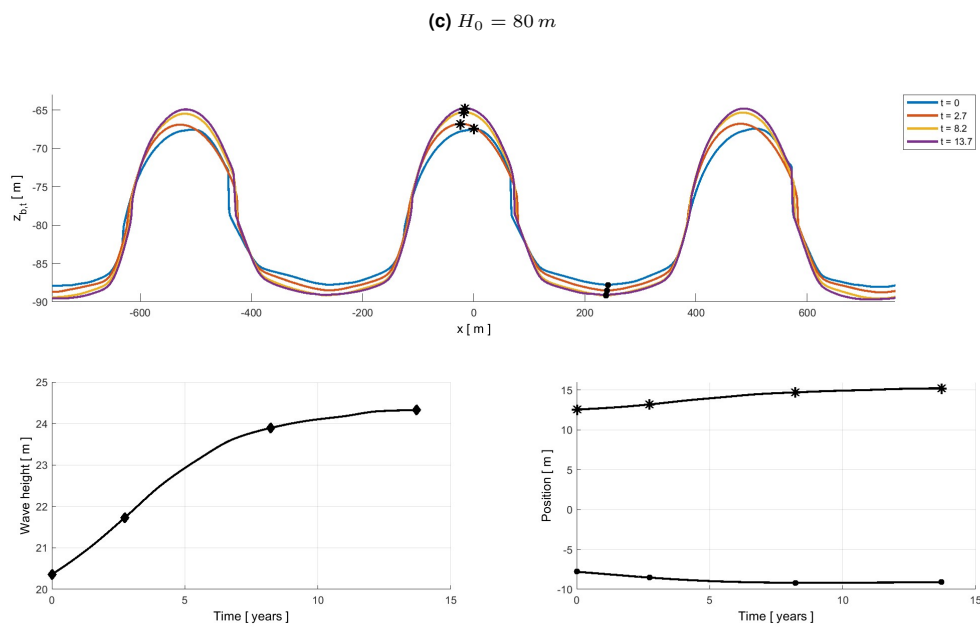


Figure F.7: Long term bed, wave height and crest-trough development for an initial wavelength of $\lambda_0 = 500\text{ m}$ and a variable water depth H_0 . Note that the equilibrium bed level of $H_0 = 40\text{ m}$ and $H_0 = 60\text{ m}$ is used as initial topography for $H_0 = 60\text{ m}$ and $H_0 = 80\text{ m}$, respectively. The used parameters correspond to Case I, see Table 6.1. The number of grid points in the finer part equals 1,250.

G

Bed stratification

G.1. Morphological acceleration factor

A sensitivity analysis is performed to determine the effect of changes in MORFAC value. This analysis is relatively limited due to time limitations. From Chapter 5 it is concluded that the sediment wave characteristics are sensitive to the MORFAC value. Therefore, the MORFAC value is initially reviewed to identify an appropriate value for the remainder of this study. At the beginning, the values of the remaining model and process parameters are adopted from Case II similar to its equilibrium topography.

This relatively short-term analysis involves examining the development of the bed level and the sand fraction in the active transport layer over time. To analyse this initial morphodynamic response of the supplementary sand veneer the model is run for one tidal cycle T . The MORFAC value again accelerates the morphodynamics and the morphological duration. Figure G.4 shows the model results of each MORFAC value individually.

The equilibrium bed level from Case II (Figure 6.4) is adopted as initial topography. Here, a MORFAC value of $MF = 1,000$ is used to reduce computation time. However, this MORFAC value results in significant shape shifting and inaccuracies of the bed level during the simulation as can be seen in Figure G.4b. Similarly, the sediment waves actively move along with the current for $MF = 500$ and to a lesser extent for $MF = 250$. This can be explained by the fact that the tidal velocity amplitude of $U_{S2} = 2.0 \text{ ms}^{-1}$ is fine-tuned to the grain size of fine gravel which is an order of magnitude larger than the selected sand diameter, that is, $d_g = 3.0 \text{ mm}$ and $d_s = 0.30 \text{ mm}$, respectively. In the initial stage after the spin-up time there is a considerable amount of sediment transport which is multiplied by the MORFAC value. In turn, this affects bed level changes significantly. It should also be noted that the flow velocity profile resembles roughly a cosine function, i.e. strongest current directed rightward occurs at $t = 0$ (cf. Figure 7.2). This can also clearly be seen from Figure G.1 in which the sand fraction in the active transport layer is plotted.

In contrast, a MORFAC value of $MF = 1$ entails little change in sand fraction, i.e. sand is only removed from the steep (right side) slope at which flow velocities are strongest. The corresponding

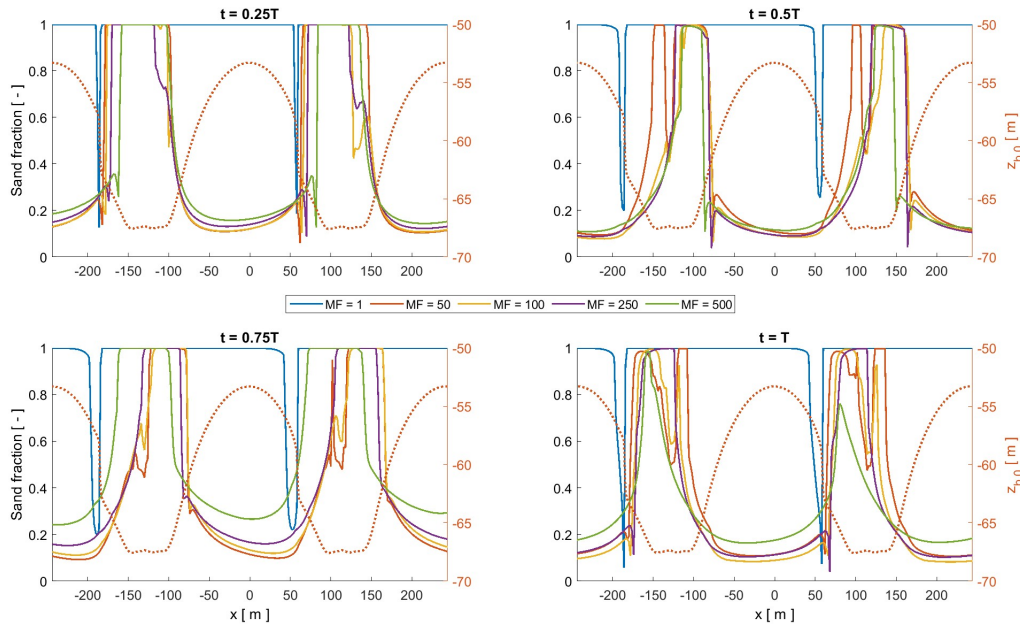
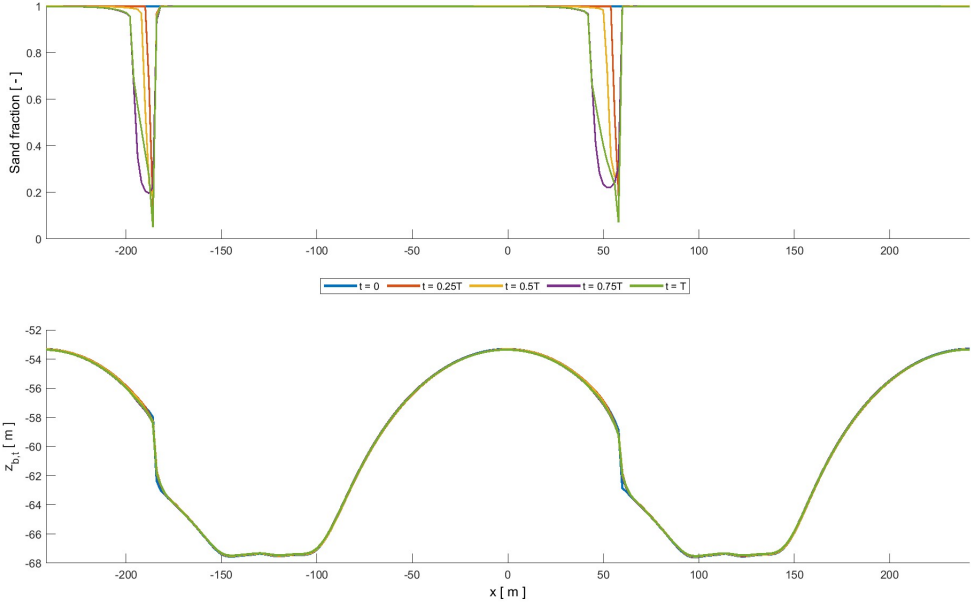


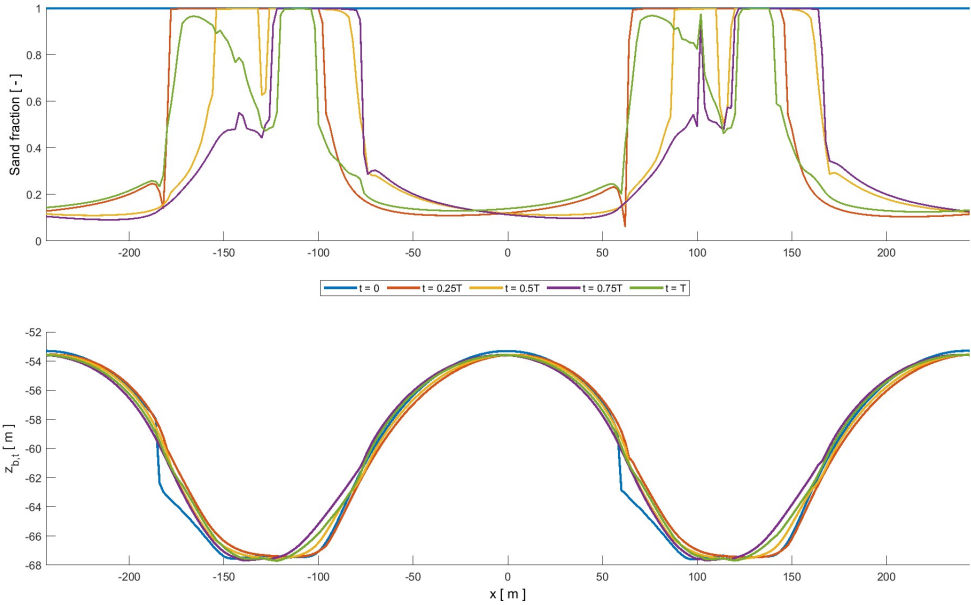
Figure G.1: Sand fraction in the active transport layer (top) and bed level development (bottom) along the x -axis over time t for various MORFAC values. The total time period equals $t = MF \cdot T$ where $T = 12 \text{ h}$. Note that the sand fraction equals $F_s = 1$ at $t = 0$ and that both (cumulative) grain size fractions are the inverse of one another, i.e. $F_g = F_s^{-1}$. At $t = 0$ and $0.5T$ the tidal current velocities are strongest directed to the right and left, respectively. The initial topography $z_{b,0}$ is plotted on the right axis to provide spatial perspective. The used parameter values can be found in Table 7.1.

morphological duration of one tidal cycle is therefore considered insufficient. Furthermore, both simulations for $MF = 50$ and 100 barely differ from one another. It is chosen to proceed with the latter value due to its longer associated morphological duration. Despite the fact that a larger MORFAC value is used rather than $MF = 1$, this morphological duration is still considered an initial response given the larger equilibrium time-scale of the coarse core, see Chapter 6.

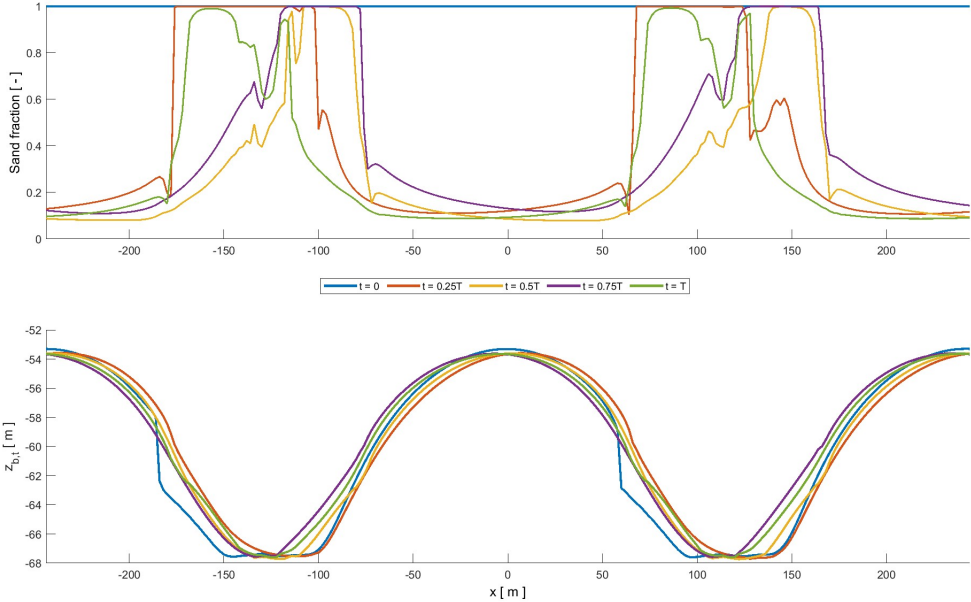
(a) $MF = 1$



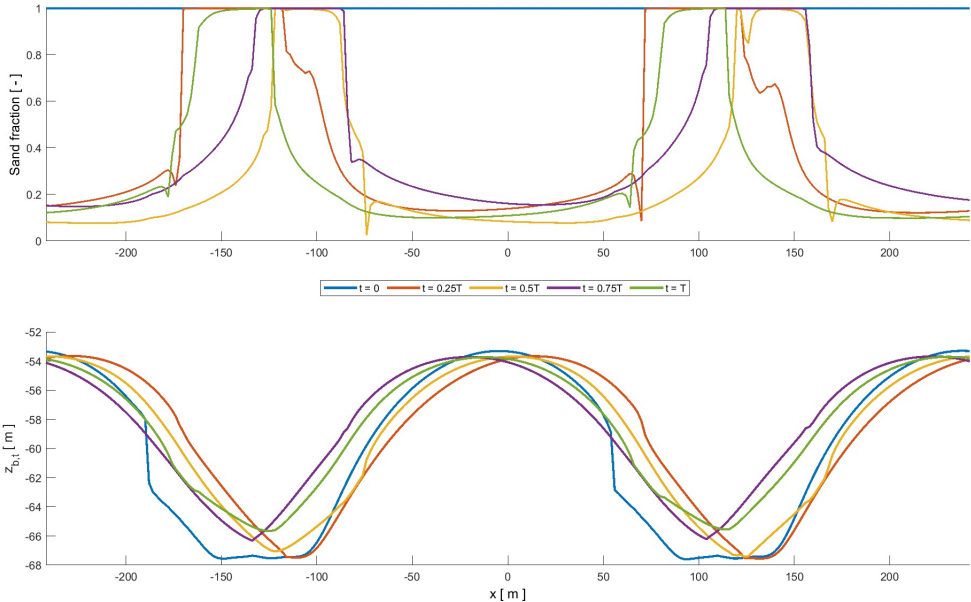
(b) $MF = 50$



(a) $MF = 100$



(b) $MF = 250$



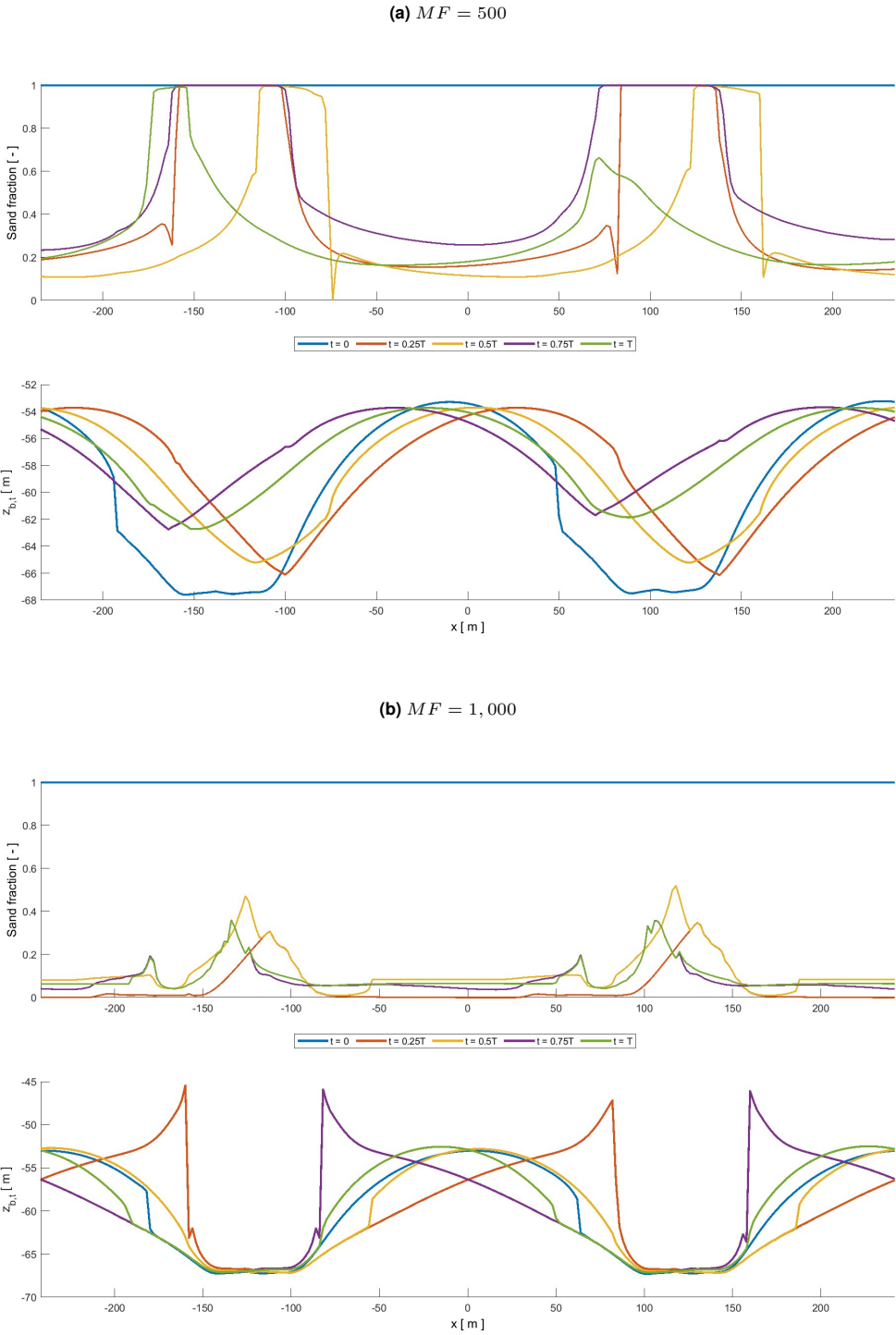


Figure G.4: Sand fraction in the active transport layer (top) and bed level development (bottom) along the x-axis over time t for various MORFAC values MF . Note that the time period equals $t = MF \cdot T$ where $T = 12 h$